



Publicly Accessible Penn Dissertations

1-1-2014

Strain Effects on Thermal Conductivity of Nanostructured Silicon by Raman Piezothermography

Kathryn Fay Murphy

University of Pennsylvania, kmurphy11@gmail.com

Follow this and additional works at: <http://repository.upenn.edu/edissertations>

 Part of the [Mechanical Engineering Commons](#), and the [Mechanics of Materials Commons](#)

Recommended Citation

Murphy, Kathryn Fay, "Strain Effects on Thermal Conductivity of Nanostructured Silicon by Raman Piezothermography" (2014). *Publicly Accessible Penn Dissertations*. 1381.
<http://repository.upenn.edu/edissertations/1381>

This paper is posted at ScholarlyCommons. <http://repository.upenn.edu/edissertations/1381>
For more information, please contact libraryrepository@pobox.upenn.edu.

Strain Effects on Thermal Conductivity of Nanostructured Silicon by Raman Piezothermography

Abstract

A fundamental problem facing the rational design of materials is the independent control of electrical and thermal properties, with implications for a wide range of applications including thermoelectrics, solar thermal power generation, and thermal logic. One strategy for controlling transport involves manipulating the length scales which affect it. For instance, Si thermal conductivity may be reduced with relatively little change in electrical properties when the confining dimension (e.g., nanowire diameter) is small enough that heat carriers are preferentially scattered at free surfaces. However, tailoring properties by geometry or chemistry alone does not allow for on-demand modification, precluding applications which require responsive behavior such as thermal transistors, thermoelectric modules which adapt to their environmental temperature, or switchable thermal barriers.

One means of tuning transport is elastic strain, which has long been exploited to improve carrier mobility in electronic devices. Uniform strain is predicted to affect thermal conductivity primarily via changes in heat capacity and phonon velocity, and crystalline defects such as vacancies or dislocations—which induce large strain gradients—should lower thermal conductivity by decreasing the phonon mean free path. Nanowires are ideal for the study of strain and defect effects due to the availability of a range of elastic strain an order of magnitude larger than in bulk and due to their small volumes. However, experimental measurements of strain-mediated thermal conductivity in nanowires have been limited due to the complexity of simultaneously applying and measuring stress or strain, heating, and measuring temperature.

In this dissertation, we measure strain effects on thermal conductivity using a novel non-contact approach which we name Raman piezothermography. We apply a uniaxial load to individual Si nanowires, Si thin films, and Si micromeshes under a confocal μ -Raman microscope and, using the Raman laser as a heat source and the Raman spectrum as a measure of temperature, determine thermal transport properties. We show that uniaxial strain up to $\sim 1\%$ has a weak effect on Si nanowire or thin film thermal conductivity, but irradiation-induced defects in nanowires yield dramatic reductions due to increased phonon scattering. Such defects are accompanied by large strain gradients, but decoupling the effect of these gradients from local changes in mass and interatomic potential is experimentally untenable. To isolate the effect of strain gradients, we extend our method to Si micromeshes, which exhibit nonuniform strains upon loading. The complex strain states achieved cause more drastic reductions of thermal conductivity due to enhanced phonon-phonon scattering in the presence of a strain gradient. The directions suggested by our experiments, as well as the development of the method, will allow for more robust understanding and control of thermal transport in nanostructures.

Degree Type

Dissertation

Degree Name

Doctor of Philosophy (PhD)

Graduate Group

Materials Science & Engineering

First Advisor

Daniel S. Gianola

Keywords

nanomechanics, Raman spectroscopy, silicon nanowires, strain engineering, tensile testing, thermal conductivity

Subject Categories

Mechanical Engineering | Mechanics of Materials

STRAIN EFFECTS ON THERMAL CONDUCTIVITY OF NANOSTRUCTURED
SILICON BY RAMAN PIEZOTHERMOGRAPHY

Kathryn Fay Murphy

A DISSERTATION

in

Materials Science and Engineering

Presented to the Faculties of the University of Pennsylvania

in

Partial Fulfillment of the Requirements for the

Degree of Doctor of Philosophy

2014

Supervisor of Dissertation

Daniel S. Gianola, Skirkanich Assistant Professor of Innovation

Graduate Group Chairperson

Shu Yang, Professor of Engineering

Dissertation Committee

Ritesh Agarwal, Professor of Engineering

Jennifer R. Lukes, Associate Professor of Engineering

Christopher B. Murray, Richard Perry University Professor of Chemistry and
Materials Science and Engineering

For my parents

ACKNOWLEDGEMENTS

I can take very little credit for this dissertation; without the support of countless colleagues, friends, and family, both personally and professionally, none of this would have been possible. First and foremost I would like to thank my advisor, Prof. Dan Gianola, for his seemingly endless supplies of patience, optimism, energy, and expertise, and for being crazy enough to let an untested PhD student pursue a high-risk project. I hope that these years have convinced him that that was a good idea, worth repeating. Dan also did perhaps the hardest part of the work: getting funding. My research was initially supported by Dan's start-up fund from Penn and then by the U.S. Department of Energy, Office of Basic Energy Sciences, Division of Materials Science and Engineering under Award #DE-SC0008135. I'd also like to thank my excellent labmates, in particular Lisa Chen, who has run the gauntlet of nanomanipulation and MEMS-based tensile testing of nanowires with me from the very beginning; Dr. Brian Piccione, friend, mentor, and optics expert, who did all FDTD simulations and fabrication of free-standing, fully dense Si tensile bars; Dr. Mo-rigen He, who did most of my TEM; Jason Woo, who did FIB milling of Si tensile bars; and Dagny Fleischman, who performed top-down fabrication of Si nanowires.

I'm grateful for having had excellent collaborators and co-conspirators outside of our group, especially Prof. Jennifer Lukes and Mehdi Zanjani, who performed lattice dynamics simulations and were happy to answer all our questions; Prof. Ritesh Agarwal, Pavan Nukala, and Rahul Agarwal, who grew $\text{Ge}_2\text{Sb}_2\text{Te}_5$ and GeTe nanowires and were always up for talking science no matter the hour; Prof. Shu Yang and Elaine Lee, who provided PDMS and the stretching device; Drs. John Sullivan, Tom Harris, and Jinkyong Yoo at the Center for Integrated Nanotechnologies, who provided the tensile testing devices and some Si nanowires; and Prof. Ralph Spolenak and Dr. Martin Süess at ETH, who generously hosted me for a few days while I monopolized their Raman system and also sent strained Si nanobridge samples. I'm further indebted to the shared-use facilities at Penn: the Nanocharacterization Facility, the Nano-Bio Interface Center, and the Quattrone Nanofabrication Facility, and particularly to their excellent staff, Dr. Doug Yates, Dr. Jamie Ford, Dr. Matt Brukman, Kyle Keenan, Dr. Hiromichi Yamamoto, Eric Johnston, Noah Clay, and Dr. Iulian Codreanu. I'm sorry about all the times I had a hand in something breaking. Finally, thanks to the indispensable people who keep the LRSM running: Steve Szewczyk, Pat Overend, Vicky Lee, Irene Clements, Rico Vargas, Fred Hellmig, and Raymond Hsiao.

We are extraordinarily lucky, at Penn, to work in such a collaborative, friendly, and open environment, where it goes without saying that we all succeed when one of us does. To all the people who I have ever turned to for help, or bounced an idea off

of, or lent me equipment, or held an event with free coffee: thank you. I've mentioned some of these brilliant, hard working, good looking people already, and additional thanks go to Penn Profs. Russ Composto, Karen Winey, Ertugrul Cubukcu, Chris Murray, and Andrew Rappe, as well as Rob Ferrier, Mike O'Reilly, Carlos Aspetti, Ryan McCaffrey, Ethan Alguire, Jason Reed, Ashley Gaulding, Dr. Rose Mutiso, Prof. Tevis Jacobs, Vicky Doan-Nguyen, Dan Magagnosc, Daksh Agarwal, Dr. David Kim, Prof. Mike Hore, Danny Strickland, Cathy Yang, and Emmabeth Parrish.

I have been fortunate to have generous, supportive, and loving parents, Ava and Art Murphy, who were truly the key ingredients of my PhD. In making me who I am, they worked on this longer than I did.

Finally, my immeasurable thanks to my husband-to-be, Jason Pope, whose unwavering love and support made the highs higher and the lows not as low, and who still wants to marry me despite my struggles to get home from lab in time for dinner.

A doctorate is a strange thing: I have never felt as ignorant, nor as capable, as I do now.

ABSTRACT

STRAIN EFFECTS ON THERMAL CONDUCTIVITY OF NANOSTRUCTURED SILICON BY RAMAN PIEZOTHERMOGRAPHY

Kathryn Fay Murphy
Daniel S. Gianola

A fundamental problem facing the rational design of materials is the independent control of electrical and thermal properties, with implications for a wide range of applications including thermoelectrics, solar thermal power generation, and thermal logic. One strategy for controlling transport involves manipulating the length scales which affect it. For instance, Si thermal conductivity may be reduced with relatively little change in electrical properties when the confining dimension (e.g., nanowire diameter) is small enough that heat carriers are preferentially scattered at free surfaces. However, tailoring properties by geometry or chemistry alone does not allow for on-demand modification, precluding applications which require responsive behavior such as thermal transistors, thermoelectric modules which adapt to their environmental temperature, or switchable thermal barriers.

One means of tuning transport is elastic strain, which has long been exploited to improve carrier mobility in electronic devices. Uniform strain is predicted to affect thermal conductivity primarily via changes in heat capacity and phonon velocity, and crystalline defects such as vacancies or dislocations—which induce large strain gradients—should lower thermal conductivity by decreasing the phonon mean free path.

Nanowires are ideal for the study of strain and defect effects due to the availability of a range of elastic strain an order of magnitude larger than in bulk and due to their small volumes. However, experimental measurements of strain-mediated thermal conductivity in nanowires have been limited due to the complexity of simultaneously applying and measuring stress or strain, heating, and measuring temperature.

In this dissertation, we measure strain effects on thermal conductivity using a novel non-contact approach which we name Raman piezothermography. We apply a uniaxial load to individual Si nanowires, Si thin films, and Si micromeshes under a confocal μ -Raman microscope and, using the Raman laser as a heat source and the Raman spectrum as a measure of temperature, determine thermal transport properties. We show that uniaxial strain up to $\sim 1\%$ has a weak effect on Si nanowire or thin film thermal conductivity, but irradiation-induced defects in nanowires yield dramatic reductions due to increased phonon scattering. Such defects are accompanied by large strain gradients, but decoupling the effect of these gradients from local changes in mass and interatomic potential is experimentally untenable. To isolate the effect of strain gradients, we extend our method to Si micromeshes, which exhibit nonuniform strains upon loading. The complex strain states achieved cause more drastic reductions of thermal conductivity due to enhanced phonon-phonon scattering in the presence of a strain gradient. The directions suggested by our experiments, as well as the development of the method, will allow for more robust understanding and control of thermal transport in nanostructures.

TABLE OF CONTENTS

ACKNOWLEDGEMENTS	iii
ABSTRACT	v
LIST OF TABLES	ix
LIST OF FIGURES	xi
1 Introduction	1
1.1 Elastic Strain	4
1.2 Thermal Conductivity	6
1.2.1 Surface Effects on Thermal Conductivity	8
1.2.2 Uniform Strain Effects on Thermal Conductivity	11
1.2.3 Nonuniform Strain Effects on Thermal Conductivity	20
1.3 Raman Spectroscopy of Crystalline Solids	22
1.3.1 Strain Effects on the Si Raman Spectrum	24
1.3.2 Temperature Effects on the Si Raman Spectrum	27
1.4 Summary and Thesis Outline	28
2 Tensile Testing of Nanowires	29
2.1 Materials and Methods	29
2.2 Effect of Clamp Deformation on Effective Strain Measurement	37
2.3 Mechanical Properties of Semiconductor Nanowires	47
2.3.1 Si Nanowires	47
2.3.2 GST Nanowires	48
2.3.3 GeTe Nanowires	51
2.4 Conclusions	54
3 Raman-Based Method for Measuring Thermal Conductivity in Strained Nanowires	56
3.1 Mathematical Model	57
3.2 Materials and Methods	62
3.2.1 Si Nanowires	62
3.2.2 Raman Mapping of Nanowires	63
3.2.3 Decoupling Strain and Temperature	69
3.2.4 Correction for Actuator Heating	72
3.2.5 Calculation of Nanowire Cross-Section and Absorption Efficiency	74
3.2.6 Heat Losses Due to Air Conduction	76
3.3 Conclusions	80

4	Raman Piezothermography of Strained Si Nanostructures	81
4.1	Si Nanowires	81
4.1.1	Unstrained Si Nanowires	81
4.1.2	Uniformly Strained Si Nanowires	83
4.1.3	Dependence of Raman Shift on Stress	86
4.1.4	Estimates of Measurement Uncertainty	86
4.1.5	Defected Si Nanowires	89
4.2	Si Micromeshes	95
4.2.1	Tensile Bar and Micromesh Fabrication	96
4.2.2	Uniformly Strained Si Films	98
4.2.3	Strained Si Micromeshes	102
4.3	Conclusions	106
5	Conclusions and Prospectives	109
5.1	Si Nanomeshes	110
5.2	Other Materials for Tunable Thermal Conductivity	113
5.3	Further Applications of Raman Piezothermography	114
5.3.1	Graphene	115
5.3.2	Piezoresistive Systems	116
5.4	Size Dependence of the Heat Transfer Coefficient	116
5.5	Strain Effects on Seebeck Coefficient	118
5.6	Mechanical Behavior of GeTe Nanowires	119
	Appendix A Raman Thermography on the NT-MDT NTEGRA System at Penn	120
	BIBLIOGRAPHY	128

LIST OF TABLES

TABLE 1:	Non-zero components of the strain tensor for a diamond-structure crystal with a uniaxial load where the principal axes are $[100]$, $[010]$, $[001]$	25
TABLE 2:	Geometry of nanowires and EBID clamps used for clamp stiffness determination, in addition to measured values of wire stiffnesses and Young's moduli.	46

LIST OF FIGURES

FIGURE 1.1: Diameter dependence of fracture strength in VLS-grown Si nanowires	2
FIGURE 1.2: One-dimensional uniform strain	6
FIGURE 1.3: Diameter and roughness dependence of Si nanowire thermal conductivity	11
FIGURE 1.4: Phonon dispersion of Si under strain	13
FIGURE 1.5: MD predictions of strain effects on Si thermal conductivity	20
FIGURE 1.6: Predicted Raman spectra for Si under stress.	26
FIGURE 2.1: Semiconductor nanowires used for mechanical testing	31
FIGURE 2.2: Tensile testing method	35
FIGURE 2.3: Stress strain curves of inorganic nanowires	39
FIGURE 2.4: Clamp stiffness effects on measurement of Young’s modulus	41
FIGURE 2.5: EBID clamp geometries	42
FIGURE 2.6: Mechanical testing of $\text{Ge}_2\text{Sb}_2\text{Te}_5$ nanowires	49
FIGURE 2.7: Mechanical testing of GeTe nanowires	53
FIGURE 3.1: Schematic of setup for determination of the heating profile as a function of laser position	59
FIGURE 3.2: Thermal circuit model	60
FIGURE 3.3: Experimental setup for Raman piezothermography	64
FIGURE 3.4: Scheme for determining power absorbed when the laser is not centered on the nanowire	65
FIGURE 3.5: Raman shifts in Si nanowires	67
FIGURE 3.6: Temperature rise from laser heating of diffused EBID material	68
FIGURE 3.7: MD simulations to find χ_T dependence on stress	71
FIGURE 3.8: Correction for actuator heating	73
FIGURE 3.9: Cross-section-dependent power absorption of nanowires . . .	75
FIGURE 3.10: Nanowire heat transfer to air	79
FIGURE 4.1: Thermal conductivity of unstrained Si nanowires	83
FIGURE 4.2: Thermal conductivity of a Si nanowire as a function of uniaxial stress	85
FIGURE 4.3: Si nanowire Raman shift dependence on stress	87
FIGURE 4.4: Residuals of heating profile fits	88
FIGURE 4.5: Thermal conductivity of irradiated Si nanowires	91
FIGURE 4.6: Strained Si micromeshes for reduced thermal conductivity .	97
FIGURE 4.7: Thermal conductivity measurements of strained Si films . .	99
FIGURE 4.8: Si tensile bar Raman shift dependence on stress	101
FIGURE 4.9: Thermal conductivity measurements of strained Si micromeshes	104

FIGURE 5.1: Thermal conductivity of strained Si	110
FIGURE 5.2: Pattern rotation for exploring anisotropy in Si nanomeshes .	112
FIGURE A.1: Schematic of steps in the grips	128

Chapter 1

Introduction

That the strength of materials tends to increase as the sample size becomes smaller has been known since the 1950s, when Brenner showed that the fracture strength of single-crystal microwires depended strongly on diameter and length.¹ This volume dependence arises from the spatial distribution of the atomic-scale defects responsible for plastic flow or fracture, which may be reduced in number or eliminated altogether by reducing sample size. A size effect on the mechanical properties of Si was first reported by Namazu *et al.*, who showed increases in bending strength from 0.5 to 17.5 GPa when the diameter of cantilevers was reduced from mm length scales to hundreds of nm.² Many other groups have studied the size dependence of mechanical behavior in Si using bending,³⁻⁸ resonance,⁹ or tensile testing,¹⁰⁻¹⁵ and the definitive work in the field was performed by Zhu *et al.*,¹⁰ who showed a pronounced diameter dependence in tensile tests of vapor-liquid-solid (VLS) grown Si nanowires with diameters in the 15 to 60 nm range. Nanowires with diameters below 30 nm exhibited a decrease in Young's modulus from the bulk value, and fracture strengths of the thinnest nanowires exceeded 12 GPa, an order of magnitude higher than typical bulk Si and about half the ideal tensile strength of 22 GPa.^{16, 17} A summary of the experimentally measured fracture strengths of single-crystal, VLS-grown nanowires may be seen in Figure 1.1. Although the absolute values differ widely between reports,

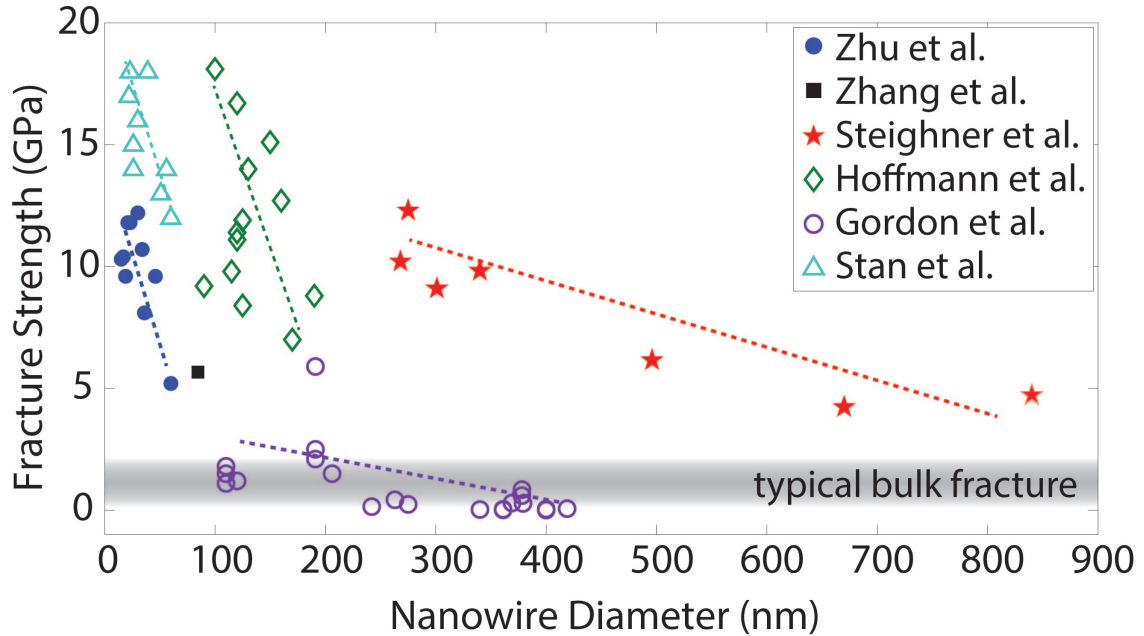


Figure 1.1: Diameter dependence of fracture strength in VLS-grown Si nanowires. Closed symbols indicate tensile testing; open symbols indicate bending. Data are taken from Refs. 4–6, 10–12. Lines are intended as guides for the eye. Although the exact values differ, in the vast majority of reports Si nanowires exhibit much larger fracture strength than bulk, with a strong trend toward higher strength with smaller diameter. This implies a larger range over which to tune strain-sensitive properties in Si nanostructures.

likely due to differences in sample quality and testing method, the trend is clear: as the diameter of a Si nanowire is reduced, it can accommodate more stress—and hence more strain—before fracture.

The expanded range of elastic strain available in nano-Si implies that there is also an expanded range in the properties which couple to strain. Strain has long been used as a means of tuning electrical properties by warping and splitting of the electronic band structure, e.g. in strained Si field effect transistors.^{18–20} One example of a potential

application of strained Si which has not been fully explored is in thermoelectrics, which convert thermal gradients to electrical potential. Thermoelectric efficiency is gauged by the non-dimensional figure of merit ZT :

$$ZT = \frac{S^2 \sigma T}{\kappa} \quad (1.1)$$

where $S = -(\Delta V/\Delta T)|_{I=0}$ is the Seebeck coefficient, σ is the electrical conductivity, and κ is thermal conductivity, and T is temperature. A good thermoelectric has high S , high σ , and low κ in order to yield high voltages from the temperature gradient, efficiently conduct current, and maintain the temperature gradient, respectively. Si in bulk is a poor thermoelectric, but nanostructured Si can have thermoelectric efficiencies orders of magnitude higher due to a drastic lowering of thermal conductivity. Progress in this field has moved quickly: the effect was first demonstrated in Si nanowires in 2008^{21, 22}, nanocrystalline bulk Si in 2009,²³ and nanomesh or “holey” Si thin film structures in 2010,²⁴ with dozens of reports in the following years.

The efficiency of nano-Si is not quite competitive with conventional thermoelectric materials (e.g. PbTe, Bi₂Te₃), but as Si is cheaper, more abundant, and less toxic than those materials, it is an attractive alternative. We may furthermore be able to improve the efficiency of nano-Si by modifying the band structure via strain. However, the effect of strain on thermal conductivity of these structures has been experimentally unexplored, despite the fact that, as we will see, tensile strain is expected to lower

thermal conductivity, potentially improving the thermoelectric figure of merit in nano-Si.

In this dissertation we will examine the thermal conductivity of Si nanowires, thin films, and micromeshes under strain using a novel method which we have named Raman piezothermography. In this chapter we will review concepts in elasticity, thermal conductivity of crystalline insulators with attention paid to size and strain effects, and the application of Raman spectroscopy to crystalline Si. In the following chapters we will describe the novel method used to perform simultaneous mechanical and thermal measurements of nanowires, thin films, and micromeshes and discuss the results of these experiments, as well as new directions for nanoscale strain engineering.

1.1. Elastic Strain

In order to explore strain effects on thermal conductivity, we must first define some basic terms in solid mechanics. Strain is the ratio of deformation to length, and in one dimension engineering strain, e_x , may be written

$$e_x = \frac{\Delta L}{L} = \frac{\partial u}{\partial x} \quad (1.2)$$

where $\Delta L/L$ refers to the overall percent change in length (the average linear strain), and u and x are displacement and position of any point within the body.²⁵ This may be seen schematically in Figure 1.2. The above equality holds for uniform or homogeneous

strain where force and strain are the same throughout the body; $\Delta L/L \neq \frac{\partial u}{\partial x}$ at every point for nonuniform or heterogeneous strain, where strain varies depending on position (i.e., there is a strain gradient). In three dimensions, strain at a point is a symmetric second-rank tensor:

$$\epsilon_{ij} = \begin{vmatrix} \epsilon_{xx} & \epsilon_{xy} & \epsilon_{xz} \\ \epsilon_{xy} & \epsilon_{yy} & \epsilon_{yz} \\ \epsilon_{xz} & \epsilon_{yz} & \epsilon_{zz} \end{vmatrix} = \begin{vmatrix} \frac{\partial u}{\partial x} & \frac{1}{2} \left(\frac{\partial u}{\partial y} + \frac{\partial v}{\partial x} \right) & \frac{1}{2} \left(\frac{\partial u}{\partial z} + \frac{\partial w}{\partial x} \right) \\ \frac{1}{2} \left(\frac{\partial u}{\partial y} + \frac{\partial v}{\partial x} \right) & \frac{\partial v}{\partial y} & \frac{1}{2} \left(\frac{\partial v}{\partial z} + \frac{\partial w}{\partial y} \right) \\ \frac{1}{2} \left(\frac{\partial u}{\partial z} + \frac{\partial w}{\partial x} \right) & \frac{1}{2} \left(\frac{\partial v}{\partial z} + \frac{\partial w}{\partial y} \right) & \frac{\partial w}{\partial z} \end{vmatrix} \quad (1.3)$$

where the u, v, w represent displacement from initial position x, y, z .²⁵ Stress, defined as force per unit area, is also a symmetric second-rank tensor, and for small deformation it is related to elastic strain via Hooke's Law:

$$\epsilon_{ij} = S_{ijkl} \sigma_{ij} \quad (1.4)$$

where σ_{ij} and S_{ijkl} are the stress and compliance tensors, respectively. For one-dimensional deformation, this simplifies to

$$\epsilon = \frac{1}{E} \sigma \quad (1.5)$$

where E is known as Young's modulus.²⁵ We note that these definitions apply to solids under small displacements where the deformation is elastic, meaning that the material returns to its original shape on unloading. Si is considered a "linear elastic" material,

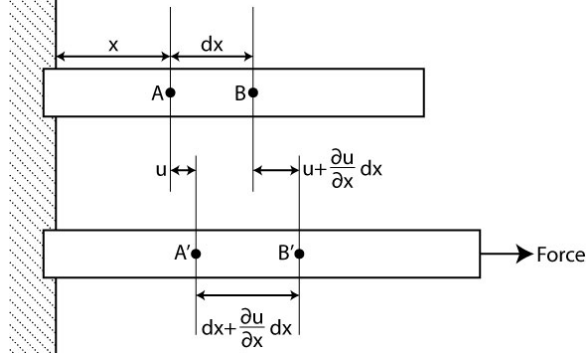


Figure 1.2: Schematic of one-dimensional uniform strain adapted from Ref. 25. For a body deforming in response to a uniaxial force, point A moves to A' and B moves to B'. Since B is further from the fixed end, it is displaced more than A. The initial separation between the points, dx , then becomes $dx + \partial u/\partial x dx$.

meaning that it obeys Equation 1.5 and exhibits a linear relationship between stress and strain up to its fracture stress, with no permanent (“plastic”) deformation.

1.2. Thermal Conductivity

Turning now to basic concepts in thermal transport, thermal conductivity is defined as the proportionality constant between heat current, \vec{j} and the temperature gradient. For a sample with a temperature gradient $\vec{\nabla}T$, Fourier’s law states:

$$\vec{j} = -\overleftrightarrow{\kappa} \cdot \vec{\nabla}T = -(\overleftrightarrow{\kappa}_e + \overleftrightarrow{\kappa}_l) \cdot \vec{\nabla}T \quad (1.6)$$

where the $\overleftrightarrow{\kappa}_e$, $\overleftrightarrow{\kappa}_l$ are the electron and lattice (phonon) contributions to the thermal conductivity, respectively. The electronic component of the thermal conductivity is given by the Wiedemann-Franz law, which states that, for fixed temperature, $\overleftrightarrow{\kappa}_e$ is

linearly related to the electrical conductivity. For moderately doped bulk Si with room temperature resistivity $1 \text{ m}\Omega\cdot\text{cm}$ (corresponding to dopant concentration approximately 10^{20} cm^{-3}), charge carriers are responsible for just 0.5% of the thermal conductivity.²⁶ Here we study systems with negligible $\vec{\kappa}_e$, so only the phononic contribution to thermal conductivity will be considered. For heavily doped or highly piezoresistive systems, thermal measurements would need to be combined with measurements of electrical conductivity in order to discern the separate contributions to $\vec{\kappa}$. One would also need to consider the effect of phonon scattering from a higher population of charge carriers.

By treating phonons in a three-dimensional material as an ideal gas (a reasonable assumption at room temperature since, at equilibrium, they are randomly moving, weakly interacting particles), we can apply the classical kinetic theory of gases to derive an expression for the thermal conductivity. If we consider a particle moving a distance \vec{l} between regions with temperature difference ΔT , we can write

$$\Delta T = \vec{\nabla}T \cdot \vec{l} = \vec{\nabla}T \cdot \vec{v}\tau \quad (1.7)$$

where \vec{v} is the particle's velocity and τ is the time to move distance \vec{l} .²⁶ In moving from $T + \Delta T$ to T , the particle loses energy $c\Delta T$, where c is the particle's heat capacity. We can then write the rate of change of energy for a single particle as²⁷

$$\frac{dE}{dt} = c\vec{\nabla}T \cdot \frac{d\vec{l}}{dt} = c\vec{\nabla}T \cdot \vec{v}. \quad (1.8)$$

For particle concentration n , the net particle flux is $n\vec{v}$, so by combining this with Equations 1.7 and 1.8 the net heat (equivalently, energy) flux for all particles is then given by

$$\vec{j} = -n\vec{v}\frac{dE}{dt} = -nc\tau(\vec{v} \cdot \vec{v})\vec{\nabla}T. \quad (1.9)$$

We may further write the total heat capacity as $C = nc$, and if we consider all phonon modes, where a mode consists of a single frequency and wavevector, we arrive at the expression for the components of $\vec{\kappa}$:

$$\kappa_{ij} = \sum_{\alpha} C_{\alpha}\tau_{\alpha}v_{i}v_{j} \quad (1.10)$$

where the modes are denoted by α and i, j refer to the three principal axes of the chosen coordinate system.²⁸ Therefore, by examining how we may tune a material's heat capacity, scattering times, or phonon velocities, we may derive means of engineering thermal conductivity.

1.2.1. Surface Effects on Thermal Conductivity

Nanostructuring affects thermal conductivity through reductions in phonon scattering time, τ , and phonon confinement effects. The latter are significant in nanowires and thin films with critical dimension nearly an order of magnitude smaller than the samples to be discussed in later chapters, so here we will focus on scattering only. When the critical dimension d (e.g. nanowire diameter, film thickness) falls

within the spectrum of phonon mean free paths for a given material, phonon scattering at free surfaces becomes significant. The effect of various scattering mechanisms on scattering time, which is inversely proportional to mean free path, may be understood according to Matthiessen’s rule:²⁹

$$\tau = \left(\sum_s \tau_s^{-1} \right)^{-1} \quad (1.11)$$

where the sum is over the types of mechanisms: boundary scattering, defect scattering, phonon-phonon scattering, phonon-electron scattering, isotope scattering, etc. Reductions in scattering time will lead to reductions in thermal conductivity; in the case of nano-Si this comes from a reduction in $\tau_{boundary}$. Assuming diffusive transport dominates (a reasonable assumption for nanowires except at cryogenic temperatures, where ballistic transport plays a role³⁰), Matthiessen’s rule yields a reduction from the bulk thermal conductivity of

$$\kappa_{NW} = \frac{d \kappa_{bulk}}{l_{bulk} + d} \quad (1.12)$$

where κ_{NW} and κ_{bulk} are the thermal conductivities of the nanowire and bulk Si, respectively, and l_{bulk} is the bulk mean free path.³¹

The first study of Si nanowire thermal conductivity was performed by Li *et al.* on VLS-grown Si nanowires with diameters ranging from 22 to 115 nm, which were found to have thermal conductivities far lower than bulk—over an order of magnitude

for the thinnest wires at room temperature—with a strong diameter dependence in accordance with Equation 1.12.³² The group repeated the experiment in a later work which examined VLS nanowires with diameters 15 to 20 nm, as well as nanowires which had been oxidized and etched in HF to produce rougher surfaces.³⁰ The roughened nanowires were found to have far lower thermal conductivities than smooth wires of similar size. The difference was explained by increases in diffuse scattering at rough surfaces, as opposed to specular or mirror-like scattering at atomically smooth surfaces, depending on phonon frequency and the height of the roughness. Other works have similarly shown a decrease in thermal conductivity in Si nanowires with controlled surface roughness.^{22, 33–35} Results of the various measurements of nanowire thermal conductivity and surface roughness may be seen in Figure 1.3.

A critical flaw present in all of these studies of roughness effects is that the chemical etching process used to produce and roughen Si nanowires is known to also produce pores and core defects^{36, 37} which could lower thermal conductivity. Such defects may additionally be undetectable using a transmission electron microscope (TEM)—the tool of choice in these studies for determining crystal quality—and could therefore have been overlooked. One of the definitive studies of surface roughness acknowledged this possibility as their Raman spectra of incrementally roughened wires were consistent with Raman spectra of Si containing incrementally higher concentrations of defects.³³ No experimental studies have yet been performed which used alternative roughening methods or in which the effects of roughness and defects

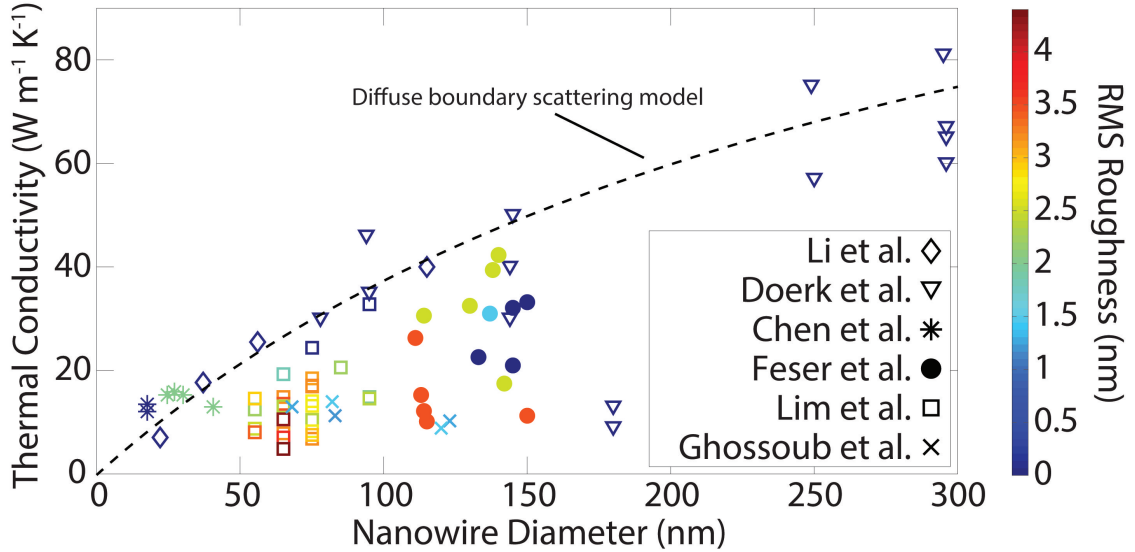


Figure 1.3: Diameter and roughness dependence of Si nanowire thermal conductivity. By comparison, bulk Si has thermal conductivity $150 \text{ W m}^{-1} \text{ K}^{-1}$,³⁹ well off the axes of this figure. Data are taken from Refs. 30–35. The coloring of the data points correlates with the RMS surface roughness as per the colorbar. All nanowires with zero RMS roughness were VLS-grown except those from Feser *et al.* and Ghossoub *et al.*, which were produced using top-down etching methods. Roughened or top-down wires generally have lower thermal conductivities than VLS nanowires of the same size. The exceptions to this trend at $\sim 175 \text{ nm}$ were believed by the authors of that study to be an artifact of their measurement method.

were quantitatively decoupled and determined—although simulations do predict that surface roughness is not sufficient to produce the observed thermal conductivity drops and that core defects are necessary³⁸—motivating the need for such experiments.

1.2.2. Uniform Strain Effects on Thermal Conductivity

Turning to strain’s effect on thermal transport, we see from Equation 1.10 that thermal conductivity depends on heat capacity, scattering time, and phonon velocity.

The strain effects on these quantities may be understood via their dependence on phonon frequency. The force constants of Si, which change with strain, lead to decreasing phonon frequencies with tensile strain⁴⁰⁻⁴³ (see Figure 1.4), and we can use this to gain some intuition about how thermal conductivity changes with strain.

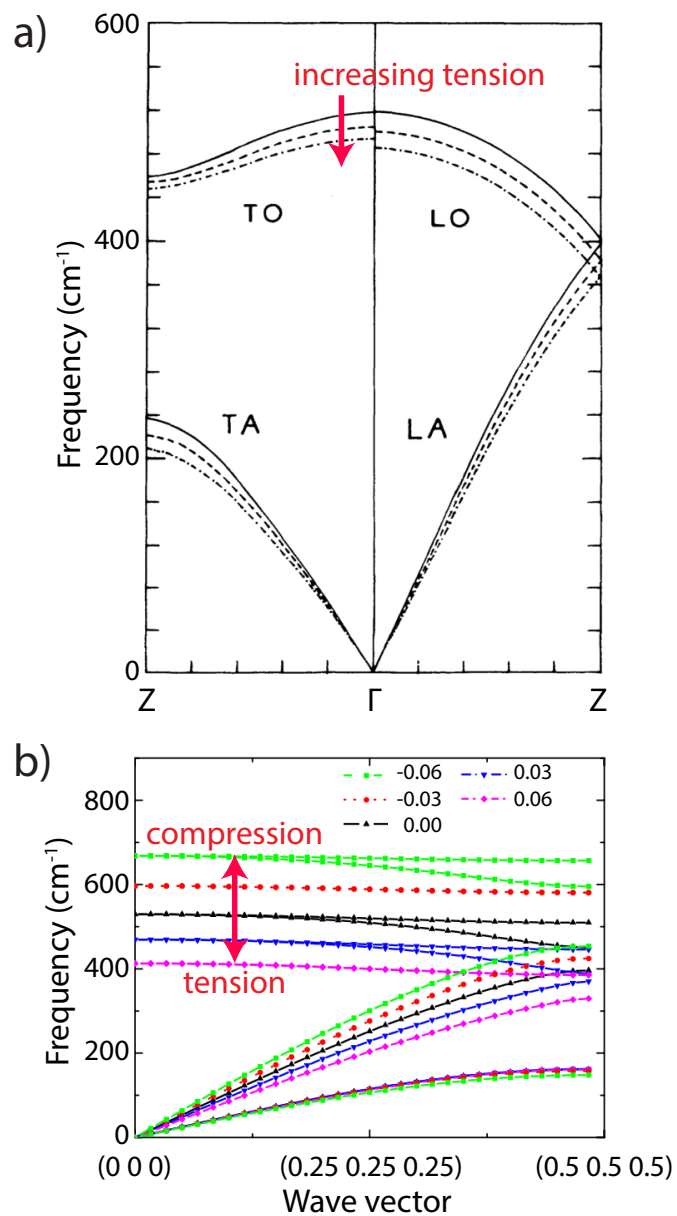


Figure 1.4: Theoretical phonon dispersion curves for Si under strain. a) From Ref. 41, dispersion along [001] for increasingly biaxially strained Si. The magnitudes of the strains were not stated. Copyright 1992 American Physical Society. b) From Ref. 42, dispersion along [111] for hydrostatically strained Si. “-” denotes compressive strain and “+” denotes tensile. Copyright 2010 American Physical Society.

We begin with the heat capacity, which scales for harmonic oscillators as²⁶

$$C \sim \sum_p \int \frac{\omega^2 \exp\left(\frac{\hbar\omega}{kT}\right)}{\left(\exp\left(\frac{\hbar\omega}{kT}\right) - 1\right)^2} D_p(\omega) d\omega \quad (1.13)$$

where \hbar , k are the reduced Planck and Boltzmann constants, respectively, the summation is over all polarizations p , the integral is over the wavenumbers, and $D_p(\omega)$ is the density of states.²⁶ Within the Debye model for diffusive transport, the density of states is proportional to ω^2 , so then the predicted decrease in phonon frequencies with tensile strain will decrease heat capacity, thereby decreasing thermal conductivity.

The strain effect on group velocity may be understood via changes in density and the elastic constants with strain. The weighted average phonon velocity for an isotropic solid is

$$v = \left[\frac{1}{3} \left(\frac{1}{v_l^3} + \frac{2}{v_t^3} \right) \right]^{-\frac{1}{3}} \quad (1.14)$$

where the velocity of the longitudinal phonon is $v_l = \sqrt{C_{11}/\rho}$ and the velocity of the transverse phonons is $v_t = \sqrt{C_{44}/\rho}$.⁴⁴ The C_{ij} are components of the elastic stiffness tensor (the inverse of the compliance tensor described in Section 1.1), and ρ is density. For real, anisotropic solids, one would need to calculate the weighted v for the three directions. The decrease in phonon frequency with tensile strain implies a decrease in stiffness, so we would expect the components of C to decrease with tensile strain. Density will also decrease, but for Si the change in ρ has shown to be relatively small compared to the change in C ,^{42, 45} so, overall, phonon velocity decreases.

The effects of strain on most scattering processes are not well-studied, but we can examine the dependence of scattering time on phonon frequency. The scattering mechanisms most relevant to single-crystal Si are point-defect scattering (e.g. scattering from an isotope, dopant, or vacancy), boundary scattering, phonon-electron scattering, and phonon-phonon scattering (we ignore the momentum-conserving normal processes here and consider only Umklapp scattering). The scattering times associated with these mechanisms are related to frequency as^{28, 46}

$$\tau_{\alpha, \text{point defect}} \sim \omega_{\alpha}^{-4} \quad (1.15)$$

$$\tau_{\alpha, \text{phonon-electron}} \sim \omega_{\alpha}^{-1} \quad (1.16)$$

$$\tau_{\alpha, \text{Umklapp}} \sim \frac{1}{T} \omega_{\alpha}^{-2} \quad (1.17)$$

The boundary scattering dependence on frequency is due to the surface roughness,^{34, 47} which we would not expect to change significantly with strain. The effect of changing phonon frequencies on τ_{boundary} would therefore depend strongly on the sample surface quality. We note that $\tau_{\text{phonon-electron}}$ is also dependent on effective mass, which should be affected by strain, the sign of which depends on the direction of the applied stress and the doping of the sample.¹⁹ However, this scattering mechanism is generally much weaker than the others²⁸ and shows the weakest dependence on phonon frequency. In both cases, tensile strain, which decreases phonon frequencies, would increase scattering time and hence increase thermal conductivity. The Umklapp scattering will

further depend on strain via changes in vibrational anharmonicity. It has been shown that the Umklapp scattering time scales as

$$\tau_{\alpha, \text{Umklapp}} \sim \frac{1}{T} \left(\frac{V}{V_0} \right)^{-2(\gamma_{\alpha} + b)} \quad (1.18)$$

where b depends on how interatomic force constants change with strain and V/V_0 is the volumetric strain.⁴⁴ γ_{α} is the Grüneisen parameter for mode α , which relates changes in frequency to unit cell volume:

$$\gamma_{\alpha} = - \frac{\partial(\ln \omega_{\alpha})}{\partial(\ln V)} \quad (1.19)$$

Since V/V_0 is > 1 in tension and γ_{α} is positive, Equation 1.18 implies $\tau_{\alpha, \text{Umklapp}}$ decreases with tensile strain. Tensile strain will therefore increase or decrease $\tau_{\alpha, \text{Umklapp}}$ depending on which scaling factor (Equations 1.17 or 1.18) is stronger.

With tensile strain we therefore have a competition between terms which decrease thermal conductivity with tensile strain (heat capacity, phonon velocity, anharmonic effects on Umklapp scattering time) and those which increase thermal conductivity (frequency effects on scattering time). The relative magnitudes of these effects depend on, among other things, doping, carrier concentration, defects, isotope content, and temperature. The terms which are most affected by strain may therefore have the least effect on overall thermal conductivity, so comprehensive simulations and experiments are needed to fully understand the effects of strain on thermal conductivity of real

materials.

Performing experimental measurements of elastic strain-mediated thermal conductivity is difficult due to the complexity of simultaneously applying and measuring stress or strain, heating, and measuring temperature, though a handful of experiments have been performed for inorganic solids. To our knowledge the first measurement was performed in 1962 by Keyes and Sladek, who determined the strain dependence of single-crystal doped Ge thermal conductivity at low temperatures. The researchers found that uniaxial tensile strain increased or had no effect on thermal conductivity, with strong dependence on dopant type and concentration as well as orientation, contrary to the expectation described above. They attributed these results to changes in donor wave functions which affect phonon scattering, so this is an electronic effect unrelated to our prior analysis. Ross *et al.* reviewed studies of bulk materials up to 1984 and found that for a wide variety of both metallic and nonmetallic materials, thermal conductivity was positively correlated with increasing hydrostatic pressure.⁴⁸ Andersson and Bäckström in 1988 studied single-crystal Si under hydrostatic pressure and found a weak, but similarly positive correlation.⁴⁹ More recent experiments measured thermal conductivity in bulk Si under uniaxial compression⁵⁰, bulk muscovite⁵¹ and MgO⁵² under hydrostatic compression, and Al and SiN_x thin films under uniaxial tension,⁵³⁻⁵⁵ and in all cases thermal conductivity was positively correlated with compressive stress, as we would expect.

Although experimental studies of the thermal conductivity dependence on strain

are sparse for bulk and thin films and nonexistent for nanowires, thorough studies using molecular dynamics (MD) have been completed. Simulation-based reports make use of the Green-Kubo equation, which relates kinetic to equilibrium properties via an equilibrium correlation (autocorrelation) function. The Green-Kubo relation for (scalar) thermal conductivity takes the form⁵⁶

$$\kappa = \frac{V}{2k_B T^2} \int_0^\infty \langle \vec{j}(t) \cdot \vec{j}(0) \rangle dt \quad (1.20)$$

where V is volume, k_B is Boltzmann's constant, \vec{j} is heat current density, and t is time.

The first attempt to understand the effect of applied stress or strain on thermal conductivity was performed by Picu *et al.*, who modeled an fcc lattice using a Lennard-Jones potential and the heat flux as:⁵⁷

$$\vec{j}(t) = \frac{1}{2V} \sum_{i=1}^N \sum_{k=1}^N \vec{r}_{ik} (\vec{F}_{ik} \cdot \vec{v}_i) \quad (1.21)$$

where \vec{r}_{ik} , \vec{F}_{ik} are the vector distance and the force acting between atoms i and k , respectively, and \vec{v}_i is the velocity of atom i . Under 3% hydrostatic strain in tension and compression they observed a 40% reduction and 100% increase, respectively, with the asymmetry arising from the form of the interatomic potential. For plane strain they observed similar trends, but for plane stress, in which the lattice was allowed to relax in the out-of-plane direction, the researchers observed a weak (<10%) dependence

of the thermal conductivity on strain. They attributed the effect to a combination of changes in stiffness (and hence velocity) and an increase in scattering rate due to lattice anharmonicity, both of which occur since a Lennard-Jones solid displays significant nonlinear elasticity. In a later study, Bhowmick and Shenoy⁴⁴ reported similar trends for a Lennard-Jones solid under hydrostatic strain and attributed the decrease in thermal conductivity to reduction of phonon velocity due to the volumetric strain and an increase in lattice anharmonicity leading to a decrease in $\tau_{Umklapp}$.

Molecular dynamics studies of Si have been performed by Li *et al*⁴² and Yang *et al*.⁴⁵ Li *et al* used MD to examine the effect of strain on thermal conductivity of Si and diamond in bulk, thin film, and nanowire form. Their results showed a less-dramatic strain effect for Si and diamond than for a Lennard-Jones solid: 3% hydrostatic strain yielded a reduction in κ for bulk Si of 18%. In the case of nanowires, the effect was even more subtle, with a 3% reduction in κ with 3% tensile strain for a 4 nm-diameter Si nanowire. They attributed their thermal conductivity changes to shifts in the phonon dispersion curves with tensile strain which lower phonon frequencies, leading to decreases in heat capacity and phonon velocity. More recently, Yang *et al.* modeled 13 nm-thick Si thin films and found a $\sim 9\%$ decrease in thermal conductivity for every 3% in-plane biaxial strain. They attributed this change to decreases in phonon velocity. Results from both studies may be seen in Figure 1.5. Taken as a whole, our intuitive understanding of thermal transport based on changes in heat capacity, phonon velocity and scattering time combined with the results of MD simulations suggest that we

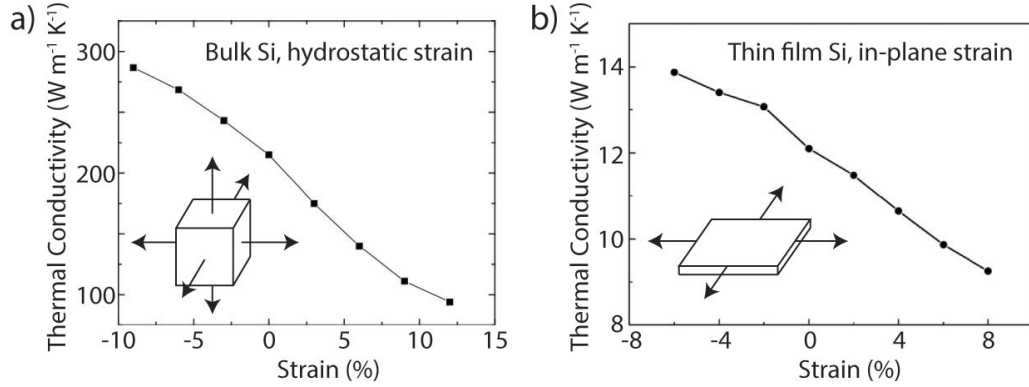


Figure 1.5: MD predictions of strain effects on Si thermal conductivity. a) From Ref. 42, thermal conductivity as a function of hydrostatic strain in bulk Si. Copyright 2010 American Physical Society. b) From Ref. 45, thermal conductivity as a function of biaxial strain in thin film Si. Copyright 2014 Elsevier.

should expect thermal conductivity to decrease with increasing uniform tensile strain.

However, the extent is not clear, motivating the need for experiments on real materials.

1.2.3. Nonuniform Strain Effects on Thermal Conductivity

The effect of heterogeneous states of strain on thermal conductivity is far less well-understood than the uniform strain effect, though many systems known to feature such states of strain have reduced thermal conductivities compared to their homogeneously strained counterparts. However, the effect of the nonuniform strain present in these systems is not readily experimentally decoupled from other effects which may also be responsible for the change in thermal transport. For instance, Si/Ge superlattices—alternating layers of epitaxially grown Si and Ge—have lower thermal conductivity than their alloy counterparts.⁵⁸ Due to a slight lattice mismatch, each

layer of a superlattice has some strain gradient through its thickness which may be responsible for a large portion of the thermal conductivity reduction,⁵⁹ but the strain effect is experimentally difficult to isolate from the effect of boundary scattering from interfaces. Similarly, dislocations effectively scatter phonons due to long-range strain fields as well as mass difference at the core of a dislocation line.^{28, 60} The strain field is predicted to affect thermal transport via an increase in vibrational anharmonicity and hence increased phonon scattering,⁶⁰⁻⁶² but this effect has never been experimentally isolated.

We may also consider point defects such as vacancies or impurity atoms, which create large local strains which decay away from the defect, creating large strain gradients. MD simulations predict the atoms around a vacancy cluster in Si to be distorted by as much as 17%⁶³ and for thermal conductivity to decrease with increasing vacancy concentration,^{64, 65} though it is not yet clear which of the various mechanisms responsible for point defect scattering dominate, again due to the difficulty of decoupling them. These mechanisms include mass-difference, change in bond strength, and strain, and their relative weights are typically calculated Klemens' formulation:⁶⁰

$$\tau_{\text{point defect}}^{-1} = \frac{3a^3}{G} \frac{\omega^4}{\pi v^3} (S_{\text{mass}}^2 + (S_{\text{bond}} + S_{\text{radius}})^2) \quad (1.22)$$

where the S terms are the scalar weights of the various scattering mechanisms, with

the strain effect treated as a local change in atomic radius. Here a^3 is the volume of one atom, G is the number of atoms in the crystal (so Ga^3 is the volume of the crystal), ω is phonon frequency, and v is phonon velocity. Klemens treats the medium as isotropic and averages over all modes for simplicity. Although Klemens' model has remained the most common framework by which the weights of the various scattering mechanisms for point defects have been evaluated for over half a century, it contains some clear and obvious flaws. The most troublesome is the treatment of the strain effect as simply a change in radius. This treatment may be apt for substitutional dopants or isotopes but is clearly insufficient for vacancies or interstitials, which cause significant atomic rearrangement and furthermore tend to cluster.^{63, 66} Although many reports (see, e.g., Refs. 67–70) rely with some success on Klemens' formulation, the need for a more robust model for the mechanisms behind phonon scattering from strain gradients—or a means of experimentally decoupling these mechanisms—is obvious.

1.3. Raman Spectroscopy of Crystalline Solids

In this work, we study strain effects on thermal conductivity using Raman spectroscopy, an optical technique which examines vibrational properties of a material; as such, it may be used to measure quantities such as strain or temperature. In a typical Raman experiment a monochromatic laser is focused on a sample, and peaks in the spectrum of inelastically scattered light correspond to optically-excited phonon modes. For a vibrating lattice in an oscillating electric field \vec{E} , we can write the

induced dipole vector \vec{p} as

$$\vec{p} = \overset{\leftrightarrow}{\alpha} \cdot \vec{E} \quad (1.23)$$

where $\overset{\leftrightarrow}{\alpha}$ is the polarizability tensor.⁷¹ $\overset{\leftrightarrow}{\alpha}$, and hence \vec{p} , is a function of interatomic displacement—as the lattice vibrates, $\overset{\leftrightarrow}{\alpha}$ changes. Expanding $\overset{\leftrightarrow}{\alpha}$ in a Taylor series about the equilibrium atomic displacement, we have

$$\alpha_{\rho\sigma} = (\alpha_{\rho\sigma})_0 + \sum_k \left(\frac{\partial \alpha_{\rho\sigma}}{\partial Q_k} \right)_0 Q_k + \frac{1}{2} \left(\frac{\partial^2 \alpha_{\rho\sigma}}{\partial Q_k \partial Q_l} \right)_0 Q_k Q_l + \dots \quad (1.24)$$

where the $(\alpha_{\rho\sigma})_0$ are the components of $\overset{\leftrightarrow}{\alpha}$ at equilibrium and the Q_k, Q_l, \dots are displacement amplitudes associated with modes of frequency $\omega_k, \omega_l, \dots$ with summation over all normal modes. For atomic vibrations of amplitude Q_{k0} , frequency ω_k , and phase factor δ_k and an electric field \vec{E} and frequency ω , we can write $Q_k = Q_{k0} \cos(\omega_k t + \delta_k)$ and $\vec{E} = \vec{E}_0 \cos(\omega t)$. Plugging these expressions and Equation 1.24 into Equation 1.23, we have

$$\begin{aligned} \vec{p} &= \overset{\leftrightarrow}{\alpha}_0 \vec{E}_0 \cos(\omega t) + \overset{\leftrightarrow}{\alpha}'_k \vec{E}_0 Q_{k0} \cos(\omega_k t + \delta_k) \cos(\omega t) \\ &= \overset{\leftrightarrow}{\alpha}_0 \vec{E}_0 \cos(\omega t) + \frac{1}{2} \overset{\leftrightarrow}{\alpha}'_k \vec{E}_0 Q_{k0} \cos(\omega t - \omega_k t - \delta_k) \\ &\quad + \frac{1}{2} \overset{\leftrightarrow}{\alpha}'_k \vec{E}_0 Q_{k0} \cos(\omega t + \omega_k t + \delta_k) + \dots \end{aligned} \quad (1.25)$$

So we have an oscillating dipole which will emit light at the frequency of the oscillation; the first term on the very right-hand side of this equation corresponds to elastic (Rayleigh) scattering, while the second and third terms are due to inelastic scattering

to lower (Stokes) or higher (anti-Stokes) photon frequencies.⁷¹ The units of ω here are s^{-1} , but it is important to note that by convention Raman spectra are in units of inverse wavelength or spatial frequency, cm^{-1} , which is linearly proportional to frequency.

1.3.1. Strain Effects on the Si Raman Spectrum

Strain affects the Raman spectrum of crystals via a loss of phonon degeneracy and changes in phonon frequency. The wavenumbers of visible light are orders of magnitude smaller than crystalline Si's Brillouin zone, so Raman spectroscopy probes phonons at the Brillouin zone center (wavenumber $q \sim 0$). This means we are examining only the optical phonons since the frequency of acoustic phonons goes to zero at the center of the Brillouin zone. In order to understand the effect of strain on the Raman spectrum, then, we must examine the effect of strain on the frequencies of $q \sim 0$ optical phonons. For an unstrained diamond-structure crystal such as Si, the one longitudinal and two transverse optical phonons are triply degenerate where $q \sim 0$, yielding a single peak in the Raman spectrum (centered near 521 cm^{-1} in the case of Si). The application of uniaxial or biaxial strain breaks this degeneracy, producing two or three separate (nondegenerate) modes of different frequencies than the unstrained, degenerate modes.

The effect of strain on the Raman spectrum depends on the polarization of incident and scattered light, the direction of strain, and the orientation of the scattering surface. For diamond-structure crystals with strain tensor $\overleftrightarrow{\epsilon}$, the Raman shift with strain may

be found using the secular equation derived by Ganesan *et al.*⁷²:

$$\begin{vmatrix} p\epsilon_{11} + q(\epsilon_{22} + \epsilon_{33}) - \lambda & 2r\epsilon_{12} & 2r\epsilon_{13} \\ 2r\epsilon_{12} & p\epsilon_{11} + q(\epsilon_{22} + \epsilon_{33}) - \lambda & 2r\epsilon_{23} \\ 2r\epsilon_{13} & 2r\epsilon_{23} & p\epsilon_{11} + q(\epsilon_{22} + \epsilon_{33}) - \lambda \end{vmatrix} = 0 \quad (1.26)$$

where $\lambda = \omega_1^2 - \omega_0^2$ where ω_1 is Raman frequency (in units of cm^{-1}) with strain and ω_0 is Raman frequency without strain. Since $\Delta\omega = \lambda/2\omega_0$, we may obtain the Raman shift with stress from the eigenvalues. The phonon deformation potentials p , q , and r relate phonon frequencies to strain and have been calculated using Raman data for strained Si by various groups;⁷³⁻⁷⁷ the most recent and comprehensive of these reports gives $p = -1.56\omega_0^2$, $q = -1.98\omega_0^2$, and $r = -0.96\omega_0^2$, in good agreement with previous measurements and which we will use here.

The secular equation is given in the reference system ($x=[100]$, $y=[010]$, $z=[001]$), but in this work we consider uniaxial stress applied along the $[110]$ and $[111]$ directions, so the strain tensor components ϵ_{ij} must be determined using Hooke's Law

Stress direction	ϵ_{11}	ϵ_{22}	ϵ_{33}	ϵ_{12}	ϵ_{13}	ϵ_{23}
$[100]$	PS_{11}	PS_{12}	PS_{12}	0	0	0
$[110]$	$\frac{P(S_{11}+S_{12})}{2}$	$\frac{P(S_{11}+S_{12})}{2}$	PS_{12}	$\frac{PS_{44}}{4}$	0	0
$[111]$	$\frac{P(S_{11}+2S_{12})}{3}$	$\frac{P(S_{11}+2S_{12})}{3}$	$\frac{P(S_{11}+2S_{12})}{3}$	$\frac{PS_{44}}{6}$	$\frac{PS_{44}}{6}$	$\frac{PS_{44}}{6}$

Table 1: Non-zero components of the strain tensor for a diamond-structure crystal with a uniaxial load where the principal axes are $[100]$, $[010]$, $[001]$.

(Equation 1.4) in the reference system. The strain components for a uniaxial stress of magnitude P applied along the $[100]$, $[110]$, and $[111]$ directions are given in Table 1. For a cubic crystal the only nonzero components of the compliance tensor are S_{11} , S_{12} , and S_{44} , with values for Si of 7.68, -2.14, and 12.6 TPa^{-1} , respectively.⁷⁸ Solving the secular equation for stress along these directions yields three eigenvalues and hence three phonon modes, two of which are degenerate for stress along $[100]$ or $[111]$. Observation of these modes in the Raman spectrum will depend on the polarization of incident and scattered light as well as the backscattering surface; for stress along $[100]$, $[110]$, and $[111]$ with light polarized along the direction of tension and backscattering from the (100) , (100) , and (112) surfaces, respectively, we expect to observe shifts of -2.0, -2.0, and -3.7 cm^{-1} , respectively. These shifts have been verified by various

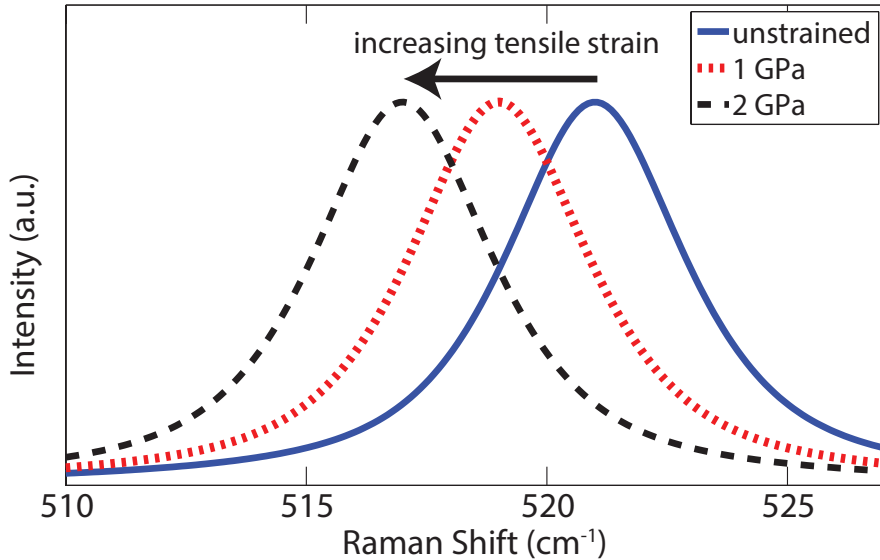


Figure 1.6: Predicted Raman spectra for Si under stress along the $[100]$ direction. 1 GPa of stress corresponds to 0.77% strain.

groups: by Anastassakis *et al.*⁷³ for stress along [100] and [111] and Peng *et al.* for stress along [110],⁷⁶ and will be used to measure strain in later chapters. Examples of the predicted changes in the Raman spectrum of Si with applied uniaxial tensile stress may be seen in Figure 1.6b.

1.3.2. Temperature Effects on the Si Raman Spectrum

Increasing temperature affects the first-order Raman spectrum of Si in three respects: downshifted peak position, broadened peak width, and reduced Stokes/anti-Stokes ratio. The experiments discussed in this work will rely on the shift in peak position, which yields the most precise temperature measurements, so we will focus on those shifts here. As with the strain effects on the Raman spectrum, temperature effects may also be understood by examining the effect of temperature on the frequencies of optical phonons at the Brillouin zone center. These frequencies change with temperature due to thermal expansion or contraction and a resulting change in interatomic potential; they are thus independent of orientation and hence light polarization. The shifts were first calculated by Cowley⁷⁹ and experimentally verified by Hart *et al.*⁸⁰ More recently, Doerk *et al.*⁸¹ showed that the temperature-dependent Raman shifts in Si nanowires are identical to bulk at $-0.022 \text{ cm}^{-1} \text{ K}^{-1}$ near room temperature. For typical Raman systems which can measure the position of Si peaks with precision on the order of $0.01\text{-}0.1 \text{ cm}^{-1}$ this implies temperature measurements are precise to within a few degrees.

1.4. Summary and Thesis Outline

We have seen that uniform and nonuniform strain may be used to tune thermal conductivity of Si nanostructures, but that these effects have not yet been experimentally assessed. We have furthermore seen that Raman spectroscopy is a valuable tool for measuring temperature and strain in Si. In this dissertation, we will present Raman-based measurements of thermal conductivity in Si nanostructures as a function of uniaxial tensile strain as well as more complicated strain states. We will begin with uniaxial tensile tests on nanowires, discuss the novel method of measuring thermal conductivity of such wires, and then extend the method to irradiated wires, strained thin films, and strained nanomesh structures. We will conclude with future prospects for nanoscale strain engineering of thermal conductivity and new applications of the Raman-based method.

Chapter 2

Tensile Testing of Nanowires

Portions of this chapter have been reproduced with permission from Nanotechnology, Volume 24, Issue 23, Page 235704. Copyright 2013 Institute of Physics.

In order to determine the strain dependence of the thermal conductivity of nanowires we must first develop a controllable, repeatable method of dynamically applying displacement and measuring load in an individual nanowire. The simplest and most easily interpretable state of strain is uniaxial tension, but it is also among the most difficult to achieve in that it requires the development of actuators and load cells with nm and nN resolution, respectively, as well as means of transferring, aligning, and gripping individual nanowires. In this chapter we will present a method of obtaining stress-strain curves of individual nanowires, with special attention paid to proper measurement of strain when using compliant gripping materials. We will discuss results of uniaxial tensile tests on three species of semiconductor nanowires and prospects for further improving measurements of nanoscale mechanical behavior.

2.1. Materials and Methods

Several species of inorganic nanowires were used in this study, including two distinct types of Si nanowires. The first set of Si nanowires were $\langle 100 \rangle$ -oriented,

fabricated using a top-down metal-assisted chemical etching (MACE) method in which nanowire diameters were defined using electron beam lithography on (100) Si wafers. Following patterning, approximately 15 nm of Au was deposited using electron beam evaporation and wafers were etched in a solution of peroxide and HF following the methods of Refs. 36, 82. The Au layer catalyzed the oxidation and removal of Si at the Au-Si interface, leaving nanowires wherever the Au did not contact the Si. The first etch step left thin, cobweb-like Si filaments in addition to the patterned nanowires due to discontinuities in the Au film, so the wafers were then oxidized in a tube furnace and etched in HF to remove the unwanted filaments. The second set of Si nanowires were undoped, $\langle 111 \rangle$ -oriented, vapor-liquid-solid (VLS)-grown purchased from Sigma Aldrich with nearly monodisperse diameters in the range of 170-180 nm. We performed additional mechanical tests on various nanowires received from collaborators. $\langle 10\bar{1}0 \rangle$ -oriented $\text{Ge}_2\text{Sb}_2\text{Te}_5$ (GST) nanowires^{83, 84} 115-280 nm in diameter and $\langle 110 \rangle$ -oriented GeTe nanowires⁸⁵ 100-128 nm in diameter were grown using VLS by Prof. Ritesh Agarwal, Pavan Nukala, and Rahul Agarwal at Penn. $\langle 110 \rangle$ -oriented Pd nanowires grown using a method based on molecular beam epitaxy (MBE)⁸⁶ 33-100 nm in diameter were supplied by Dr. Gunther Richter at the Max Planck Institut in Stuttgart, Germany. Mechanical testing of Pd nanowires was performed by Lisa Chen at Penn. Images of Si, $\text{Ge}_2\text{Sb}_2\text{Te}_5$, and GeTe nanowires prior to harvesting may be seen in Figure 2.1. All nanowires were single-crystalline, with orientation of VLS- and MBE-grown nanowires verified using selected area electron

diffraction. Top-down Si nanowires took the orientation of the host wafer from which they were grown.

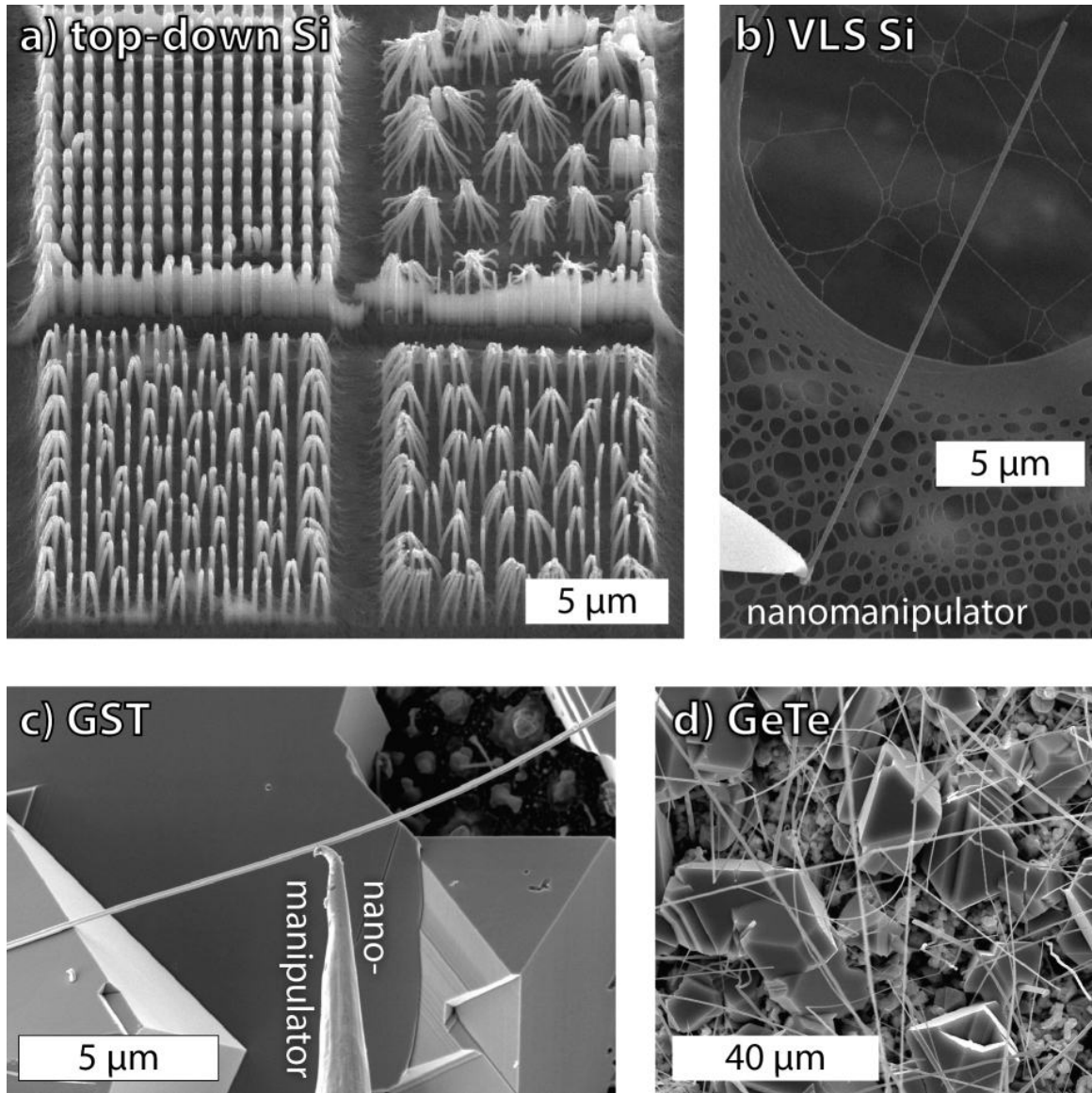


Figure 2.1: Semiconductor nanowires used for mechanical testing. a) Top-down Si NWs with controlled diameters. b) A single VLS nanowire on a holey carbon grid and attached to a nanomanipulator. c) A GST nanowire as grown, with a nanomanipulator in contact but not yet attached. d) As-grown GeTe nanowires.

In order to apply uniaxial tension we transferred individual nanowires to a microelectromechanical systems (MEMS) -based tensile testing device fabricated at the Center for Integrated Nanotechnologies (CINT). Trenches were milled into the grips of the device using a focused ion beam (FIB) to aid in alignment of the specimen with the tensile axis. The device consisted of a thermal actuator and a compound flexure load cell, as shown in Figure 2.2a. Actuation was controlled by applying voltage across the actuator (electrically and thermally isolated from the sample by a thin SiN_x strip) with a Keithley 2636A source measure unit (SMU). The applied voltage induced a current, and the slender, angled beams thermally expanded due to Joule heating, pulling the two grips apart. We calibrated the actuator by incrementally increasing the voltage across the beams and acquiring an image of the actuator at each increment. Separate calibrations had to be performed for actuation under an optical microscope in ambient conditions or inside a scanning electron microscope (SEM) due to convective heat losses when actuating in air, which affected temperature and subsequently actuator displacement. The image series was analyzed using digital image correlation (DIC) to extract the displacement of the actuator as a function of applied voltage, then inverted to obtain voltage as a function of displacement. We could then produce tables of voltage values which would yield a constant displacement rate during testing. Voltage was controlled during testing using the Keithley SMU and a custom LabView program.

All nanowires were transferred to the testing device from their as-grown state

except for the VLS Si nanowires, which arrived in solution and were first dispersed onto holey carbon grids. Nanowires were harvested inside a SEM by attaching a single nanowire to a tungsten probe (tip radius $<0.1 \mu\text{m}$) on a nanomanipulator (Kleindiek Nanotechnik). The nanomanipulator had three degrees of freedom and its position could be precisely controlled to within $\sim 1 \text{ nm}$. Nanowires which were isolated and lying in the same plane as the MEMS device were chosen for nanomanipulation and testing. After selecting a nanowire, the probe tip was brought into contact such that the interface between the nanowire and probe could be imaged. The nanowire was attached using a small amount of Pt-containing material (precursor of $\text{C}_5\text{H}_4\text{CH}_3\text{Pt}(\text{CH}_3)_3$) deposited using electron beam induced deposition (EBID), as can be seen in Figure 2.1b. Once attached to the nanomanipulator, nanowires were lifted off of the substrates, and the SEM stage was translated to bring the MEMS device into the field of view. The stage was then rotated to align the grips of the device with the nanowire. The wires were lowered into the trenches (except specimens Si B and F and Pd D, E, and H, which were placed flat on the grips) and clamped using EBID (Figure 2.2b). Pt- or W-containing (precursor of $\text{W}(\text{CO})_6$) clamps were deposited at 5 to 20 kV accelerating voltages and 40 pA (for Pt deposition) or 560 pA (for W deposition) beam currents at room temperature. These precursor materials and deposition conditions are known to produce C-rich deposits with Pt content varying from 5 to 16at.%.⁸⁷ In the case of W, the reported metal content for 5 kV accelerating voltage and 1.6 nA beam current— $3\times$ the beam current used here—is about 35at.%.⁸⁸

The deposition time was chosen to produce clamps with thicknesses that exceeded the nanowire diameter. Clamp widths ranged from 0.5 to 1.5 μm and lengths along the wire ranged from 0.3 to 1.8 μm . Once secured, the nanomanipulator was retracted, breaking the relatively weaker bond between the manipulator and the wire without applying stress to the specimen gage section. Details of the wire materials, dimensions, EBID conditions, and clamping configurations for Si, GST, and Pd nanowires are summarized in Table 2.

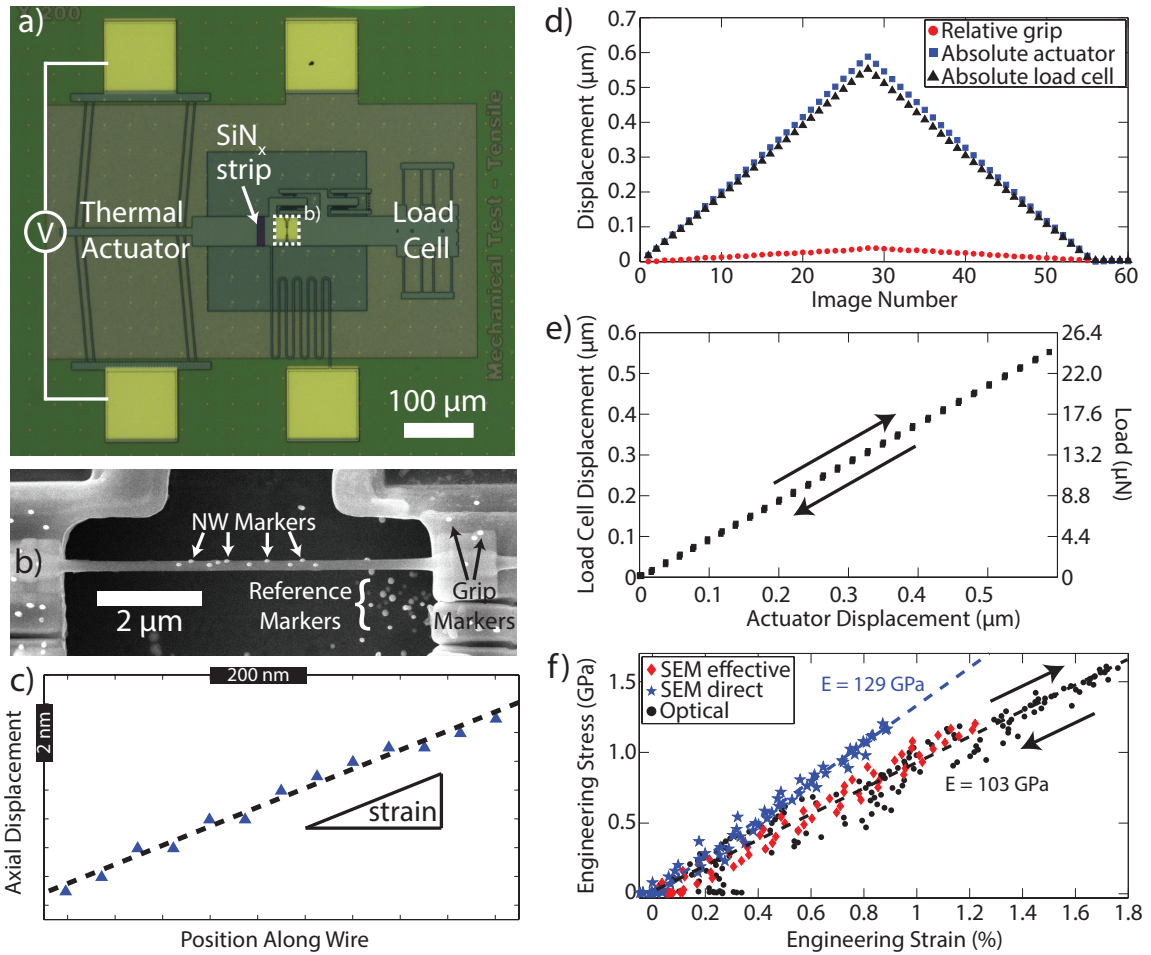


Figure 2.2: Tensile testing method. a) Optical image of MEMS tensile platform employed for *in situ* testing of individual nanowires. b) SEM image showing a Si nanowire suspended across testing grips and secured using EBID clamps. c) Scheme for direct measurement of nanowire strain during testing using digital image correlation of markers providing axial displacements along the gage section of the nanowire. d) Displacements of the actuator, load cell, and relative displacement between them during a single mechanical test on a $\langle 100 \rangle$ -oriented Si nanowire with $d=165$ nm inside a SEM. e) Load-displacement data for the test in (d), from which stress was determined. f) Stress-strain curves using the two strain measurement methods for the same nanowire tested inside a SEM as well as under an optical microscope, where only the effective strain is available. The directly measured strain yields Young's modulus, E , in good agreement with bulk, as we would expect for nanowires of this size. The difference in between the curves produced using the different strain measurement methods is indicative of clamp deformation.

For SEM testing, markers were deposited using EBID on both grips, the substrate, and along the length of the wire spaced far enough apart to prevent load bearing (Figure 2.2b) in order to measure displacement. Strain rates between 10^{-5} s^{-1} and 10^{-4} s^{-1} were applied and a series of images were obtained during testing. Displacements of the deposited markers (SEM testing) or of the MEMS device components (optical testing) were determined from DIC of the image series, yielding resolution better than 0.1 pixels (1 nm in SEM images or 5 nm in optical images). Strain in the nanowires was determined from these displacements in two ways. The “direct” engineering strain was measured from displacement gradients (Figure 2.2c) obtained from the markers placed directly on the nanowire, while the “effective” engineering strain was determined from the relative displacements of the two grips and the original gauge length. Figure 2.2d shows the displacements of the MEMS-based actuator and load cell over the course of a single test; the relative displacement between these two components is the displacement between the grips, from which the effective strain was determined. We note here that when testing under an optical microscope, only the effective engineering strain is accessible. Load was determined by measuring the deflection of the compound flexure load cell, which had stiffness linear in the displacement of 44 N m^{-1} . Displacement of the load cell—and hence load—against displacement of the actuator for the test shown in Figure 2.2d is plotted in Figure 2.2e. From the load-displacement curve, the relative grip displacement, and the geometry of the nanowire we extracted the stress-strain curves seen in Figure 2.2f for both

SEM and optical tests. Young's moduli for all nanowires and all strain measurement methods were determined from the unloading portions of the stress-strain curves.

2.2. Effect of Clamp Deformation on Effective Strain Measurement

The troubling difference between the effective and direct stress-strain curves seen in Figure 2.2f is due to deformation of the EBID clamps. Clamp deformation may influence the effective strain measurement—and any properties which depend on it, such as Young's modulus—in a number of ways. This diversity is highlighted in Figure 2.3a via representative stress-strain curves for Pd, Si, and GST nanowires (GeTe nanowires are not included in the study of clamp deformation due to their large, spatially variant plastic deformation, discussed in a later section). The Pd nanowire shown exhibits an apparent difference in modulus using the two strain measurement approaches, although linear elastic behavior is measured with both strain measurement methods, suggesting a low clamp stiffness relative to the nanowire. In contrast, both slight and extreme apparent hysteresis is detected in the Si and GST stress-strain curves, respectively, that vanishes or diminishes in the stress-strain curves obtained from direct strain measurements. This discrepancy can be attributed to permanent deformation of the clamping material. Without a direct measurement of strain, such stress-strain curves could be improperly interpreted as indicating plastic deformation in the nanowires, when in fact the true material deformation remained entirely (Si)

or mostly (GST) elastic. It is important to note that the stress-strain curves shown in Figure 2.3a do not indicate the behavior observed in *all* nanowires of a particular material system. Specifically, slight hysteresis was observed in some measurements of Pd nanowires, and not all GST nanowires exhibited large hysteresis.

The occurrence of apparent hysteresis in the stress-strain response of many of the tested nanowires, as quantified by measurements of the residual strain upon unloading, can be ascribed to two potential mechanisms. The first is plastic deformation of the gripping material, which would be expected to scale with the load transferred by the nanowire to gripping material. However, measurements of the residual grip displacement normalized by the total applied displacement show an inverse correlation. For instance, contacts used for Si and GST nanowires had similar interfacial areas, yet Si nanowires showed the lowest hysteresis despite incurring the largest forces during testing. A second proposed mechanism is interfacial sliding (i.e. pull out) of the nanowire relative to the grips, which presumably depends on the nature of the interfacial bonding. Indeed, the normalized residual displacements showed differences between the three materials (Figure 2.3b), with GST and Si showing the highest and lowest values, respectively. However, further experiments would be needed to validate this hypothesis with greater statistical significance.

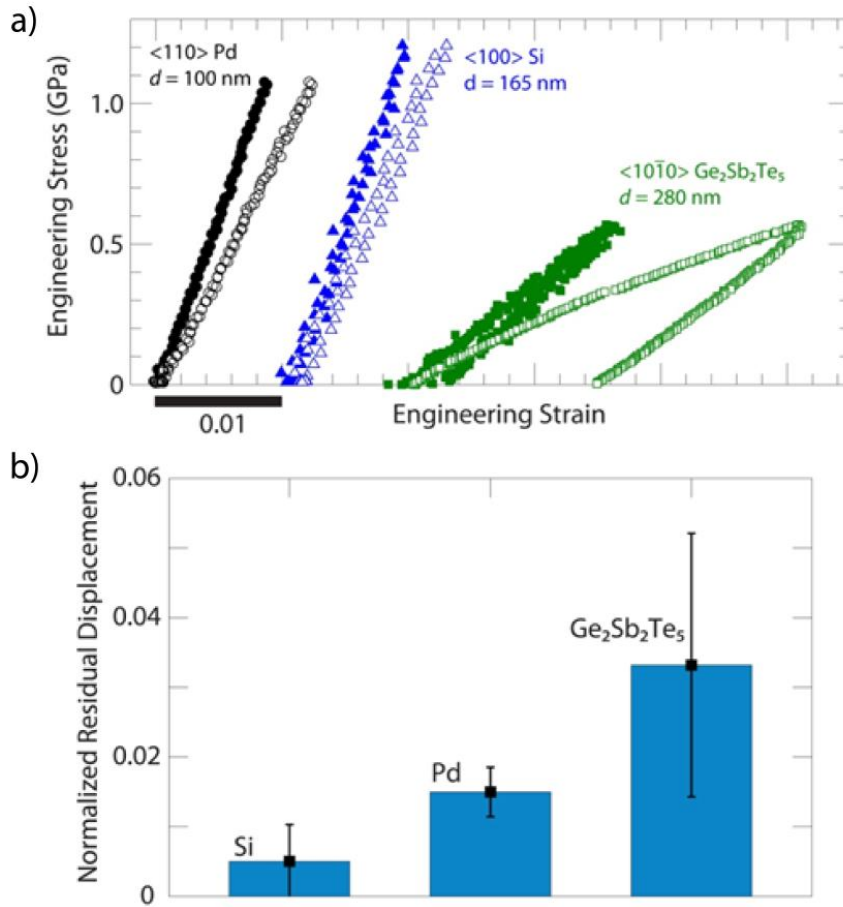


Figure 2.3: Stress strain curves of inorganic nanowires. a) Stress strain curves for nanowires composed of three different inorganic materials highlighting differences between apparent (open markers) and true (closed markers) response upon directly measuring strain within the specimen gage section. Curves for different materials are shifted along the strain axis for clarity. Young's moduli were measured from the unloading portion of the stress-strain curves. b) In cases where apparent hysteresis was detected, the residual displacement upon unloading normalized by the total applied displacement for the three different tested materials. The apparent material dependence on the residual displacement is consistent with an interfacial sliding mechanism.

Measurement of both effective and actual Young’s moduli allows for determination of the mean single contact stiffness,

$$k_{\text{contact}} = 2 \left(\frac{1}{k_{\text{apparent}}} - \frac{1}{k_{\text{wire}}} \right)^{-1} \quad (2.1)$$

where $k_{\text{apparent}} = AE_{\text{apparent}}/L$ and $k_{\text{wire}} = AE_{\text{direct}}/L$, with A and L the cross-sectional area and length of the nanowire, respectively, and E_{apparent} and E_{direct} the moduli determined using the strain from grip displacement and the directly-measured strain, respectively. This model provides insight on the influence of the contact stiffness on the apparent elastic response. Namely, the ratio of contact to nanowire stiffnesses must be greater than 18 to yield better than 90% accuracy in measurement of Young’s modulus (approximately within our experimental uncertainty considering force and area measurement, see Ref. 89), as shown in Figure 2.4. The resulting stiffnesses, moduli, and errors for Si, Pd, and GST nanowires using the two methods of measuring strain are summarized in Table 2. By varying the nanowire material and geometry we achieved nanowire stiffnesses that varied by over an order of magnitude (0.07 to 2.4 kN m⁻¹). In total, we found that clamp compliance led to errors in modulus greater than 10% for 14 out of the 17 samples tested, while errors less than 10% were only observed for nanowires with stiffness below approximately 0.3 kN m⁻¹. Contact stiffness was found to be invariant with load for each test, and displayed no correlative trends with contact length along the wire, accelerating voltage during deposition, or nanowire material. No strong correlation was measured between contact stiffness and

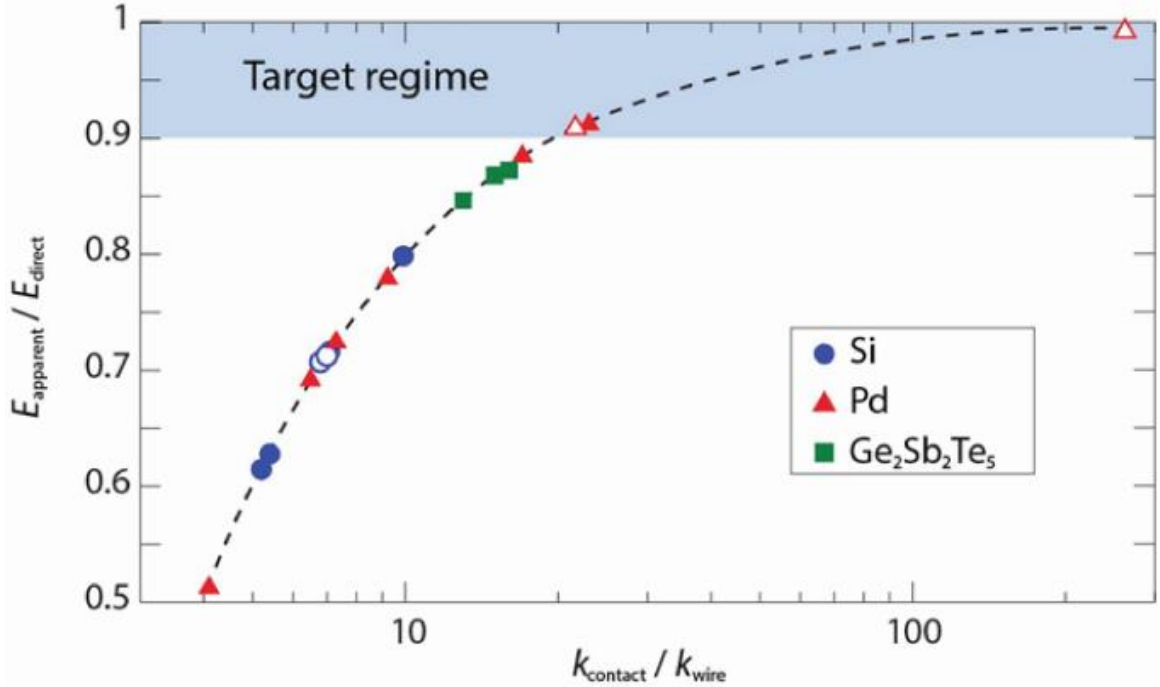


Figure 2.4: Ratio of apparent to direct measurements of Young’s moduli during tensile testing of 3 different inorganic nanowires vs. ratio of contact to wire stiffness. Open symbols denote flat-geometry contacts. The shaded region denotes the optimal range where measurements using remote displacement sensing modes give a value of E_{apparent} that are within 10% of E_{direct} according to Equation 2.1.

beam power, which is known to control the overall metal content in such deposits.

For all wires in which the clamping geometry was flat, the contact stiffness was approximately equal to (in the case of Si) or greater than or equal to (up to an order of magnitude in the case of Pd) that of the trenched geometry contacts. We ascribe this to the lack of contact in the trenched geometry between the nanowire and the grips such that they were surrounded on all sides by EBID material (see Figure 2.5). For Pd nanowires, using a flat clamping geometry sufficiently increased the clamp stiffness such that E_{apparent} was within 1% of E_{direct} . However, for the Si

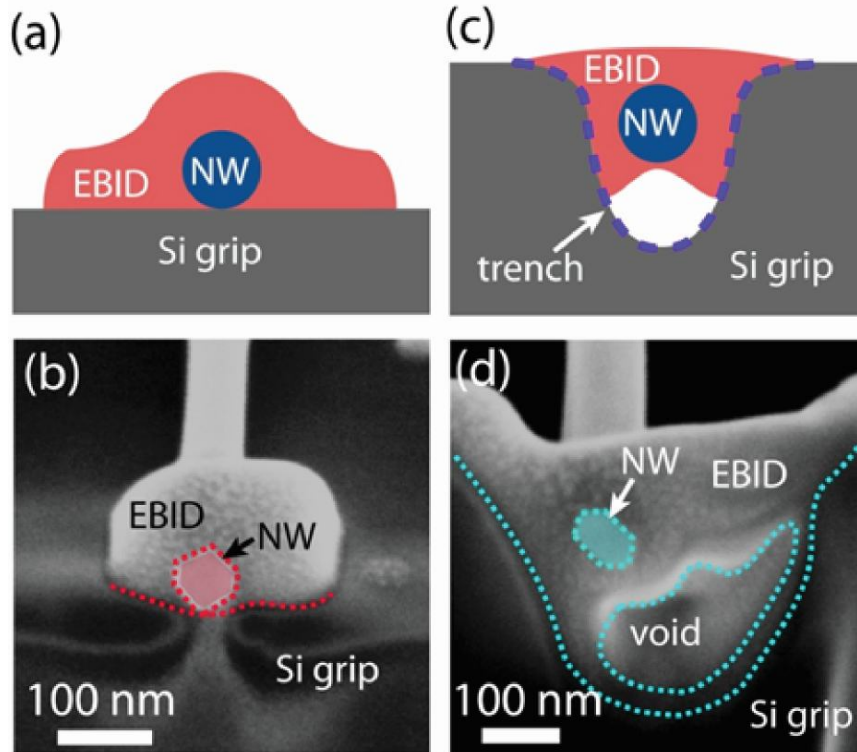


Figure 2.5: Schematics (a,c) and SEM images (b,d) of FIB-polished cross sections of Pd nanowires (NW) clamped to a flat surface (a,b) and in a trench (c,d). NWs in trenches do not often touch the bottom but rather make contact with side walls or remain suspended from nearby surfaces, whereas samples clamped to flat surfaces often make direct contact with the Si grips. Figure produced by Lisa Chen.

nanowires, which were much stiffer, the error in measured modulus in the flat clamping configuration was still over 29%. Manipulating a nanowire to the trench geometry is generally more efficient and results in better alignment of the nanowires to the tensile axis, but only one of the trench-geometry tests shown here had error less than 10%.

This motivated several attempts to improve the stiffness of the trenched contacts. A common strategy within the electrical testing community is to improve contacts (i.e. increase electrical conductivity) by increasing their metal content. It has been

shown that the resistivities of EBID deposits of a given material depend on electron accelerating voltage and beam current, which is ascribed to the primary influence of metal content.^{87, 90, 91} Low electrical resistivity implies a percolating metal network, which would imply an increase in contact stiffness since metals are stiffer than the surrounding amorphous carbonaceous matrix. For Pd F, Pt clamps were deposited at 2 kV and 420 pA, which has been reported to increase the metal content from approximately 5at.% (10 or 20 kV and 40 pA) to 16at.%,⁸⁷ below the threshold of 30% by volume (approximately 17at.%) for a percolating network⁹² but sufficiently high to expect a lowering of electrical resistivity by as high as a factor of four.⁹³ Si E was clamped with W-containing EBID material, which is reported (albeit for much larger beam currents than employed in the current study) to have a metal content over 35at.%,⁸⁸ notably above the percolation threshold. Furthermore, bulk W has a Young's modulus more than double that of Pt. Further attempts included annealing a device with Si A (see Table 2) attached in O₂ at 300°C for 10 minutes to increase the metal concentration of the clamp following the methods of Botman *et al.*, which has been shown to decrease the resistivity of the deposits by three orders of magnitude by removing the insulating carbonaceous matrix from between the Pt crystallites such that the metal content rises above the percolation threshold.⁹⁴ Since the annealing step removed most of the contact material, additional material was then deposited on top, resulting in a contact with a significantly higher overall metal content. In all, no trend in contact stiffness with increased metal content was measured, implying that

since the percolation thresholds for electrical and stiff mechanical connectivity are distinct, the metal in the contacts is in the form of particles rather than a continuous network. This suggests that the stiffness of these organometallic composite contacts is dominated by the organic matrix, consistent with the findings of Utke *et al.*⁹⁵

Since varying electron power density has been shown to affect deposition rate and metal content and furthermore shows a saturation in the metal content achievable in typical electron microscopes,⁸⁷ the implication is that the stiffness of the EBID material itself is inherently limited (unlike the contact strength as shown previously), and so the geometry of the deposit must be considered. Accordingly, the lengths of the contacts along the axes of the wires were varied for Si, but the contact stiffness showed no apparent relationship with contact length. Similarly, varying contact width from 470 nm for Pd C to 700 nm for Pd A resulted in nearly identical contact stiffnesses.

On the whole, these limitations on the maximum contact stiffness imply that accurate measurements of strain are favored on longer or thinner, and therefore more compliant, nanowires. The lowest measured contact stiffness was 0.55 kN m^{-1} ; taking this as the minimum possible contact stiffness, the nanowire stiffness must be less than 0.03 kN m^{-1} to yield better than 90% accuracy in modulus measurement. For a nanowire with Young's modulus 100 GPa and diameter 100 nm, this implies a minimum gauge length of approximately $25 \mu\text{m}$, longer than typical tensile testing specimens. This may explain the large scatter in the reported Young's moduli among distinct testing methods, as especially evident where tensile testing yields the lowest

measured modulus⁹⁶ or is systematically lower than bulk values.^{11, 13} Although usage of the apparent strain will only yield values of Young's modulus that are lower than the actual values, it is important to note that observation of nanowire moduli that are higher than bulk does not necessarily indicate that clamp effects are negligible. Indeed, in the case of Pd D, the apparent modulus was higher than bulk, whereas the actual modulus was higher still owing to size-dependent elasticity.⁸⁹ When a sufficiently compliant sample cannot be prepared, local strain measurements such as the method we have described here, selected area diffraction,⁹⁷ or Raman spectroscopy,^{98–103} should be used. Other methods of attaching nanowires to tensile testing setups should also be considered, e.g. deposition of pure metal or semiconductor contact materials by evaporation through a shadow mask, co-fabrication of specimens directly onto testing apparatuses,¹⁰⁴ or nanoscale spot welding.^{105–107}

Wire	d (nm)	L (μm)	Clamp Geometry	Contact Length (μm)	Deposition Voltage (kV)	Beam Current (pA)	k_{wire} (kN/m)	k_{contact} (kN/m)	$k_{\text{contact}}/k_{\text{wire}}$	E_{direct} (GPa)	E_{apparent} (GPa)	Modulus Error
Si <100>A	165	3.2	trench	.80	5	40	.86	6.8	7.9	129	103	20%
Si <100> B	165	1.1	flat	.60	10	40	2.4	12	4.8	123	87	29%
Si <111> C	180	7.1	trench	.65	5	40	.67	2.3	3.4	188	118	37%
Si <111> D	171	7.1	trench	1.8	5	40	.63	3.7	7.1	194	139	25%
Si <111> E	172	7.1	trench ^[a]	1.0	5	560	.63	2.0	3.2	192	118	39%
Si <111> F	176	7.0	flat	1.1	5	40	.76	3.8	7.0	219	156	29%
Pd A	77	7.1	trench	.45	10	40	.08	1.6	21	114	104	9%
Pd B	63	3.0	trench	.45	10	40	.14	1.5	13	139	116	13%
Pd C	100	3.2	trench	.28	20	40	.31	1.6	5.3	127	92	27%
Pd D	33	3.0	flat	.50	10	40	.07	1.1	15	243	215	12%
Pd E	62	3.1	flat	.32	20	40	.13	34	262	132	131	0.7%
Pd F	37	1.47	trench	.58	2	420	.09	.57	6.0	130	97	25%
Pd G	88	3.34	trench	.31	20	40	.21	2.0	9.5	115	95	17%
Pd H	100	3.34	flat	.33	5	40	.29	6.1	21	125	114	9%
Ge ₂ Sb ₂ Te ₅ A	280	3.4	trench	.80	10	40	.71	7.8	11	39	33	16%
Ge ₂ Sb ₂ Te ₅ B	130	6.7	trench	1.0	5	40	.09	1.3	14	47	41	12%
Ge ₂ Sb ₂ Te ₅ C	115	2.8	trench	.38	10	40	.20	2.6	13	53	46	13%

[a] Tungsten-containing deposition used for clamping. All other clamps were platinum-containing. |

Table 2: Geometry of nanowires and EBID clamps used for clamp stiffness determination, in addition to measured values of wire stiffnesses and Young’s moduli. Values of Young’s moduli are tabulated as calculated based on direct measurement of strain in the wire gage section and indirect values based on the relative grip displacement.

2.3. Mechanical Properties of Semiconductor Nanowires

2.3.1. Si Nanowires

Beginning with Si, direct strain measurements showed linear elastic behavior for the entirety of each tensile test, with Young's moduli for Si $\langle 111 \rangle$ and $\langle 100 \rangle$ that are in excellent agreement with the bulk values (188 and 130 GPa, respectively). Size effects on the elastic behavior would be expected to be negligible for Si nanowires with the diameters tested. Indeed, Zhu *et al.* found that nanowire modulus was constant for diameters above 40 nm,¹⁰ and Jin *et al.* found a constant modulus for nanobeams with thickness of 100 nm,¹⁴ consistent with our finding of size-independent elastic behavior for our range of sizes. The notable outlier is Si F, a $\langle 111 \rangle$ nanowire with a measured E_{direct} of 219 GPa, which was due to poor out-of-plane alignment observed in tilted SEM imaging, resulting in an artificially low strain measurement. All other tested wires did not show evident signs of such misalignment. The high stiffness and large diameters of these nanowires, combined with the limited load range of our MEMS devices prevented us from bringing these nanowires to fracture, even at a maximum of 3% strain. The high strength and bulk-like, linear elastic behavior of these nanowires will prove advantageous for the thermal transport measurements discussed in the following chapters.

2.3.2. GST Nanowires

We next consider the behavior of GST nanowires. Errors in the effective strain measurement from clamp deformation were generally small and consistent for these nanowires due to their low stiffness, so most testing was performed under an optical microscope. Representative stress-strain curves using the effective strain measurement for a single 180 nm diameter nanowire may be seen in Figure 2.6a, which was loaded and unloaded twice before loading to fracture. In tests of eleven GST nanowires (three of these inside a SEM) we observed no size effects on Young's modulus, with average 44 ± 5 GPa over all measurements (see Figure 2.6b. This value is likely slightly lower than the actual Young's modulus, by perhaps 12-16%, following Table 2, due to the use of the effective strain measurement. However, this is within the error of our measurements. We were able to measure fracture strengths of seven of these nanowires and also observed no clear dependence on size (see Figure 2.6c), with average fracture strength 1.2 ± 0.3 GPa. All nanowires appeared to undergo brittle fracture with little, if any, plastic deformation.

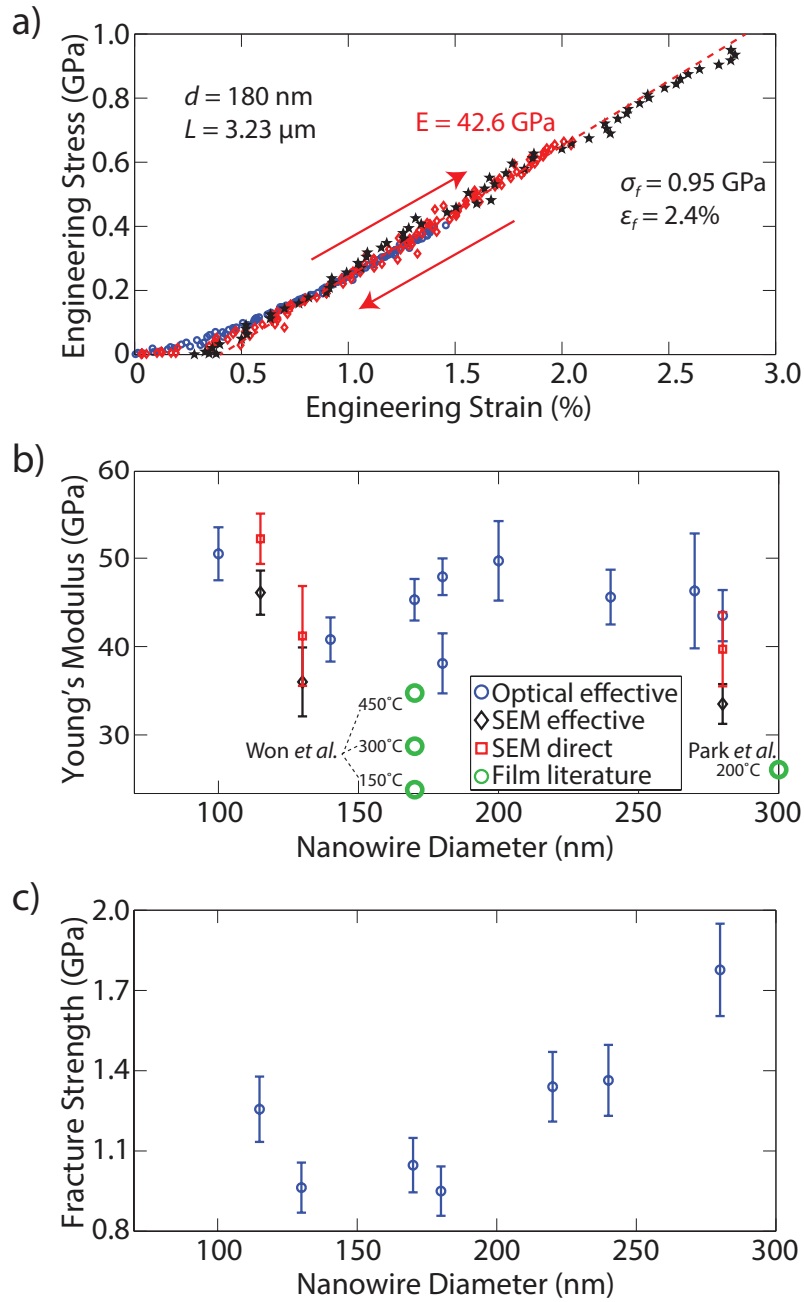


Figure 2.6: Mechanical testing of GST nanowires. a) Load-unload stress-strain curves for a single nanowire cycled to increasingly high stresses until it fractured. We were unable to measure any appreciable plastic deformation. b) Young's modulus for eleven GST nanowires measured using the various methods. The average modulus over all measurements was $44 \pm 5 \text{ GPa}$, with no systematic dependence on size. Modulus data for annealed GST thin films from Won *et al.*¹⁰⁸ and Park *et al.*¹⁰⁹ are included for comparison. c) Strengths of the seven GST nanowires we were able to controllably bring to fracture. The average over all measurements was $1.2 \pm 0.3 \text{ GPa}$.

This is the first report on the mechanical behavior of GST nanowires, but we can compare our results with measurements on thin films. Kalb *et al.* measured the biaxial modulus of crystalline GST films using wafer curvature to be 45.2 ± 8.2 GPa;¹¹⁰ assuming Poisson’s ratio of 0.3, we would expect Young’s modulus 31.6 ± 5.7 GPa. Park *et al.* measured the biaxial modulus of 300 nm thick crystalline GST using nanoindentation to be 36.8 ± 1.54 GPa,¹⁰⁹ which would give Young’s modulus 25.8 ± 1.1 GPa. Won *et al.* examined the dependence of GST thin film modulus on size and annealing temperature using micromechanical resonators.¹⁰⁸ Modulus increased for film thicknesses below ~ 40 nm due to grain size effects, and increasing the annealing temperature increased the stiffness. For a 170 nm thick film (the only film they measured with thickness close to that of our nanowires), modulus increased from 7 GPa for the as-deposited amorphous phase to 35 GPa after annealing at 400°C for 10 minutes. These results are plotted along with ours in Figure 2.6b. Annealing resulted in growth of crystals in the *fcc* phase (150°C), mixed *fcc* and *hcp* phases (300°C), and the *hcp* phase (400°C), with grain size increasing with annealing temperature. This may help explain why the moduli extracted by other groups were lower than our nanowires—our nanowires were single crystals with *hcp* crystal structure, whereas the thin films were polycrystals. Kalb *et al.* and Park *et al.* did not report their crystal structures, but by comparing their annealing temperatures with those of Won *et al.* we may conclude that their films were of the lower stiffness *fcc* phase. The differences between the thin film measurements and ours may also be a result of orientation: whereas our measurements

probe a single crystal orientation, measurements on thin films would yield an average over all orientations. These results have important implications for the use of GST nanowires in mechanically robust phase change memory devices, since these materials undergo significant changes in volume when switching between amorphous and crystalline phases,^{111–115} resulting in large stresses in encapsulated systems. Control and understanding of mechanical behavior is also critical for integration of these materials onto flexible substrates,¹¹⁶ where strains may be high.

2.3.3. *GeTe Nanowires*

The utility of the direct strain measurement is perhaps best illustrated by its application to another phase change material, GeTe nanowires. Stress-strain curves for two pristine GeTe nanowires are shown in Figures 2.7a and c. Both curves are initially linear, abruptly flatten for several percent of strain, then stress continues rising linearly until fracture. This behavior is typical of materials which undergo a stress-induced transformation from one crystal structure to another, with phase boundaries propagating along the tensile axis (“Lüders-like” deformation).²⁵ We confirmed that similar behavior occurs in GeTe by examining the relative displacements of each marker placed on the nanowire; local changes in the displacement vs. position plots seen in Figures 2.7b and d provide information about the heterogeneity of the deformation. In the plots obtained in the midst of the plateau regime, two slopes may be observed: a high slope—indicating high strain—on the left side of the plot and a low slope on the

right. The boundary between the high and low slope regimes propagates left-to-right as deformation proceeds, corresponding to a propagating phase boundary between the initial and final crystal structure. Far-field strain measurements would not have been sensitive to this behavior, highlighting the value of the direct strain measurement.

We note that the phase boundary did not progress smoothly but rather in local strain bursts accompanied by the load drops noted in Figures 2.7a and c. Such behavior may be a consequence of the design of the tensile testing stage, which allows for neither displacement nor force control; any sudden burst in strain will necessarily result in a sudden drop in force as the load cell is allowed to relax back toward its equilibrium position. When the load abruptly decreases below the threshold for phase change, the propagation of the boundary halts until the actuator has pulled the wire to where the threshold has been reached again. This problem could be avoided by using a load cell with stiffness much higher than the specimen or with load- or displacement-controlled testing.

Although these experiments suggest that GeTe nanowires undergo a stress-induced phase change, they give no information on the second phase. To our knowledge, the only stable or metastable room temperature phases of GeTe are the crystalline face centered rhombohedral phase ($\alpha = 88.35^\circ$) and the amorphous phase.¹¹⁷ GeTe is known to form twins,^{118, 119} but we observe no measurable tilting of the nanowire after fracture which would accompany a change in orientation. *In situ* TEM testing, selected area electron diffraction (SAED), or electron backscatter diffraction (EBSD)

will be needed to understand whether the phase transformation is to a different, previously unpredicted crystal structure, an amorphous structure, or due to twinning. These measurements, as with the GST nanowires, represent the first reports on the mechanical behavior of GeTe nanowires and thus have important implications for use of these materials in phase change memory devices.

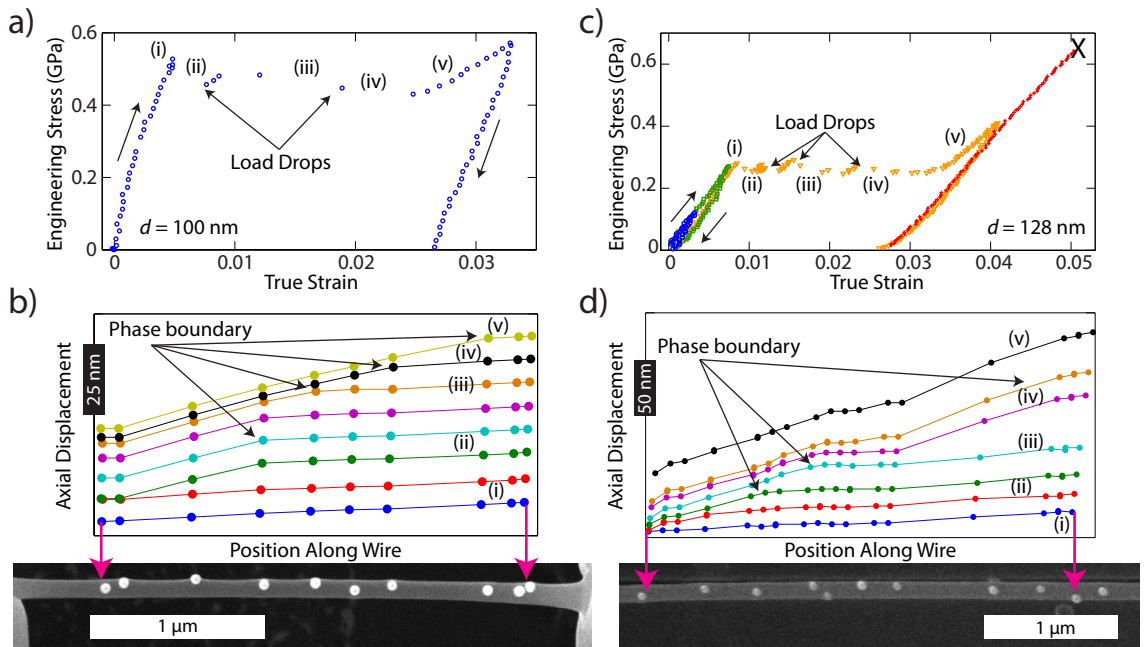


Figure 2.7: Mechanical testing of GeTe nanowires. a) Load-unload stress-strain curve for a 100 nm diameter nanowire with gauge length $3.2 \mu\text{m}$. b) Displacement vs. position data for the 100 nm wire. Each set of data represents a separate image from which strain was determined, correlating to the indicated points on the stress-strain curve. The phase boundary is clearly seen propagating from left to right. c) Load-unload stress-strain curves for a 128 nm diameter nanowire with gauge length $7.1 \mu\text{m}$. Each subsequent test was to a higher maximum stress. d) Displacement vs. position data for the 128 nm wire, in which the phase boundary can again be seen propagating from left to right. Not all points on this nanowire were used due to difficulty tracking all points on a longer gauge section.

2.4. Conclusions

We have demonstrated a method for performing quantitative tensile tests on individual nanowires. Wires were harvested and transferred to a MEMS-based tensile testing device using a nanomanipulator and clamped using EBID. Actuation of the device was achieved by applying a voltage across a thermal actuator, and load was provided by an integrated compound flexure in series with the nanowire. All displacements were determined by performing DIC on the image series obtained during testing, whether under an optical microscope or inside a SEM. We obtained direct, local measurements of strain by tracking the displacement of markers placed on the nanowires and effective measurements of strain by measuring the relative displacement of the two grips. Differences between these two measurements allowed us to extract average contact stiffnesses.

We showed that the EBID clamps commonly used for nanoscale tensile testing have stiffnesses that are approximately on the order of the stiffness of inorganic nanowire specimens commonly tested. As a consequence, inconsistent and significant errors—as high as 49% and as low as 1%—were introduced in measurements of displacement and hence strain and Young’s modulus, with a strong dependence on the stiffness of the sample and the geometry of the clamp. Furthermore, permanent clamp deformation resulted in nominal stress-strain curves that incorrectly indicated plastic deformation in the nanowires. We have demonstrated that a local measurement of strain is a necessity for mechanical testing when EBID clamps are used. Our work may

explain anomalous behaviors and discrepancies between nanowire moduli measured using grip displacement and provides guidelines for the nanowire and clamp stiffnesses needed to achieve acceptable errors in measurements of strain. For experiments which seek to measure coupled properties as functions of strain, such as those which will be discussed in later chapters, properties should be reported as functions of stress, the measurement of which is not affected by contact compliance.

We measured room temperature stress-strain behavior of Si, GST, and GeTe nanowires and found the first two of these to be elastic or nearly elastic up to fracture, with Young's moduli for nanowires with diameters >70 nm consistent with bulk. By contrast, GeTe nanowires exhibited Lüders-like deformation, indicative of a stress-induced phase change. The GeTe measurements highlighted the utility of the local strain measurement as it allowed for tracking of the propagating phase boundary. Further testing is needed to fully understand the change in phase. This is the first report on the mechanical behavior of GST and GeTe nanowires, with important implications for the use of these nanowires as phase change memory materials.

Chapter 3

Raman-Based Method for Measuring Thermal Conductivity in Strained Nanowires

Portions of this chapter have been reproduced with permission from Nano Letters, Volume 14, Issue 7, Pages 3785-3792. Copyright 2014 American Chemical Society.

The relative dearth of experimental measurements of strain-mediated thermal conductivity is largely due to the complexity of simultaneously applying and measuring stress or strain, heating, and measuring temperature. One versatile, non-contact method of measuring thermal conductivity is Raman thermography, which uses a laser to heat a suspended specimen and the spectrum of inelastically scattered light to measure temperature, requiring no fabrication of sample heaters or thermometers. Raman additionally provides information on phonon frequencies and densities of states, making it particularly well-suited to studying phonon transport. The method was first demonstrated for porous Si^{120, 121} and later extended to suspended, bridged graphene,¹²²⁻¹²⁸ carbon nanotubes,^{129, 130} MoS₂,¹³¹ GaAs nanowires,¹³² Si membranes,¹³³ and cantilevered Si nanowires.³¹ However, the difficulty of decoupling the effects of strain from temperature on the frequencies of the Raman-active modes has largely prevented this method from being used on strained samples. In this

chapter, we will describe a means of extending Raman thermography to strained samples—Raman *piezothermography*—as well as several improvements to the method, including proper determination of contact resistance, heat lost to air, and absorbed laser power.

3.1. Mathematical Model

We begin by deriving an analytical expression for the temperature rise at an internal heat source (the laser spot) for a suspended nanowire. The total thermal resistance of the system may be written in terms of the Raman shift ω and absorbed laser power P as^{123, 134}

$$R_{system} = \frac{\partial T}{\partial P} = \frac{1}{\chi_T} \frac{\partial \omega}{\partial P}, \quad (3.1)$$

where χ_T is the relationship between first-order Raman shift and temperature ($\chi_T = \partial\omega/\partial T = 0.022 \text{ cm}^{-1}$ for Si nanowires⁸¹). Equation 3.1 yields the total thermal resistance of the system, including the effects of contact resistance and air conduction. In order to distinguish these effects from the thermal conductivity of the sample, we make use of the fact that the temperature rise in a suspended nanostructure will be a function of the thermal resistances of all components of the thermal system. We therefore scan a point source—a laser—along a doubly-clamped specimen such that the shape of the resulting heating profile, as measured at the source, is a signature of the thermal resistances of the components of the system.

The steady-state heat equation for the temperature rise $\Delta T = T - T_{ambient}$ at position s in a one-dimensional conductor of length L , cross-sectional area A , circumference C , heated from some point in the interior a distance a and $L - a$ from the two heat sinks (see Figure 3.1) may be written as^{135, 136}

$$\kappa \frac{d^2 \Delta T}{ds^2} - \frac{Ch}{A} \Delta T + \frac{P}{\sqrt{\pi} w A} \exp\left(-\frac{s^2}{w^2}\right) = 0 \quad (3.2)$$

with boundary conditions

$$\begin{aligned} \Delta T(-a) &= R_{c,l} A \kappa \left. \frac{d\Delta T}{ds} \right|_{s=-a} \\ \Delta T(L-a) &= -R_{c,r} A \kappa \left. \frac{d\Delta T}{ds} \right|_{s=L-a} \end{aligned}$$

where h is the heat transfer coefficient between the nanowire and air, κ is the thermal conductivity, P is the absorbed power, w is the half-width of the laser spot, and $R_{c,l}$ and $R_{c,r}$ are the thermal contact resistances at the left and right heat sinks, respectively. The laser power source is represented by a Gaussian centered at $s = 0$. The solution gives the full temperature distribution in the nanowire, but we are only interested in the temperature rise at the laser spot as the distance a is varied. Setting $x = 0$ and taking the limit as w approaches 0 (a reasonable simplification since, at 285 nm, the real w is approximately 2% the length of the nanowire) we obtain the temperature rise ΔT at the power source, where now the independent variable x is

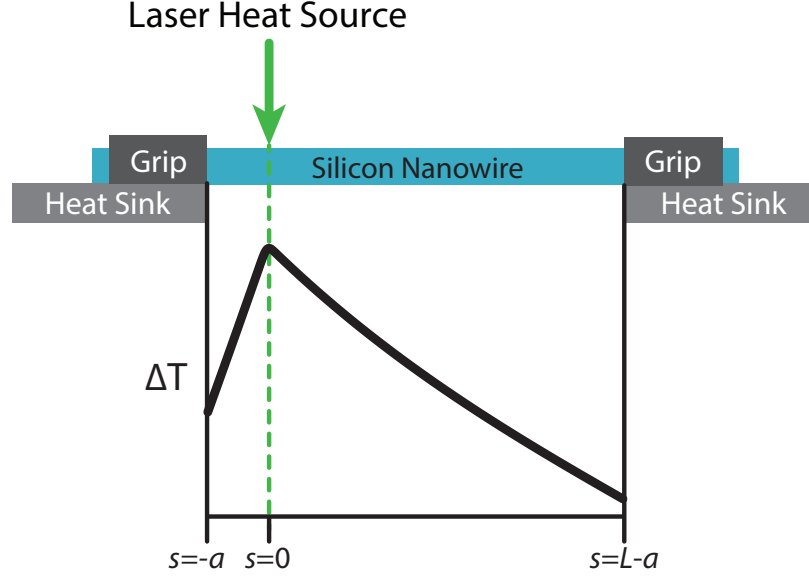


Figure 3.1: Schematic of setup for determination of the heating profile as a function of laser position. The solution to the heat equation yields temperature profiles similar to the representative profile shown. This function is solved for $s = 0$ to obtain the rise in temperature at the laser spot. By varying a we obtain the temperature rise at the laser spot as the laser is scanned across the nanowire.

the distance from the laser to the left heat sink:

$$\Delta T(x) = P \frac{[MR_{c,r} \cosh(m(L-x)) + \sinh(m(L-x))] [MR_{c,l} \cosh(mx) + \sinh(mx)]}{M [M(R_{c,l} + R_{c,r}) \cosh(mL) + (1 + M^2 R_{c,l} R_{c,r}) \sinh(mL)]} \quad (3.3)$$

where $M \equiv \sqrt{Chak}$ and $m \equiv \sqrt{Ch/A\kappa}$. Fitting the heating profile $\Delta T(x)$ along the wire gives thermal conductivity as well as the thermal contact resistances, provided accurate determination of P and h . In the case of Raman thermography, which employs the excitation laser as the heat source, $P = IQ_a$ where I is the total applied laser power and Q_a is the size-, refractive index-, polarization- and wavelength-dependent absorption efficiency.¹³⁷

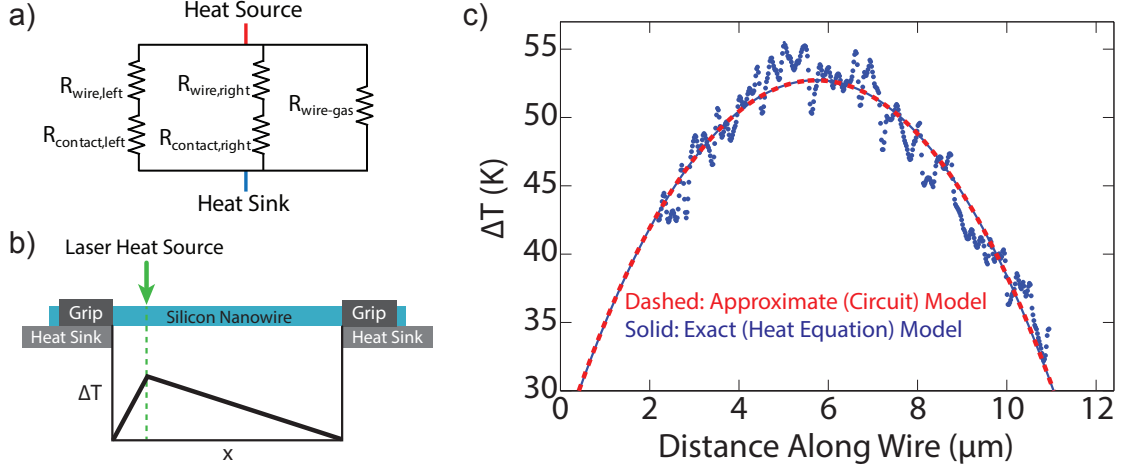


Figure 3.2: Thermal circuit model. a) Schematic of thermal resistor model. The nanowire-contact series on either side of the laser are in parallel with each other as well as the nanowire-gas interface. b) Approximate instantaneous temperature profile in the nanowire used to calculate the thermal resistance of the nanowire-gas interface leg of the circuit. c) A heating profile for wire 1 fit to the exact model (Equation 3.3) and the approximate model (Equation 3.4). The fits are nearly identical and yield thermal conductivities within $1 \text{ W m}^{-1} \text{ K}^{-1}$ of each other.

An alternative, more mathematically simple model which, as we will see, provides a good approximation to Equation 3.3 is based on thermal circuits. For solid conduction only, heat generated by the laser may travel in one of two directions: left or right in the geometry of Figure 3.1. We may therefore model this system as two thermal resistors in parallel, each including the resistance of some portion of nanowire length as well as the thermal resistance of the contact. For heat lost to air, we treat the air as another thermal resistor in parallel with the two legs of the nanowire. This may be seen schematically in Figure 3.2a. Since the heat loss to air from any point along the nanowire depends on the temperature at that point, the total loss depends on the full temperature profile in the nanowire for any given laser position s . We approximate

this profile by solving the heat equation with no losses to air ($h = 0$), no contact resistance ($R_{c,l} = R_{c,r} = 0$), and an infinitely narrow Gaussian heat source ($w = 0$). The solution gives the profile shown in Figure 3.2b, which is linear between the laser spot and each heat sink. By integrating the triangular profile we arrive at a simple expression for the temperature rise as a function of laser position:

$$\Delta T(x) = R_{system}P = \left(\frac{1}{\frac{x}{A\kappa} + R_{c,l}} + \frac{1}{\frac{L-x}{A\kappa} + R_{c,r}} + \frac{hCL}{2} \right)^{-1} P \quad (3.4)$$

Fitting heating profiles to Equation 3.4 yields curves and thermal conductivities in excellent agreement with Equation 3.3, as can be seen in Figure 3.2c.

In order to accurately determine thermal conductivity and contact resistance of a strained nanowire using the models described here, a number of steps must be performed:

1. Obtain spatially resolved maps of Raman spectra.
2. Decouple strain and temperature effects on the Raman shift.
3. Determine nanowire cross-sectional area and circumference, A and C .
4. Determine power absorption based on nanowire shape, Q_a .
5. Determine size-dependent heat losses to air, h .

These steps are described in detail in the following sections.

3.2. Materials and Methods

3.2.1. *Si Nanowires*

We used the $\langle 111 \rangle$ -oriented VLS Si nanowires purchased Sigma Aldrich which we described in Chapter 2 to determine thermal conductivity as a function of stress. These nanowires were chosen due to their long length (15-20 μm), lack of any measurable taper, and strong Raman signal indicating a low defect concentration. The monodispersity of these wires was also advantageous for checking repeatability of our measurements. We considered several other Si nanowires which proved inappropriate for these measurements. We were unable to grow the top-down nanowires described in Section 2.1 long enough for adequate Raman mapping, and the growth method furthermore raised concerns about atomic-scale defects and pores,^{36, 37} which would not be easily measured but would affect thermal transport. We attempted measurements on uniaxially strained nanobridges fabricated at Paul Scherrer Institut by patterning and underetching of biaxially strained silicon-on-insulator wafers,¹³⁸ but the elastic strains in these samples relaxed under the Raman laser, perhaps due to size effects on the brittle to ductile transition temperature in Si,^{8, 139} making the decoupling procedure described below in Section 3.2.3 impossible. We examined other VLS-grown Si nanowires purchased from CVD Equipment Corporation in a transmission electron microscope (TEM) and found them to be of poor crystal quality. These wires may, in the future, be useful for studies of dislocation effects.

3.2.2. Raman Mapping of Nanowires

In order to determine thermal conductivity, heating profiles as a function of strain and laser power must first be determined. To prepare samples for testing, nanowires were dispersed on holey carbon grids, harvested, and transferred to the grips of a tensile testing device described in Chapter 2 using a nanomanipulator (see Section 2.1). The device may be seen in Figure 3.3a. Wires were clamped using electron beam induced deposition (EBID), being careful to minimize deposition on the wire itself. A representative scanning electron microscopy (SEM) image of an individual nanowire clamped to the device is given in Figure 3.3b.

Maps of spectra (Figure 3.3c) were obtained for nanowires subject to a uniform strain as well as for nanowires damaged via ion bombardment by placing the device under the objective of a confocal micro-Raman system equipped with a 532 nm continuous-wave laser at ambient temperature and pressure (see Figure 3.3d). For the unstrained state and upon application of each increment of strain, spectra were collected along the central 8-10 μm of the nanowire length and across the nanowire diameter with a 100 nm step size. Laser intensity was precisely controlled with a neutral density filter, and at least five different powers in the range of 40 to 400 μW (as measured using a power meter at the focal point) were used. Both strain and laser power increments were varied non-monotonically to rule out systemic measurement errors and strain relaxation. Sample first-order spectra collected with low and high laser powers, with and without applied uniform strain are given in Figure 3.3e. These

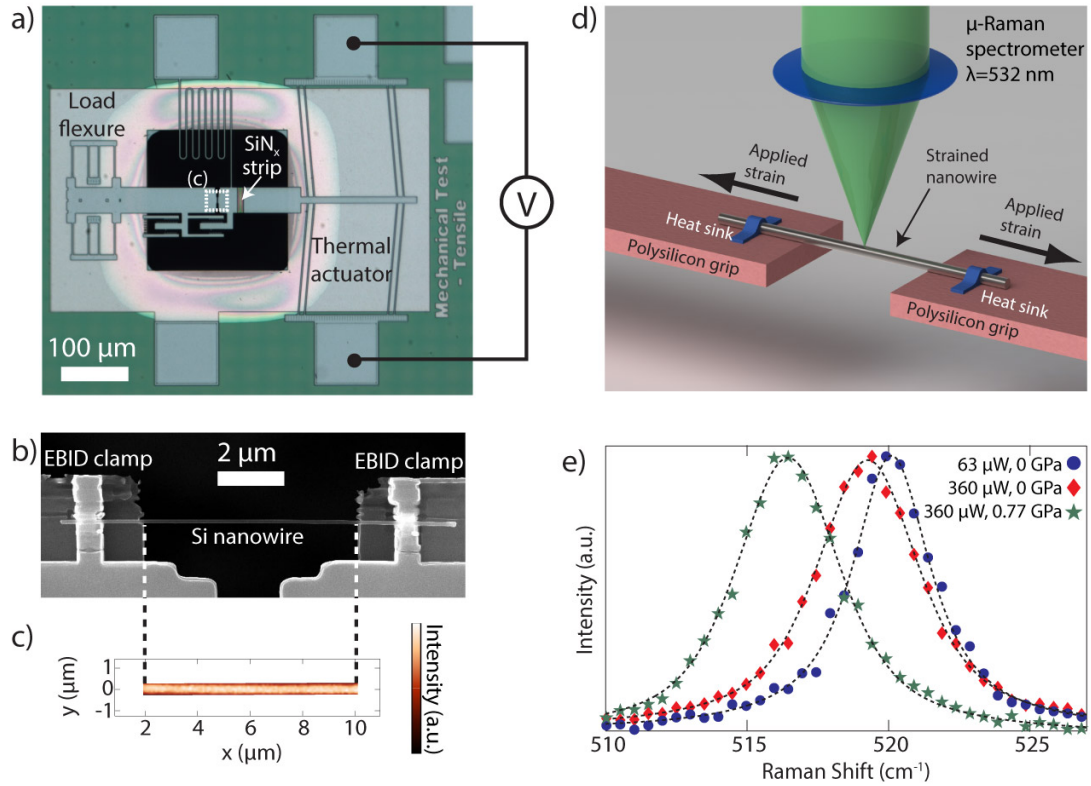


Figure 3.3: Experimental setup for Raman piezothermography. a) Optical image of the MEMS tensile testing device described in Chapter 2. b) Schematic of experimental setup. c) SEM image of a $\langle 111 \rangle$ Si nanowire clamped to the MEMS device. d) A to-scale map of Raman peak intensities. e) Sample spectra collected at low ($63 \mu\text{W}$) and high ($360 \mu\text{W}$) applied laser powers (equivalently, low and high temperature) and at zero and 0.77 GPa of stress. Dotted lines are fits to Gaussian + Lorentzian lineshape.

peaks correspond to the strain- and temperature-dependent zone-center longitudinal optical (LO) phonon in Si. Each spectrum was fit to a Gaussian + Lorentzian lineshape to extract peak intensities, linewidths, and frequencies, and maps of these fits were interpolated using cubic splines. A full procedure for operation of the Raman system at Penn may be found in the Appendix.

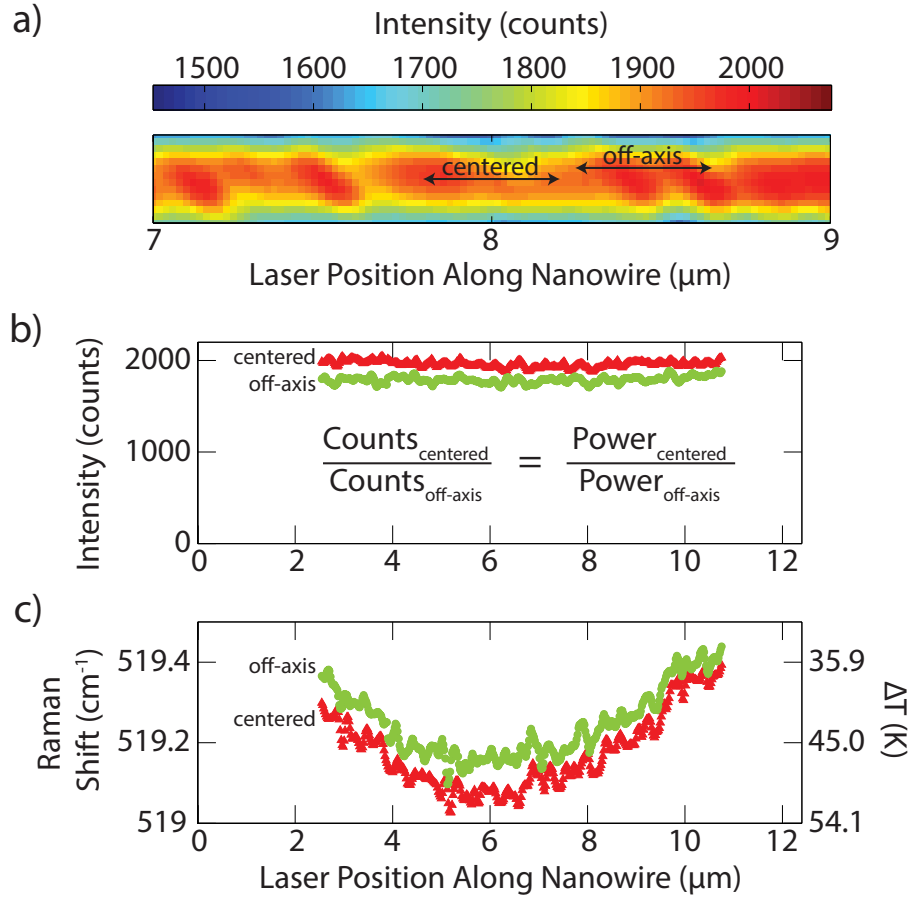


Figure 3.4: Scheme for determining power absorbed when the laser is not centered on the nanowire. a) 2 μm section of an interpolated Raman peak intensity map for unstrained wire 1. The laser was assumed to be centered on the nanowire where there were maxima in peak intensity. b) First-order Raman peak intensity for the center and laterally shifted from the nanowire axis. The absorbed power for the original data was calculated using the FDTD method described in the Section 3.2.5. The absorbed power for the off-axis data was calculated from the ratio of the peak intensities (about 0.91 for the data shown here) and the absorbed power for the original data. c) Corresponding Raman shift profiles for the original and off-axis data. The temperature difference is approximately 4 K.

The spatially resolved maps of Raman spectra allow us to establish which spectra were obtained when the laser was centered on the nanowire by examination of the Raman peak intensity: the highest intensity spectra were acquired using the highest laser power (equivalently, when the laser was centered). We gain additional information by examining spectra collected when the laser was off the nanowire axis, but the incident laser power must then be determined. To find the incident laser power for off-axis spectra, we calculated the ratio between the average peak intensity when the laser was centered and the average when the laser was off-axis. We then assumed this ratio to be the same as the relative incident laser powers (see Figure 3.4). These profiles of Raman shift with a given laser intensity, as seen in Figure 3.5a, were then used to find the temperature rise as a function of laser position using the method described in the following section. The inclusion of off-axis profiles had a negligible effect on the fit to the plot of Raman shift as a function of laser power (Equation 3.1) but resulted in more heating profiles to fit to Equation 3.3.

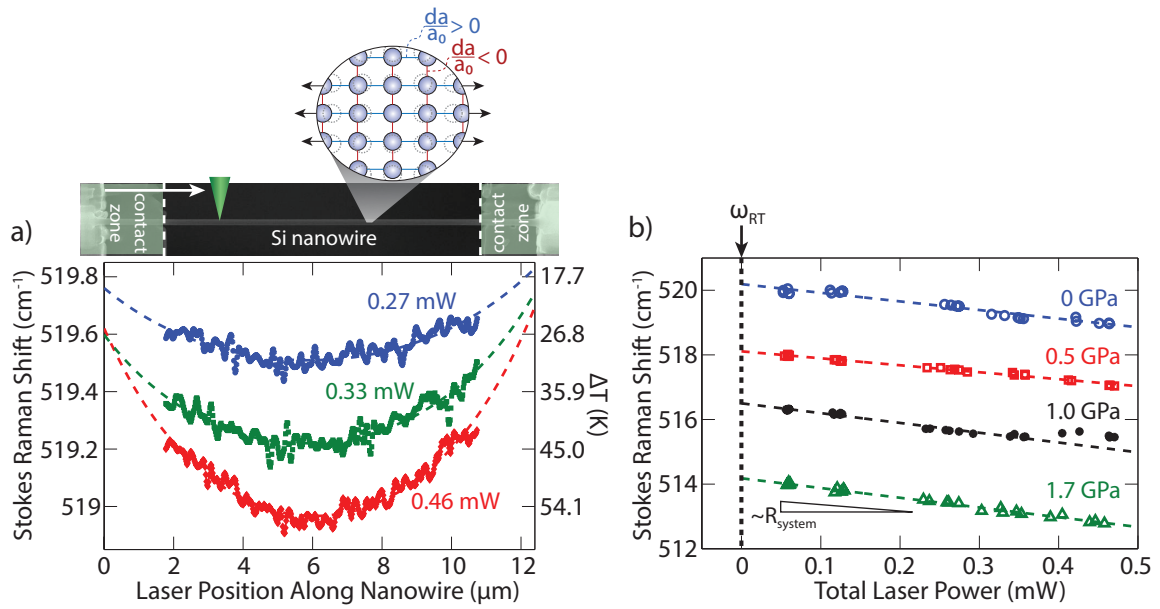


Figure 3.5: Raman shifts in Si nanowires. a) Raman shift as a function of laser position along the nanowire. Spatially resolved spectra were collected with a 100 nm step, and the maps of peak intensity and position were interpolated with 20 nm spacing. As laser power increases, temperature increases, resulting in an overall downshift of the curves. The concave shape is due to the thermal resistance of the wire, heat losses to air, and the contacts with the heat sinks on either end. Residuals of the fits are shown in Figure 4.4. b) The minima of the fits shown in (a) for each laser intensity for several increments of stress. The slope of this curve is the total thermal resistance of the system, and the zero-intercept of the fit is taken to be the room temperature peak position. Determination of the room temperature peak position allows us to plot temperature as a function of peak position (secondary axis of (a)) for any strain.

We note that exposure of the EBID clamp material to the laser will heat and degrade the clamps, leading to their mechanical failure. Laser exposure can also induce diffusion of the clamp material down the nanowire. An example of a heating profile obtained from a nanowire where the EBID material had diffused may be seen in Figure 3.6; the diffused material absorbs more laser power, resulting in anomalous heating near the grips. This is contrary to our expectation of lower temperature rises near the heat sinks and is difficult to account for. Profiles such as the one shown could not be used for thermal conductivity measurements, necessitating the use of longer nanowires ($\gtrsim 10 \mu\text{m}$) so that the diffused EBID material could be avoided. In order to further minimize exposure of the EBID material to the laser, steps were milled in the grips so that the wire could be clamped away from the edge of the grip (see Figure 3.3b and the Appendix).

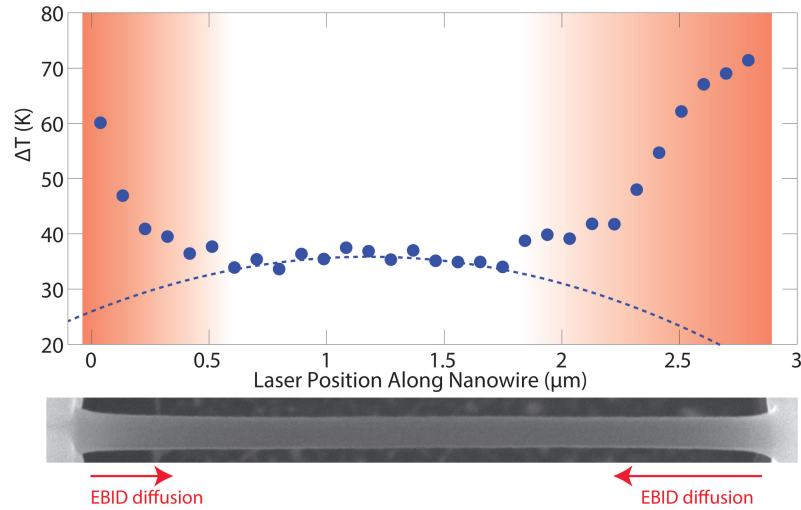


Figure 3.6: Temperature rise from laser heating of diffused EBID material, with attempted fit to Equation 3.3. Consequently, heating profiles from short nanowires such as the one shown here were not used for measurement of thermal conductivity.

3.2.3. Decoupling Strain and Temperature

Increasing strain or temperature produces downshifts in the Raman peak position, and the separate contributions may be decoupled by varying the laser intensity as follows. Fits of the Raman shift minima (i.e. highest temperatures) of the Raman shift profile as a function of the total incident laser intensity for an unstrained nanowire as well as at three applied stresses are shown in Figure 3.5b, with the slope of these fits proportional to the total thermal resistance of the system as per Equation 3.1. The zero-intensity intercepts of the fits shown in Figure 3.5b were taken to be the room temperature peak positions for each stress increment. The differences between the unstrained and strained room temperature peak positions are due to strain only, while the difference between the room temperature peak at a given stress and the measured peaks is entirely due to laser heating. With our independent measure of stress, this decoupling procedure enabled the measurement the room temperature relation between Raman shift and tensile stress in Si (see Section 4.1.3). The peak shift for a given stress was observed to be linear with laser intensity, suggesting a constant thermal resistance over the temperature range of the measurement ($\Delta T < 80$ K) and negligible resistive heating due to photocurrents, which would heat the wire as ΔP^2 . The temperature (secondary axis of Figure 3.5a) was subsequently calculated from the spectrum as $\Delta T = (\omega - \omega_{RT})/\chi_T$, where ω is the measured peak position and ω_{RT} is the room temperature peak position.

We confirmed that the Raman shift with temperature, χ_T , is independent of strain

by performing lattice dynamics simulations to extract the temperature dependence of the frequency of the zone-center optical phonon (corresponding to the first order Raman peak) at various tensile stresses. Figure 3.7a shows the calculated zone-center optical phonon frequencies at various increments of stress and temperature containing the range of stresses and temperatures used in our experiments. The slope of each fit shown in Figure 3.7a corresponds to χ_T . Thus, if the slope depends on stress, then so does χ_T . Figure 3.7b shows the slopes plotted against applied stress, where the error bars are the 95% confidence intervals on the fit. It is worth noting that although the exact numbers extracted from these calculations do not precisely match experimental values, we are only concerned with any stress-dependent trends in χ_T since the unstrained experimental value is well known. The results of these calculations exhibit no trend, so we treat χ_T as unchanging with stress. It is furthermore worth noting that χ_T originates from thermal expansion of the crystal lattice and is therefore intrinsically tied to lattice anharmonicity. Differences in anharmonic behavior at the nanoscale relative to macroscopic behavior would manifest as changes to the elastic behavior at large strains,⁸⁹ yet our measurements show both linear elastic response and Young's moduli that agree with bulk values for $\langle 111 \rangle$ Si (see Chapter 2). Thus, our simulations and experiments suggest the value of χ_T for a strained Si nanowire with $d > 165$ nm to be the same as that of bulk Si, which is the same as that of unstrained nanowires.⁸¹

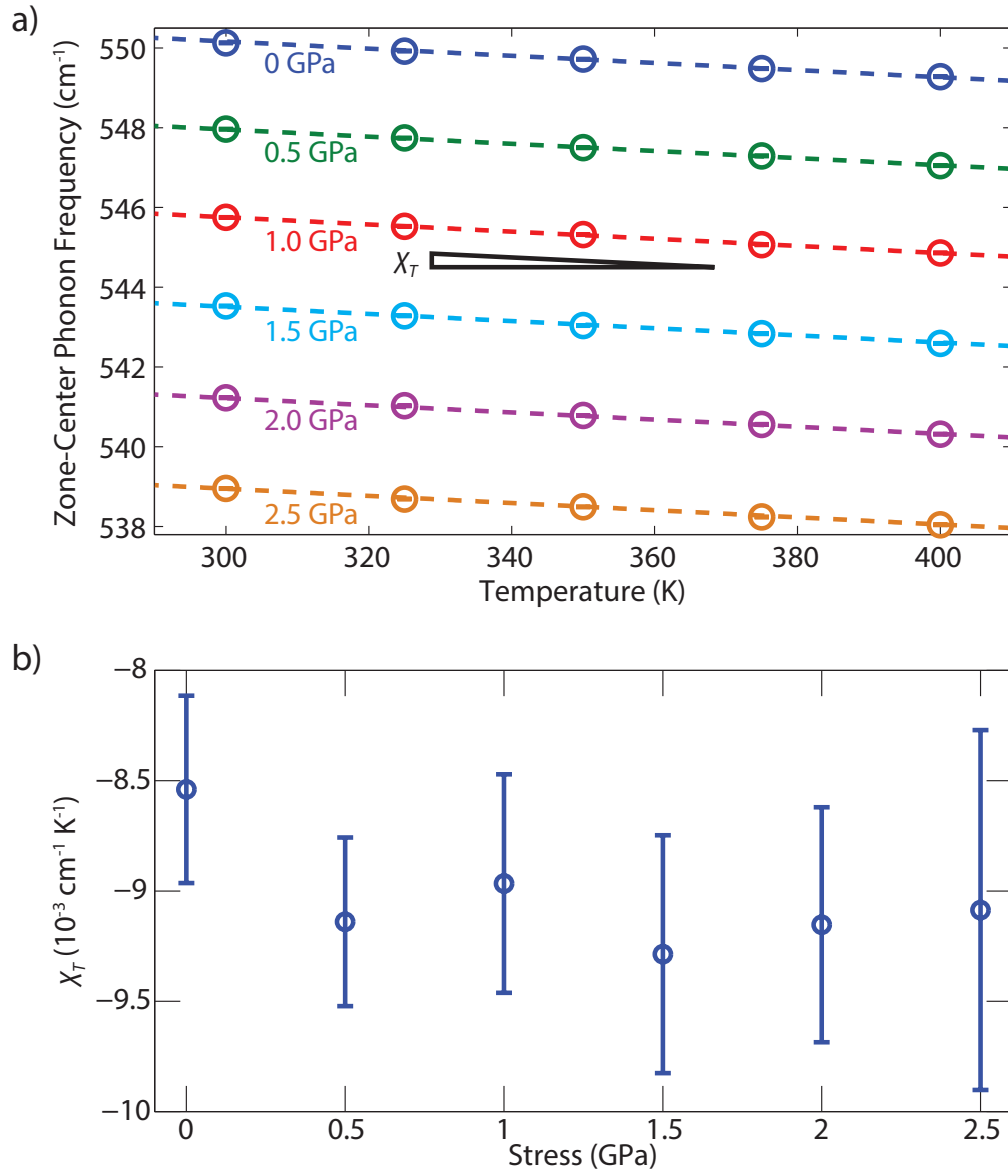


Figure 3.7: MD simulations performed by Mehdi Zanjani and Prof. Jennifer Lukes at Penn to find χ_T dependence on stress. a) Calculated zone center longitudinal optical phonon frequency at various temperatures and stresses, corresponding to Raman shift for the first-order Si peak near 521 cm⁻¹. The slope of the fit shown is the relationship between Raman shift and temperature for a given stress ($\chi_T(\sigma)$). b) $\chi_T(\sigma)$ for $\sigma = 0$ to 2.5 GPa. The error bars are the 95% confidence intervals on the slope of the fits to the data shown in (a).

3.2.4. Correction for Actuator Heating

When straining nanowires using the MEMS device there is slight heating of one grip from the thermal actuator, yielding a temperature difference between the grips of no more than 40 K. To correct for this, a scan was made at power low enough to yield laser-induced heating below the noise floor of our temperature measurement (about 4 K). The slope of this curve, an example of which is shown in Figure 3.8a, was taken to be the gradient due to temperature and removed from the strained plots. An example of an uncorrected strained plot and the same data corrected for the temperature gradient and fitted to Equation 3.3 is shown in Figure 3.8b.

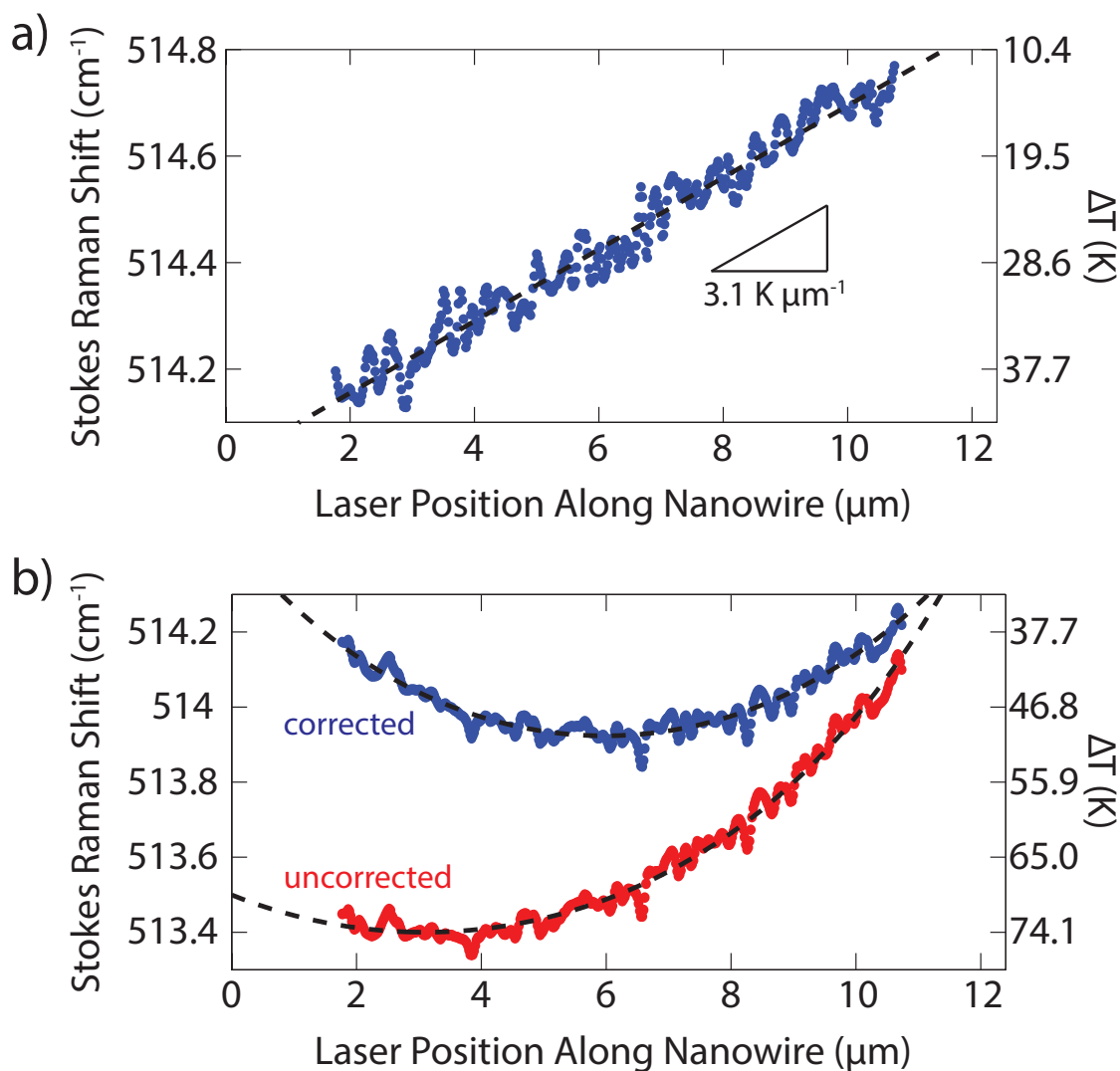


Figure 3.8: Correction for actuator heating. a) Peak position and temperature profile at 1.7 GPa obtained using applied laser power $61 \mu\text{W}$, low enough that the laser-induced heating was below the resolution of our measurement. The slope of the linear fit corresponds to a temperature gradient across the wire of $3.1 \text{ K } \mu\text{m}^{-1}$ and was taken to be entirely due to heating from the actuator. b) Peak position and temperature profiles with the corresponding fits at 1.7 GPa obtained using applied laser power 0.22 mW , uncorrected and corrected for the slope shown in (a).

3.2.5. Calculation of Nanowire Cross-Section and Absorption Efficiency

The exact geometry of the nanowire—cross-sectional area, circumference, and shape—affects the calculation of thermal conductivity from the measured thermal resistance and strongly affects the fraction of incident laser power absorbed by the nanowire. In order to determine these quantities, each nanowire was cut following testing using a focused ion beam (FIB) to create a cantilever. The cut nanowires were then bent upward using a nanomanipulator inside a SEM in order to directly image the cut face and obtain the cross-sectional shape and hence circumference and area. Absorption for Si nanowires with a circular cross-section is known from analytical Mie scattering solutions,¹⁴⁰ but our nanowires exhibited significant deviations from circularity, preventing application of an analytical solution. Using a commercial finite-difference time-domain (FDTD) software package (Lumerical), 3D numerical simulations were performed for the Si nanowires with a Gaussian source focused to a FWHM of 570 nm to match measured experimental conditions. Non-circular cross-sections were obtained by fitting polynomials to cross-sectional nanowire images obtained via SEM (Figure 3.9a-b), and power absorbed per unit volume in the simulated structures was calculated from the divergence of the Poynting vector $P_{abs} = -0.5\omega|E|^2\text{imag}(\epsilon)$ where ω is frequency, $|E|^2$ is electric field intensity, and ϵ is the permittivity. Integrating $|E|^2$ over the entire illuminated nanowire volume (Figure 3.9c) produced total power absorbed. The refractive index of Si was taken from Ref. 141. A range of frequencies about 563.5 THz with a bandwidth of 30 THz were applied to

each wire to simulate the effects of scaling nanowire cross-sectional area and ensure measurement errors would not result in incorrect absorption values. No resonance peaks were found, and calculated absorption values were stable to $\sim 0.2\%$ within the frequency range tested. Values for wires 1-4 varied between 4.9% and 6.1%. By contrast, absorption in cylinders of the same major diameters (171-177 nm) calculated using the Mie solutions and accounting for the relative sizes of the laser spot and the nanowire is 3.1-4.4%.

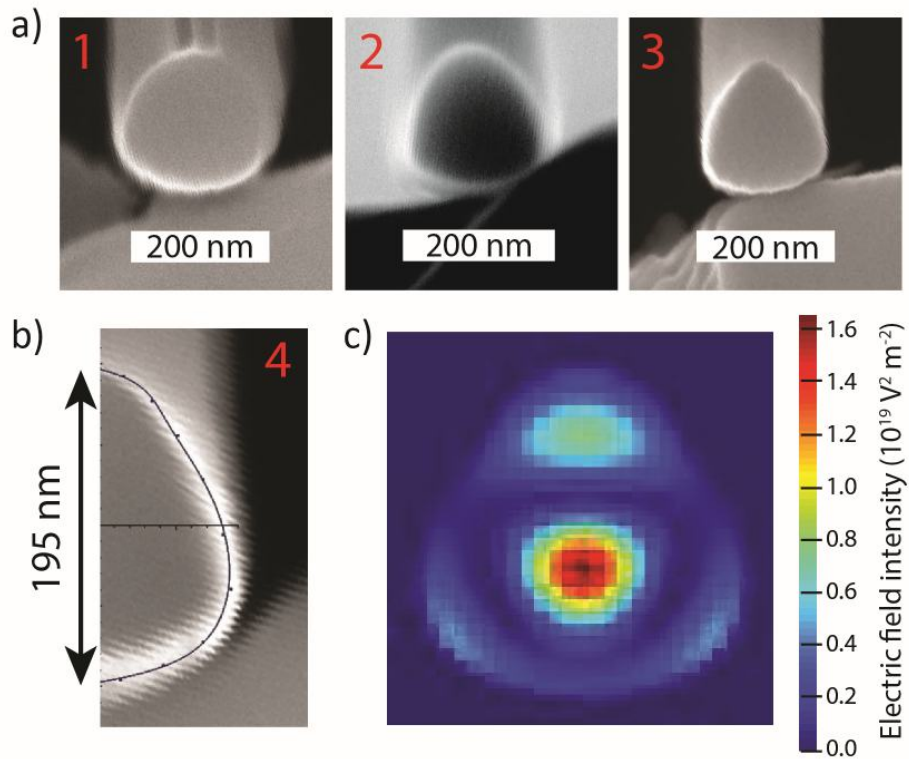


Figure 3.9: Cross-section-dependent power absorption of nanowires. a) Cross-sectional SEM images of Si wires 1-3. b) Fitted nanowire profile overlaid on cross-sectional SEM image of wire 4. c) Cross-section of simulated nanowire under far-field illumination, illustrating spatial distribution of electric field intensity for 532 nm wavelength light. FDTD calculations were performed by Dr. Brian Piccione at Penn.

3.2.6. Heat Losses Due to Air Conduction

Our experimental setup did not allow for measurements in vacuum, so heat losses to the surrounding air had to be considered. Experimental and theoretical evidence exists for a size dependence of the heat transfer coefficient to air, but no prior measurements on cylindrical samples of similar diameters to our nanowires have been performed. We therefore developed a means of measuring it using a variation of our Raman method. For fixed surroundings, thermal conductivity and the heat transfer coefficient to air should not depend on how the sample is clamped; that is, if the wire is in bridged or cantilevered geometry, κ and h should be the same. Keeping this in mind, the thermal measurement procedure for bridged nanowires was performed on wire 4, and after testing the wire was cut at one end using a FIB. The procedure was then repeated for the cantilevered geometry. We may modify the boundary conditions of Equation 3.2 to allow for air conduction from the free end of the wire:¹⁴²

$$\begin{aligned}\Delta T(-a) &= R_{c,l}A\kappa \left. \frac{d\Delta T}{ds} \right|_{s=-a} \\ \Delta T(L-a) &= -\frac{\kappa}{h} \left. \frac{d\Delta T}{ds} \right|_{s=L-a}\end{aligned}$$

so we can substitute κ/h for $R_{c,r}A\kappa$ in Equation 3.3:

$$\Delta T(x) = P \frac{[(M/Ah) \cosh(m(L-x)) + \sinh(m(L-x))] [MR_{c,l} \cosh(mx) + \sinh(mx)]}{M [M(R_{c,l} + 1/Ah) \cosh(mL) + (1 + M^2R_{c,l}/Ah) \sinh(mL)]}. \quad (3.5)$$

We fit both the bridged and cantilevered heating profiles (see Figure 3.10a) using various fixed values of the heat transfer coefficient and extracted thermal conductivity from the fit. The intersection of the h vs. κ curves seen in Figure 3.10b represents the value of h which yields the same calculated value of κ for both clamping geometries; this intersection occurred at $h=1.8 \text{ W cm}^{-2} \text{ K}^{-1}$ and $\kappa=52 \text{ W m}^{-1} \text{ K}^{-1}$ (thermal conductivity results are discussed fully in the next chapter). Figure 3.10c shows a heating profile fit to curves which do and do not account for heat loss to air; although both curves fit the profile well, not accounting for air losses (i.e., treating $h=0$) leads to a 19% increase in the calculated thermal conductivity, highlighting the importance of measuring and accounting for heat losses to air. The difference would be expected to be more pronounced for thinner nanowires, which have both higher h and lower κ .

Although the value of h we measure differs from other diameter-dependent experimental measurements of the heat transfer coefficient, from which we would predict h to be roughly $0.50 \text{ W cm}^{-2} \text{ K}^{-1}$,¹⁴³ it is in better agreement with the value we calculate using a semi-empirical model from Wang *et al.* based on measurements performed on microwires and carbon nanotubes.^{144, 145} This two-layer model appropriate for quasi-1D particles with diameter approaching the mean free path of air molecules treats the transition region near the particle surface using molecular kinetics and the region farther from the particle as a continuum. Within this model, the heat transfer coefficient is related to the mean free path and heat capacity of air as well as the

particle diameter via the dimensionless Nusselt number, Nu :

$$Nu = \frac{2rh}{\kappa_{air}} = \frac{4\alpha_f f_{ncr} \zeta / \pi}{\beta + f_{ncr} (\zeta + \Delta/\lambda) \ln(n_r ((\zeta + r_0/\lambda) / (\zeta + \Delta/\lambda)))} \quad (3.6)$$

where r is the particle radius, λ is the mean free path of air (67 nm, Ref. 146), Δ is the thickness of the transition region (here taken to be 5λ as per Ref. 147), $\zeta = r/\lambda$, and f_{ncr} is a function of ζ . The values of the fitting parameters α_f , β , n_r , and r_0 were taken from Ref. 144. We then solve this expression for h , obtaining $1.18 \text{ W cm}^{-2} \text{ K}^{-1}$ for a wire 175 nm in diameter. At $1.8 \text{ W cm}^{-2} \text{ K}^{-1}$, our experimental value of h is higher by 52%. We attribute the discrepancy to errors in the choice of Δ as 5λ , the maximum value allowed by Ref. 147, and in the fitting parameters taken from Ref. 144, which were determined using samples an order of magnitude larger and smaller in diameter than our nanowires. Heat transfer from solids to air is also strongly affected by environmental conditions such as humidity, air currents, and proximity to other surfaces, which for our measurements were not likely identical to those of other reports.

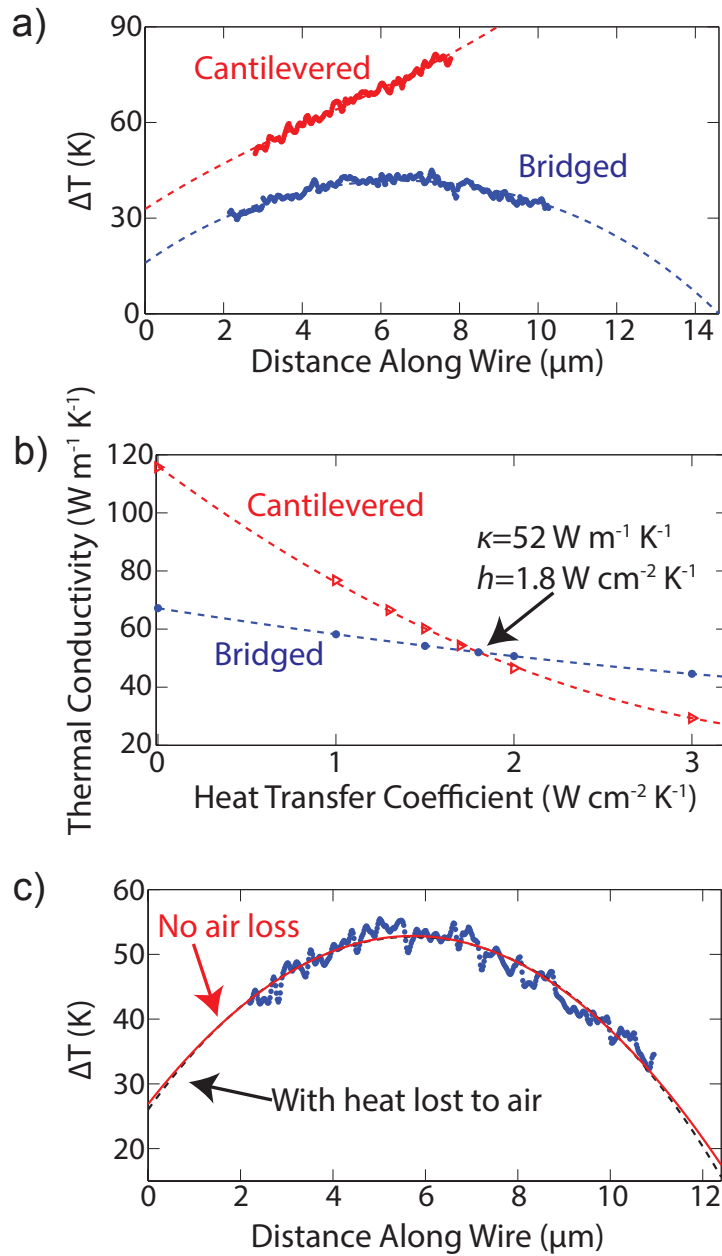


Figure 3.10: Nanowire heat transfer to air. a) Bridged and cantilevered heating profiles for the same wire obtained using the same laser intensity and fit using the correct value of h . b) Thermal conductivity calculated using varying values of the heat transfer coefficient for wire 4 in bridged and cantilevered geometry. The intersection of the two curves gives the correct values of the two variables: $52 \text{ W cm}^{-1} \text{K}^{-1}$ and $1.8 \text{ W cm}^{-2} \text{K}^{-1}$, respectively. c) Heating profile for wire 1 collected using $370 \mu\text{W}$ incident laser intensity and fit to models with and without heat lost to air. The fits are nearly identical in the region of the data. If air conduction is not accounted for, thermal conductivity measured from this profile increases by 19%.

3.3. Conclusions

We have extended and refined the Raman thermography method in order to measure thermal conductivity in strained nanowires. By scanning the laser along the wire we may measure and account for thermal contact resistance, a non-negligible quantity which in conventional thermal testing is treated as being insignificant. Our means of decoupling strain and laser heating effects on the Raman spectrum by varying laser power allows for determination of both, as well as for the application of Raman thermography to strained systems—Raman *piezothermography*. We have furthermore accurately calculated the absorbed power using FDTD simulations which take into account the nanowire’s cross-sectional size and shape. Finally, we developed a means of measuring the heat transfer coefficient to air in order to accurately perform testing at ambient pressure. In the next chapter we will discuss the results acquired by applying this novel method to homogeneously and heterogeneously strained Si nanowires and thin films.

Chapter 4

Raman Piezothermography of Strained Si Nanostructures

Portions of this chapter have been reproduced with permission from Nano Letters, Volume 14, Issue 7, Pages 3785-3792. Copyright 2014 American Chemical Society.

In the previous chapter we described a novel method of measuring thermal conductivity as a function of applied uniaxial strain in nanowires. In this chapter, we will discuss our results on unstrained, strained, and irradiated Si nanowires. We will then demonstrate an extension of the method of unstrained and strained Si thin films and micromeshes.

4.1. Si Nanowires

4.1.1. Unstrained Si Nanowires

We first compare our results for thermal conductivity of unstrained nanowires with other groups' reports on VLS-grown Si nanowires at room temperature. The mean thermal conductivity values we obtained for four unstrained $\langle 111 \rangle$ -oriented Si nanowires with diameters 171-177 nm were between 58 and 66 $\text{W m}^{-1} \text{K}^{-1}$, in agreement with these other reports, which we have plotted in Figure 4.1 along with

the predicted thermal conductivity based on diffuse boundary scattering:

$$\kappa_{NW} = \frac{d \kappa_{bulk}}{l_{bulk} + d} \quad (4.1)$$

where κ_{NW} and κ_{bulk} are the thermal conductivities of the nanowire and bulk Si, respectively; d is nanowire diameter; and l_{bulk} is the bulk mean free path.³¹ This model predicts thermal conductivity $55 \text{ W m}^{-1} \text{ K}^{-1}$ for a 175 nm nanowire, well within the error bars of our measurement and verifying that diffuse boundary scattering is the dominant mechanism responsible for the decrease in thermal conductivity of these nanowires at room temperature. The first experimental measurement of thermal conductivity performed on Si nanowires used nanowires bridged across microfabricated resistive heater-thermometers,³² and the diameter-dependent data was fit to a boundary scattering model which accounted for ballistic transport, which dominates at low temperatures.³⁰ At room temperature this model agrees well with the fully-diffusive model for nanowires of the same size as those used in the present study, yielding a predicted thermal conductivity of approximately $60 \text{ W m}^{-1} \text{ K}^{-1}$, also in excellent agreement with our measurements. We may furthermore compare to diameter-dependent measurements obtained using Raman thermography of unstrained, cantilevered Si nanowires (measured as-grown, such that contact resistance was negligible),³¹ from which we would predict nanowires of similar diameter to have thermal conductivity of $55 \text{ W m}^{-1} \text{ K}^{-1}$. Our contact resistances were determined to be on the order of $1 \text{ K } \mu\text{W}^{-1}$; with our experimental setup and sample dimensions, neglecting contact

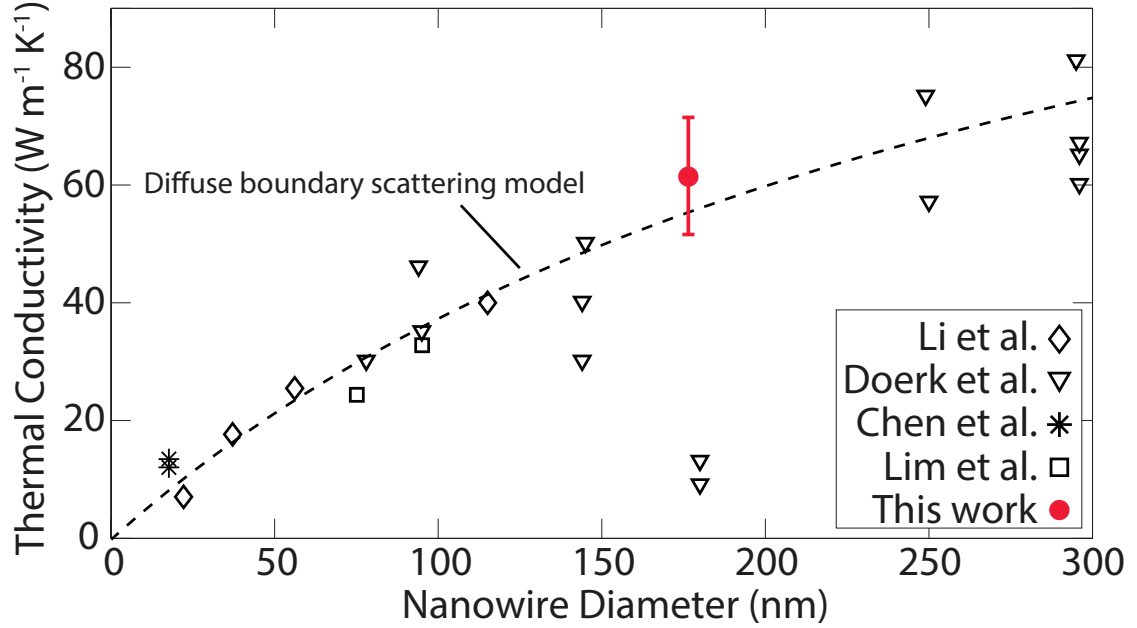


Figure 4.1: Thermal conductivity of undoped, VLS-grown Si nanowires from this work and the literature. Literature values are from Refs. 30, 32, 34. Our results are in good agreement with the diffuse boundary scattering model, verifying that this is the dominant mechanism responsible for the decrease in thermal conductivity of VLS-grown nanowires.

resistance would yield errors of 20-25%, highlighting the importance of measuring and correcting for this extra resistance.

4.1.2. Uniformly Strained Si Nanowires

With the method verified for unstrained Si, we applied uniform tensile strain to wire 1 (diameter $d=177$ nm) and measured thermal conductivity as a function of stress as shown in Figure 4.2. Our results using the exact analytical solution (Equation 3.3) were in excellent agreement with the thermal conductivities calculated

using the approximate solution based on thermal circuits (Equation 3.4). We found heat transport changes to be $<8\%$, well within our error bars, for tensile stresses as high as 1.7 GPa (equivalent to an elastic strain of 0.9%). We were unable to go to higher stresses due to the actuator heating issues discussed in Section 3.2.4, which limited the amount of load we could apply; we were furthermore limited by the unavailability of thinner Si nanowires of adequate crystal quality which would have allowed us to apply more stress. Our results are furthermore consistent with recent molecular dynamics (MD) simulations on Si nanowires in which the effect of strain on phonon frequencies and subsequent changes in phonon velocity and heat capacity were examined.⁴² The authors found that less than 1% strain applied to a 4 nm diameter nanowire would yield less than 1% reduction in thermal conductivity. Indeed, more than 7% strain was needed to achieve a 10% reduction, beyond the reported elastic limit of Si nanowires with these sizes.¹⁰ We may also compare our results to experiments on undoped bulk Si under hydrostatic compressive pressure up to 1 GPa,⁴⁹ or uniaxial compressive strain up to 0.3%⁵⁰ which found similarly small changes in thermal conductivity. Taken as a whole, our results suggest that uniform, uniaxial elastic strains below 1% do not substantially affect phononic transport in Si nanowires.

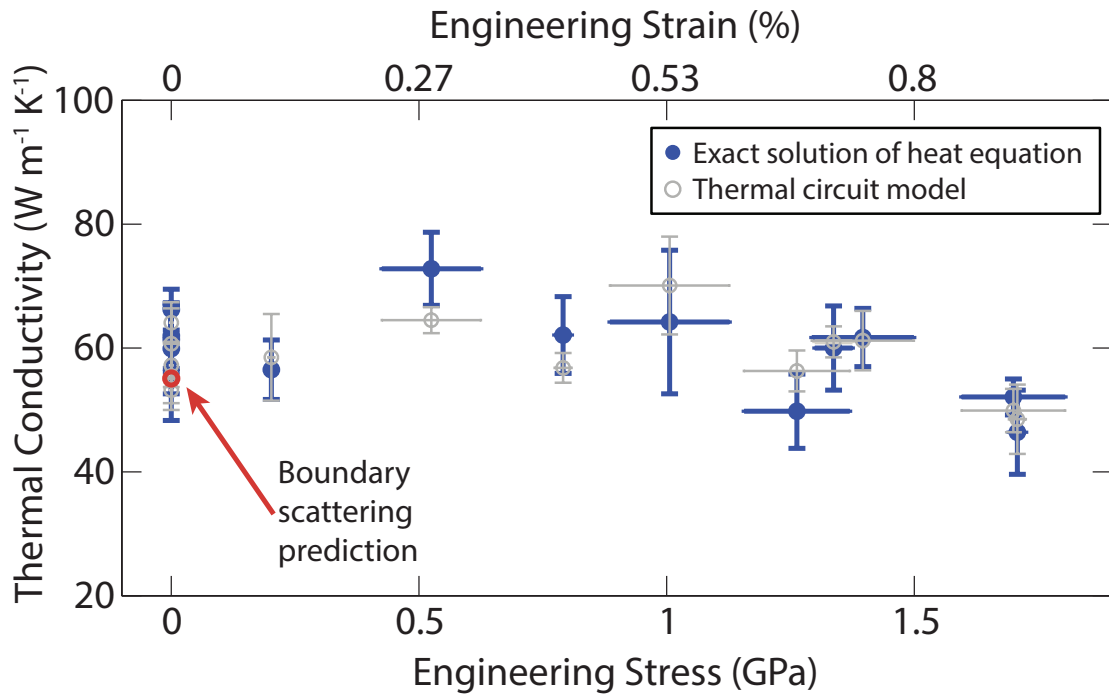


Figure 4.2: Thermal conductivity of an undoped, $\langle 111 \rangle$ -oriented Si nanowire as a function of applied engineering stress. Details regarding the two analysis methods are given in Chapter 3. No systematic change beyond the error bars is observed. The plotted boundary scattering model point is for comparison to Equation 4.1, which predicts a nanowire of this diameter to have thermal conductivity $55 \text{ W m}^{-1} \text{ K}^{-1}$. Engineering strain values were calculated using the Young's modulus measured from nominally identical nanowires, which demonstrated fully elastic behavior with no permanent strains for the strain ranges used here (see Chapter 2 and Ref. 148).

4.1.3. *Dependence of Raman Shift on Stress*

With our independent measurement of stress we were able to determine the stress dependence of the Raman shift. Figure 4.3 shows the change in room temperature peak position with respect to the unstrained nanowire for stresses up to 1.7 GPa. At $-3.5 \text{ cm}^{-1} \text{ GPa}^{-1}$, the slope of the linear fit here is in very good agreement with the relationship between Raman shift and stress along $\langle 111 \rangle$ predicted from lattice dynamics^{72, 149} as well as with experiments on uniaxially stressed bulk Si up to 1.2 GPa in compression^{73, 75} or 0.15 GPa in tension⁷⁶ along $\langle 111 \rangle$. This measurement is the first to be performed on a $\langle 111 \rangle$ -oriented Si nanowire, and due to the large range of elastic stresses accessible in Si nanowires, it is the also the highest-stress measurement of this relationship along $\langle 111 \rangle$ in Si.

4.1.4. *Estimates of Measurement Uncertainty*

Deflection of the load cell (proportional to stress) is measured using digital image correlation (DIC) both on loading and unloading, such that we have two measurements of stress for each increment. We observe no trends in the difference between the loading and unloading stresses with load, and we observe no systematic difference that would indicate that the wire or contacts plastically deform during collection of Raman data, so the difference between the loading and unloading stresses was taken to be the error on our measurements of stress. The mean difference across all stress measurements

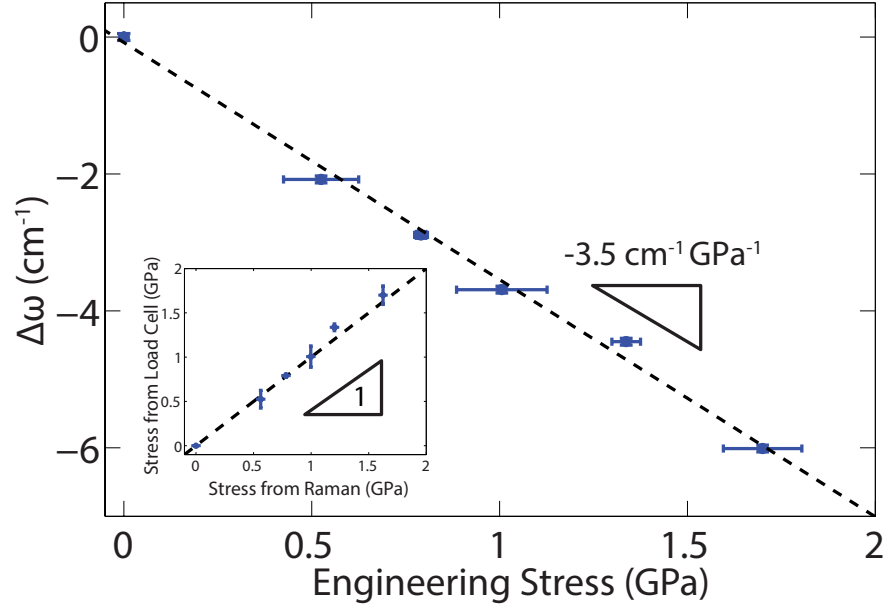


Figure 4.3: First-order Raman shift of the room temperature peak positions as a function of stress as measured using the MEMS-based load cell. The dotted line is the linear fit to this data and is in very good agreement with reports of this relationship for bulk samples in both tension and compression. Inset: Comparison between stress measured using the MEMS device and stress measured using Raman and the previously-determined relationship between Raman shift and stress for $\langle 111 \rangle$ bulk Si in tension ($-3.7 \text{ cm}^{-1} \text{ GPa}^{-1}$, Ref. 76). The dashed line represents perfect agreement between our stress measurement and the Raman-based stress measurement.

was 6 MPa (equivalent to strain $\sim 10^{-5}$).

We expect insignificant error in our stress or temperature measurement from thermal expansion and associated stresses in the mechanically clamped nanowire. Assuming the linear coefficient of thermal expansion for silicon is $2 \times 10^{-6} \text{ K}^{-1}$ and our temperature excursions are no more than 80 K, the maximum thermal expansion we would expect would be approximately 1 nm. Since our load cell has stiffness 44 N m^{-1} , this corresponds to 44 nN or 2 MPa of stress in the nanowire, corresponding to an

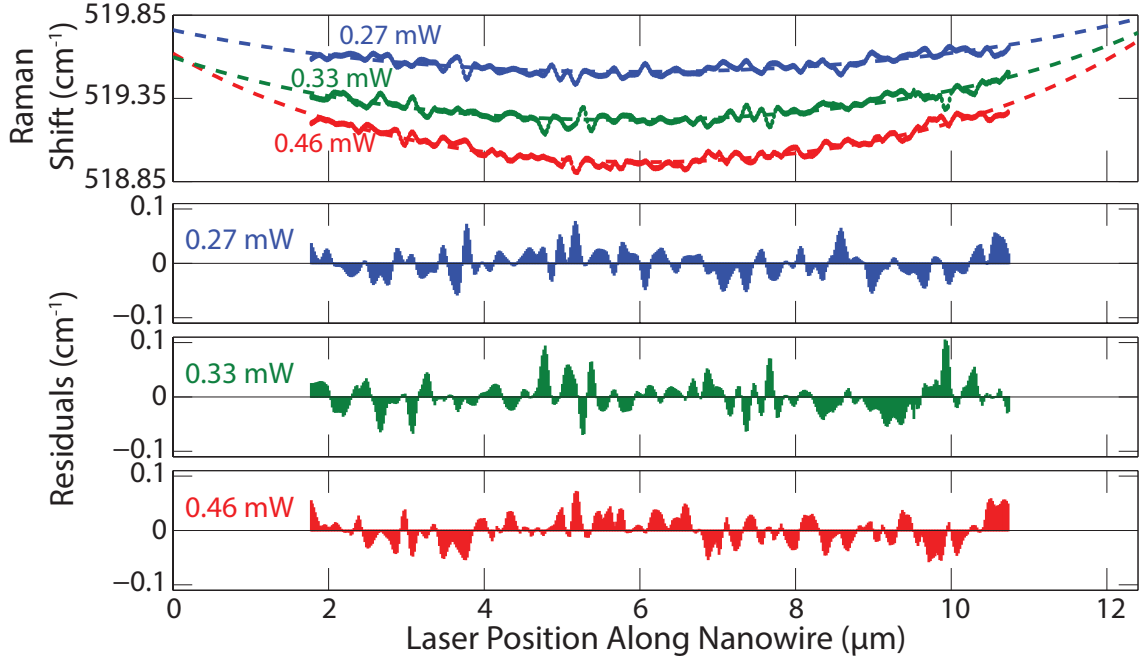


Figure 4.4: The fits shown in Figure 3.5a with accompanying residuals. The RMS values of the residuals for 0.27, 0.33, and 0.46 mW are 0.024, 0.028, and 0.025 cm^{-1} , respectively.

error in the Raman shift of 0.007 cm^{-1} , a negligible error.

We estimate the error on our temperature measurement by examining the 95% confidence intervals on the fits to each spectrum. The Lorentzian + Gaussian fits yield mean error on the peak position values conservatively below 0.05 cm^{-1} . The 95% confidence error on the linear fit which yields the room temperature peak position ω_{RT} is also $<0.05 \text{ cm}^{-1}$, so the error on $\Delta\omega$ is therefore $<0.1 \text{ cm}^{-1}$. The error on our determination of temperature is therefore $<4 \text{ K}$.

Thermal conductivity and contact resistance were measured from the temperature profiles with fitted curvature greater than $2.5 \text{ K } \mu\text{m}^{-2}$, which typically yielded 95%

confidence intervals on the fitting parameters within 20% of the mean values. The residuals of these fits, shown in Figure 4.4, are consistent with the error on the peak fits. Between 10 and 20 of the temperature profiles at each stress increment met this requirement; the error bars on Figure 4.2 represent the standard deviation of the resulting values of thermal conductivity using these profiles.

4.1.5. Defected Si Nanowires

The strain resulting from uniaxial tension is spatially uniform and thus affects phonon behavior primarily through changes to frequencies and hence heat capacity and group velocity. A contrasting view is that of strain incurred by lattice defects, which produce spatially nonuniform strain fields in the form of large strain gradients and may affect the phonon mean free path. One way to introduce a large density of point and line defects is by way of displacement damage resulting from ion irradiation. We examined the effect of a locally nonuniform state of strain by lightly irradiating a 5 μm section in the center of wire 1 and a 4 μm section of a similarly-sized wire (wire 2, $d=175$ nm) with a focused Ga^+ ion beam (30 kV, 20,000 \times magnification, and fluence 4 ions nm^{-2}) at normal incidence and without rotation about the nanowire axis. Although the precise temperature in the immediate sample environment during irradiation was unknown, the microscope chamber and stage were held at room temperature. Figure 4.5a shows a dark field transmission electron microscopy (TEM) image of wire 2 at the boundary between the irradiated and unirradiated regions, with

a selected area electron diffraction (SAED) pattern from the irradiated region inset. We observe a thin semi-shell (<25 nm) of partially-amorphized Si in the irradiated region, but the majority of the wire remains crystalline (although defected as evidenced by the SAED pattern which exhibits strong spots and very faint rings). There was no overall change in diameter or surface roughness.

Wires 1 and 2 exhibited drops in thermal conductivity of approximately 92% and 94%, respectively, as a result of irradiation. Figure 4.5b demonstrates this pronounced effect via the marked change in the relationship between laser power and peak position (slope proportional to thermal resistance, as per Equation 3.1) for wire 2 before and after irradiation. To verify that the apparent heating increases in the irradiated wires were due to changes in thermal conductivity and not to changes in absorption or in χ_T in the irradiated region, a third wire (wire 3, $d=171$ nm) was irradiated along a $1.5 \mu\text{m}$ length at the end of the nanowire such that all Raman measurements were performed on the pristine section of the nanowire. Changes in the heating profile for fixed laser intensity (Figure 4.5c) could then be attributed to changes in the resistance of the irradiated length of the nanowire. Here, a drop of 71% in thermal conductivity was observed for the irradiated section. The difference between the thermal conductivities measured using the two irradiation geometries could be due to small changes in absorption or χ_T in the irradiated region or due to changes in contact resistance upon irradiation which we were unable measure in this experimental geometry. Regardless, it is clear that the bulk of the apparent drop is due to a change

in thermal conductivity within the irradiated region.

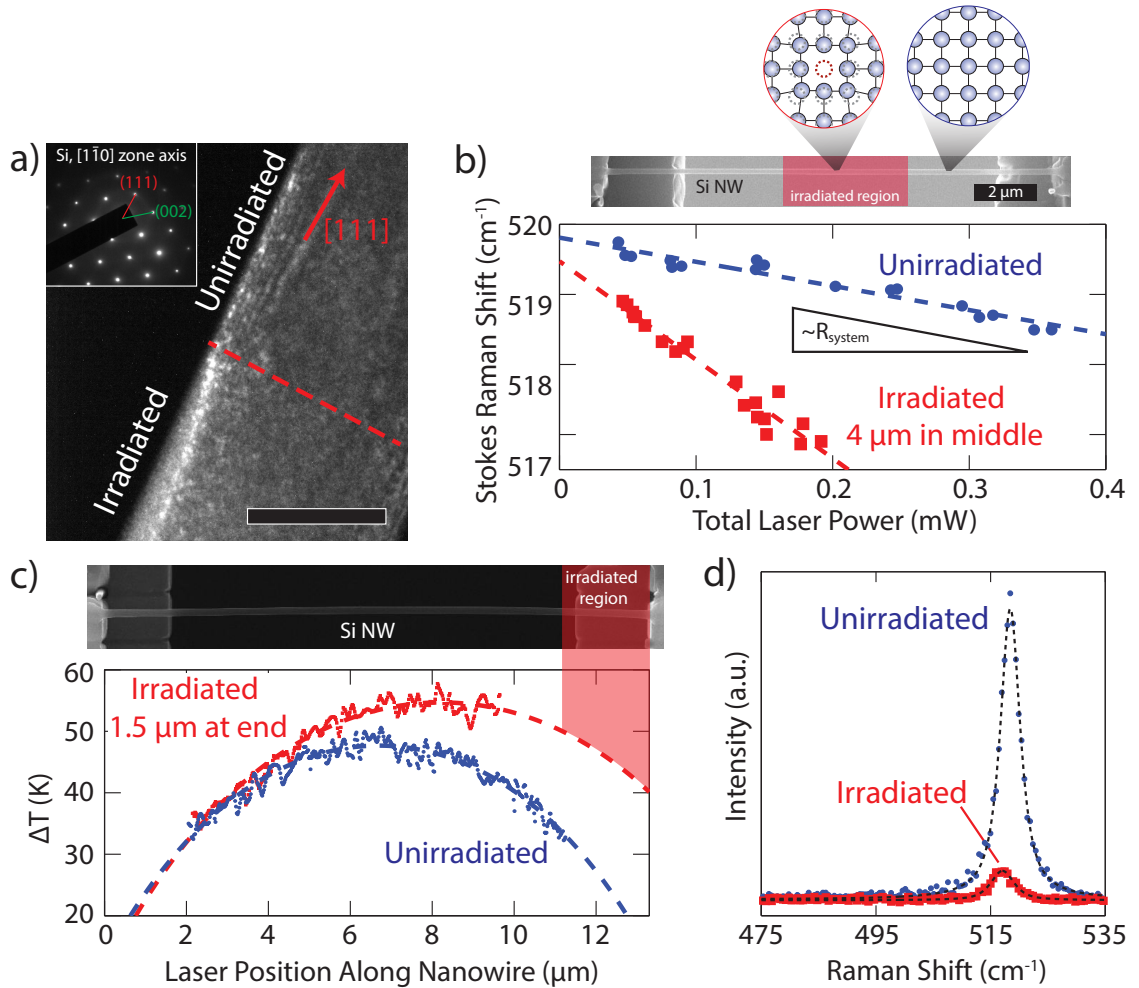


Figure 4.5: Thermal conductivity of irradiated Si nanowires. a) Dark field TEM image of the irradiated/unirradiated boundary of wire 2 using the (111) spot indicated in SAED pattern from the irradiated region, inset. Scale bar represents 100 nm. b) Raman shift as a function of incident laser intensity for wire 2 before (blue circles) and after (red squares) ion irradiation. The slope of this curve is proportional to the thermal resistance of the system. Measurements before and after irradiation were performed on the same day and within the same session in order to eliminate errors due to instrumental drift. c) Heating profiles for fixed laser intensity for wire 3 before and after irradiating one end near a grip. d) Direct comparison of representative Raman spectra from unirradiated and irradiated regions of wire 2 collected using the same laser intensity and collection time. Any amorphous peaks are undetectable.

We ascribe our decrease in thermal conductivity to the introduction of defects in the form of vacancies and implanted ions¹⁵⁰—and hence a locally nonuniform state of strain—throughout the nanowire volume. Our Raman spectra from the irradiated regions suggest more extensive disruption of the lattice than can be seen with TEM. Compared to the perfectly crystalline case, the first-order Raman peak for Si which has been disordered via either ion implantation¹⁵¹ or deposition conditions¹⁵² has been observed to be of lower Raman shift, lower intensity, and broader linewidth. As can be seen in Figure 4.5b, the room temperature peak position in the irradiated region is 0.3 cm^{-1} lower than in the unirradiated region. Furthermore, the intensity of the irradiated peak is lower by a factor of approximately 10 with no amorphous peak, as shown in representative Raman spectra collected from wire 2 in the irradiated and unirradiated regions within the same map (Figure 4.5d). Although difficult to measure compared to the changes in intensity or position, we detect some (6-14%) broadening in the irradiated regions beyond what would be expected with increasing temperature. The lowered shifts and intensities and increased linewidths we observe suggest phonon confinement with characteristic length scales smaller than the nanowire diameter, akin to systems with large fractions of planar defects (e.g. grain boundaries) such as nanocrystalline systems.^{153, 154} This interpretation is consistent with our TEM and SAED results, which indicate that the vast majority of the irradiated material maintains crystallinity, albeit with local disorder introduced via irradiation-induced defects, leading to the large measured drop in thermal conductivity. We may

exclude diameter and surface effects as causes of the dramatic lowering of thermal conductivity since we observe no changes to the nanowire surface. The diameter reduction of the crystalline core is also not sufficient to yield the observed $>70\%$ drops by comparison with diameter-dependent studies,^{30, 31} and the RMS roughness of the crystalline-amorphous interface was at most 1 nm greater than the surface roughness of the unirradiated wire, insufficient to yield the observed drops by comparison with systematic studies of roughness dependence.^{33, 34} A decrease in thermal conductivity with irradiation is additionally consistent with experimental reports on irradiated samples of bulk SiC^{155, 156} and microscale InN,¹⁵⁷ for which the surface and diameter effects prevalent at the nanoscale are negligible.

Our measurements suggest that the diminished thermal conductivity observed in studies of rough Si nanowires may in fact be due in large part to core rather than surface effects. Reports on the effect of surface roughness have all used metal-assisted chemical etching,^{22, 30, 33-35} a process known to, depending on the concentrations of the etchant components, lead to the formation of nanoporous nanowires.^{36, 37} It has not been unequivocally demonstrated that the etched nanowires used in these surface roughening studies did not also contain an increased concentration of atomic-scale pores and vacancies (which would not be observable in conventional TEM) as compared to pristine wires. Indeed, Raman spectra of etched Si nanowires with roughness controlled by the etch time have been reported to exhibit broadening of the first-order peak which increased with etch time,³³ indicative of increasing lattice disorder. Recent

MD simulations have examined Si nanowires with both surface roughness and core defects and found that a combination of the two is necessary to achieve the thermal conductivity decreases reported in the literature, with core defects responsible for the majority of the reduction.³⁸ Our measurement of a large drop in thermal conductivity without a significant increase in surface roughness is consistent with this notion, and it is clear that roughening approaches which do not modify the core must be developed and utilized to isolate the effect of surface quality on thermal conductivity.

Taken as a whole, our measurements imply that local perturbations to the crystalline lattice via core defects radically affect thermal transport in Si, whereas small, uniform elastic strains do so weakly. The decrease in Si thermal conductivity with uniform tensile strain arises from a reduction of phonon frequencies and hence heat capacity and phonon velocity.^{42, 158} For the elastic strains achieved here ($<0.9\%$), the change in zone-center phonon frequency is relatively small ($<1.1\%$, as seen from our room temperature Raman shifts) and the effect on thermal conductivity is also relatively small. This implies that uniaxial strain may be used to independently tune electrical properties without strongly influencing thermal transport, a promising indicator of the use of elastic strain engineering in applications benefiting from tunable charge transport or optical properties. Irradiation has a more drastic effect on thermal properties by significantly decreasing phonon scattering times due to defects, and for nanoscale systems where strong boundary scattering is prevalent, the overall thermal conductivity has been predicted to scale with vacancy volume fraction, ϕ , as $1/(1+a\phi^b)$

where a and b are fitting parameters.¹⁵⁹ Although point defects scatter phonons due to the mass difference with the host lattice as well as the large strain gradients around these defects,⁶⁰ the strain field effect likely dominates over the mass-difference effect.^{160, 161} For a single vacancy in Si, neighboring atoms may be displaced by as much as 18%, with higher displacements associated with divacancies or interstitial defects.⁶⁶ Thus, we may ascribe the majority of the thermal conductivity reduction to the large gradients in strain near point defects.

4.2. Si Micromeshes

Our previous finding that uniform strain affects thermal conductivity weakly, if at all, whereas defects have a strong effect motivates the need for a means of tunably applying heterogeneous states of strain in order to understand the effect of gradients on phonon scattering. It would furthermore be useful to find ways of isolating the strain gradient effect since the relative weights of the mechanisms behind phonon scattering from defects (strain gradients, mass-difference, changes in interatomic potential, interfaces, etc.) are not well studied in real systems. There are several means by which heterogeneous strain may be reversibly applied to a nanostructure, including bending or indenting within the elastic regime or straining a kinked nanowire or a micromesh. The last of these is attractive since we may draw parallels between a micromesh—a thin film containing pores which extend through the thickness—and a defected system. Pores may be considered similar to vacancy clusters in that they

are essentially missing atoms; however, the spatial extent of strain gradients near these pores would be relatively low compared to the size of the pores. This is in contrast to a vacancy cluster, where the volume of the distorted lattice is on the order of the volume of missing atoms.¹⁶² Applying a far-field load to a micromesh creates a heterogeneous state of strain such as that seen in Figure 4.6a, with varying strain states and magnitudes within the same structure, with the largest gradients near the holes, analogous to systems containing high vacancy concentrations. Although this analogy is imperfect, measurements of micromesh thermal conductivity both with and without strain may shed light on the relative importance of the mechanisms behind vacancy scattering as well as provide another means of engineering materials thermal conductivity.

4.2.1. Tensile Bar and Micromesh Fabrication

Free-standing Si tensile bars were fabricated in the device layer of commercially-available (100) silicon-on-insulator (SOI) wafers with the axis along the $\langle 110 \rangle$ direction. Dogbone patterns were created using photolithography and transferred by reactive ion etching (RIE) in SF_6 . The oxide layer was then dissolved in an HF bath so that the tensile bars detached from the wafer. The resulting tensile bars were approximately 1.5-1.7 μm thick, 1 mm long in the straight part of the gauge section, and 95 μm wide. A representative optical image of a tensile bar can be seen in Figure 4.6b. Micromesh patterns spanning the width of the tensile bars and

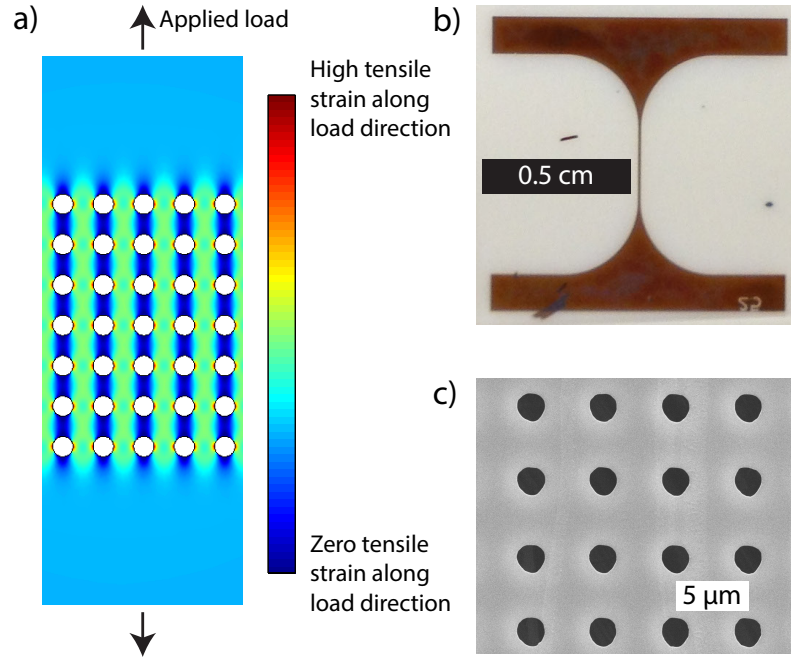


Figure 4.6: Strained Si micromeshes for reduced thermal conductivity. a) Finite-element model demonstrating a complicated strain state achievable by applying a uniaxial load to a micromesh structure. Only the center of a wide mesh is shown. The colorbar is a linear scale; the strain state is self-similar for all applied loads up to fracture. Strain at the edges of the pores is approximately $3\times$ the far-field strain. b) Optical image of a fully dense tensile bar fabricated by Dr. Brian Piccione at Penn. c) SEM image of a FIB-milled mesh pattern.

approximately $80\ \mu\text{m}$ along their length were created by FIB milling using Ga^+ at 30 kV accelerating voltage and 20 nA beam currents. The patterns contained pores 1.9-2.1 μm in diameter with 4.9-5.1 μm spacing; the size and spacing were guided by the resolution of the ion beam at beam current practical for fabrication of these patterns. A representative SEM image of a portion of the mesh may be seen in Figure 4.6c.

4.2.2. Uniformly Strained Si Films

Before testing tensile bars with the micromesh pattern, we developed a method of applying strain to fully dense (i.e., without a mesh pattern) tensile bars and measuring thermal conductivity. The device shown schematically in Figure 4.7a was used to apply strain to the tensile bars. Si supports were attached to a PDMS strip measuring approximately 1×4 cm using PDMS precursor and cured. The PDMS strip was then placed in the device, which consists of two clamps which are free to slide in one dimension on guide bars. Tensile bars were aligned parallel to the guide bars and attached to the Si supports such that the tensile bars were suspended several hundred microns above the PDMS. Strain was applied using a micrometer positioning stage and then fixed using set screws. Although there is no load cell incorporated in the device, elastic strain may be measured using shifts in the room temperature peak position with strain, as in Section 4.1.3, and converted to stress using the bulk Young's modulus for $\langle 110 \rangle$ Si of 169 GPa. It is important to note that in applying this method to the tensile bars, where strain is applied along the $\langle 110 \rangle$ direction, a different relationship exists between stress and Raman shift from the $\langle 111 \rangle$ -oriented nanowires, and the literature value of χ_σ was used.^{76, 149} We additionally measured strain by collecting optical images of a “dirty” region of the tensile bar containing some surface debris at each strain increment and performing digital image correlation (DIC) to determine strain. The Raman- and DIC-based methods were found to be in excellent agreement (see Figure 4.8).

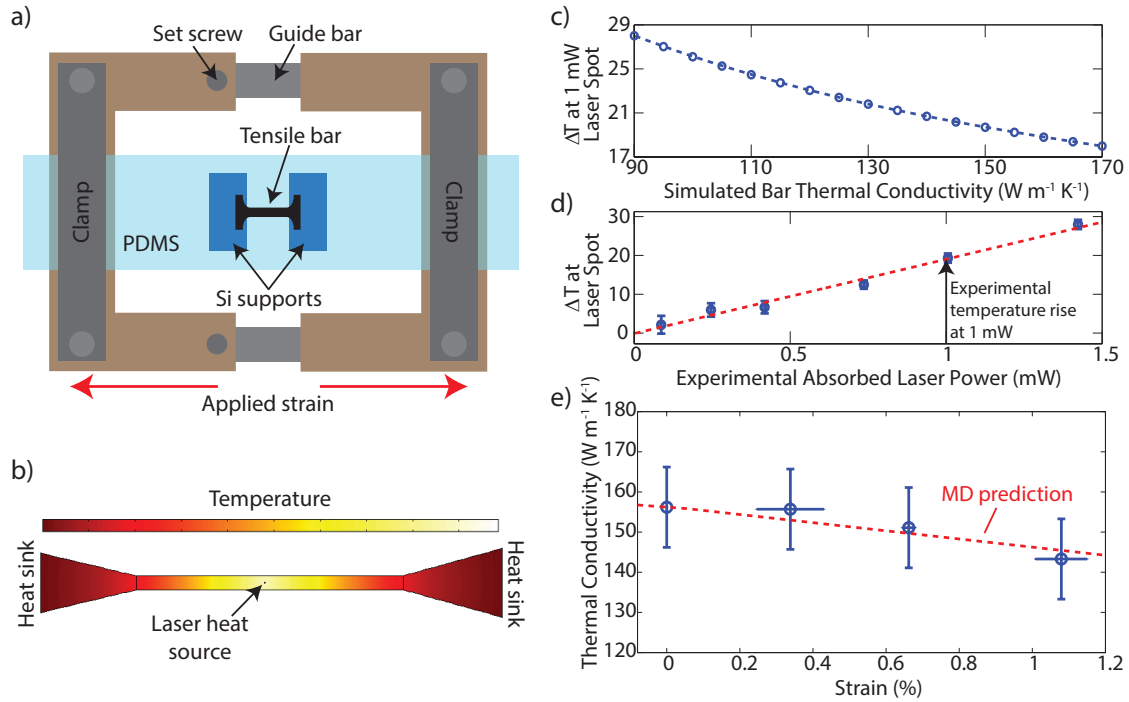


Figure 4.7: Thermal conductivity measurements of strained Si films. a) Top-down schematic of device used to strain Si thin film tensile bars. The structure is suspended above the PDMS strip by pieces of Si wafer. The PDMS is clamped at both ends, and the entire device is pulled using a micrometer stage. Set screws fix the strain so that the device can be placed under the objective of the Raman microscope. b) Example of simulated temperature distribution in a laser heated fully dense tensile bar. c) The simulated temperature rise at a 1 mW laser spot for various tensile bar thermal conductivity values. d) Experimental temperature rises at the laser spot for various absorbed laser powers for an unstrained tensile bar. The temperature corresponding to 1 mW from the linear fit was compared to the simulation results seen in (c) in order to calculate thermal conductivity. e) Thermal conductivity of a fully dense tensile bar as a function of strain along the $\langle 110 \rangle$ direction. Horizontal error bars represent the differences between the two strain measurement methods (Raman and DIC). The MD prediction is for relative changes in thermal conductivity with strain in bulk Si from Refs. 42, 158 and is in excellent agreement with our results.

The more complicated geometry of the micromesh structures does not allow for the direct application of the mathematical model used for quasi-1D systems. As such, a model was developed using finite-element software (COMSOL Multiphysics, Heat Transfer in Solids module) to calculate the temperature rise at the center of a fully dense tensile bar (with or without a micromesh) for a given absorbed laser power, heat transfer coefficient, and tensile bar geometry. The laser was treated as a cylindrical heat source with diameter the same as the FWHM of the laser spot (570 nm). An example of a calculated temperature distribution may be seen in Figure 4.7b. The simulation was run for several values of the thermal conductivity; the predicted average temperature rise for these values within the simulated laser spot (Figure 4.7c) could then be compared to experimentally realized temperature rises (Figure 4.7d) at the same absorbed laser power in order to determine thermal conductivity. When applying this method to tensile bars containing micromeshes, the mesh was treated as a separate material and the simulation was run sweeping over the micromesh thermal conductivity, with the rest of the bar taking the thermal conductivity determined from measurements of the fully dense tensile bar.

We found an unstrained, fully dense tensile bar of thickness $1.65 \pm 0.01 \mu\text{m}$ to have room temperature thermal conductivity nearly identical to that of bulk Si, as would be expected for a sample of this size.^{67, 133, 162} Up to 1% tensile strain was applied to the tensile bar, and up to 8% decrease in thermal conductivity was observed. These results are also as would be expected by comparison with our results on uniformly

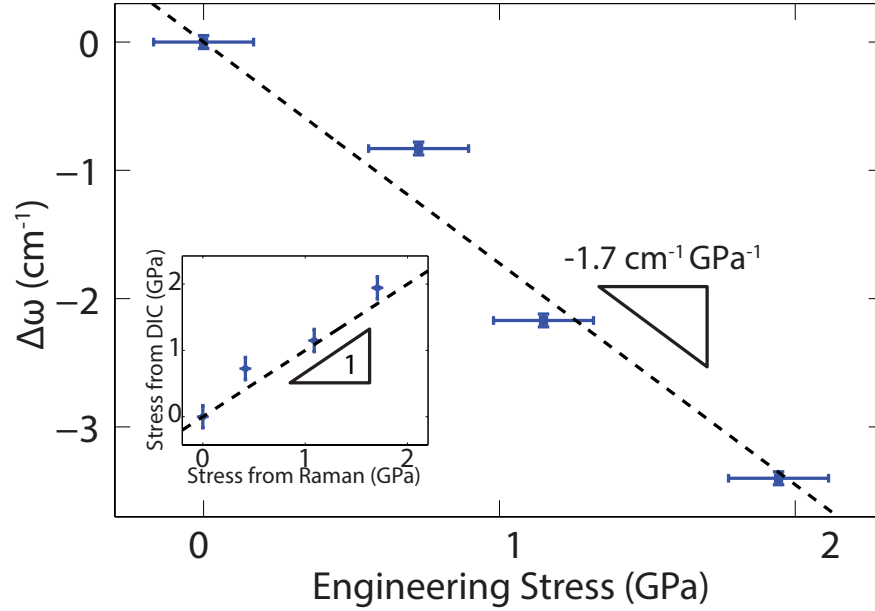


Figure 4.8: Raman shift of the room temperature peak positions as a function of stress as measured using DIC on the “dirty” part of the tensile bar. The dotted line is the linear fit to this data and is in very good agreement with reports of this relationship for bulk samples. Inset: Comparison between stress measured using DIC and stress measured using Raman and the previously-determined relationship between Raman shift and stress for $\langle 110 \rangle$ bulk Si in tension ($-2.0 \text{ cm}^{-1} \text{ GPa}^{-1}$, Ref. 76). The dashed line represents perfect agreement between our stress measurement and the Raman-based stress measurement.

strained nanowires and with recent MD simulations which predict a 6% decrease in bulk Si thermal conductivity with 1% uniaxial tensile strain.^{42, 158} Although all of our measurements are within the error bars (calculated based on the standard deviation of the Raman shift), the trend toward decreasing thermal conductivity with tensile strain seen in Figure 4.7e is clear and is consistent with theoretical predictions.

4.2.3. *Strained Si Micromeshes*

We applied the piezothermography method used for fully dense Si to two nominally-identical micromesh structures and measured thermal conductivity as a function of far-field strain. The far-field strain was determined by collecting low-power spectra away from the mesh, in the bulk-like part of the tensile bar. We were unable to collect high quality images for performing DIC verification of strains for these samples, but as we previously showed, Raman spectra alone are sufficient for determining strain. We note that Raman spectra obtained from the etched sides of these meshes are of considerably lower intensity than spectra collected from the unetched back sides, indicating FIB damage as with the irradiated nanowires. Thermal conductivity measurements were therefore performed using spectra from the back sides of the tensile bars. We repeated our measurement procedure and performed finite-element modeling, as in Section 4.2.2, in order to determine thermal conductivity of these meshes.

Unstrained micromeshes exhibited thermal conductivities of 20-21 W m⁻¹ K⁻¹. This is approximately half what we'd expect by comparison with mesh structures of roughly similar dimensions (4.5 μm thickness with 2.3 μm-diameter pores and 4 μm spacing, fabricated by Song and Chen using deep reactive ion etching¹⁶³), and we attribute the difference to our use of the FIB to fabricate the pores. As we saw with the fully dense tensile bars, the thickness of these films does not affect thermal conductivity. We showed in Section 4.1.5 that for nanowires even small amounts of ion irradiation can drastically affect thermal transport, and the high beam currents (20 nA) and

long etch times (>20 minutes) needed to create these meshes will inevitably damage the remaining Si. Our measurements probe the total thermal conductivity of the system, which we have treated as consisting of pristine Si, but in reality our system is a gradient of FIB-damaged Si, from nearly amorphous on the etched surface to pristine on the back side, though the shape of this gradient and the thickness of the damaged region is unknown. It is therefore not surprising that we measure lower thermal conductivity than expected by comparison to similar films fabricated using cleaner methods. However, since we are interested primarily in changes in thermal conductivity with strain (i.e., $\Delta\kappa/\kappa$), the FIB damage and resulting reduced thermal conductivity is acceptable.

We observed measurably nonuniform strains within the mesh region for far-field strains above 0.08% and up to 0.32%, after which the tensile bars fractured. The strain patterns were self-similar at all strains, and an example may be seen in Figure 4.9a for 0.32% far-field strain. The strains in the center of a ligament along the direction of applied load (dashed line in Figure 4.9a) are shown in Figure 4.9b for far-field strains of 0.32% and 0.10%. Both sets of data are fit to sinusoidal curves with the same period and goodness of fit; they differ in amplitude and offset only. The measured strains exhibit good agreement with the theoretically predicted strains shown in Figure 4.6a, with the highest strain at the edges of the pores perpendicular to the direction of applied strain and nearly zero strain between pores parallel to the direction of applied strain. Spectra obtained from inside the pores had negligible Si Raman peak intensity

and may be disregarded.

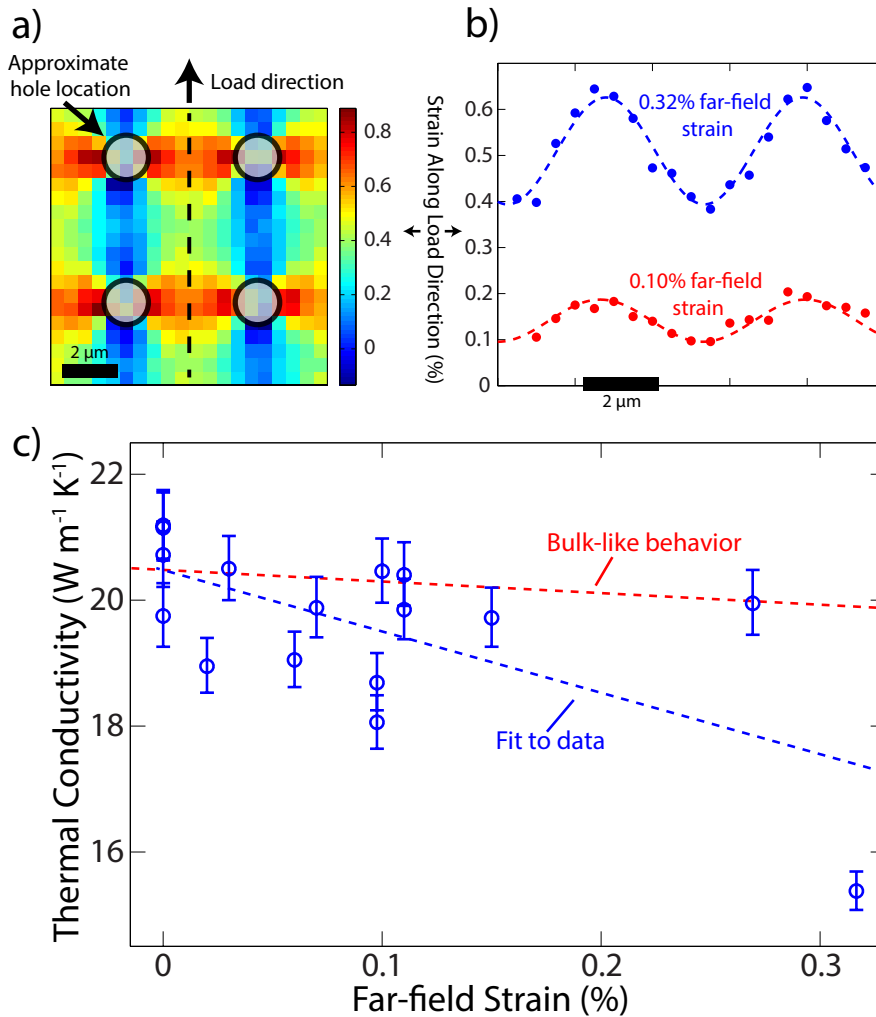


Figure 4.9: Thermal conductivity measurements of strained Si micromeshes. a) Nonuniform strains in a mesh with far-field strain 0.32% as measured by Raman spectroscopy. Strains in the pores are artifacts of the spectral fitting procedure—Si Raman signals from those regions were negligibly low. b) Strains along the centers of the ligaments parallel to the direction of loading (dashed line in (a)) for two strain increments. Both profiles are sinusoidal with the same period. c) Thermal conductivities of two nominally identical Si micromeshes as a function of far-field (in the bulk part of the tensile bar) strain. From the slope of the linear fit we predict a 4.8% decrease in thermal conductivity for each 0.1% of applied far-field strain. The expected thermal conductivity for a bulk-like strain dependence is shown in red.

We observed decreasing thermal conductivity in the two nominally identical Si micromeshes with increasing far-field strain—equivalently, increasing strain gradients within the mesh—far beyond what we observed for uniformly strained Si, as seen in Figure 4.9c. The linear fit to these data suggests a 4.8% decrease in thermal conductivity for every 0.1% applied far-field strain. The maximum strain in the mesh, at the edges of the pores, is about $3\times$ the far-field strain, so this is equivalent to a 1.6% decrease in thermal conductivity for every 0.1% increase in the maximum strain in the mesh. For the fully dense tensile bars, we observed just 0.8% decrease for every 0.1% applied strain, a far smaller change than what we measure in the meshes. We confirmed that no permanent deformation such as defects or microcracks was responsible for the decrease in thermal conductivity at least up to 0.15% far-field strain, since thermal conductivity recovered upon unloading (we were unable to perform unloading tests beyond 0.15% due to sample failure). These results therefore show that heterogeneous strain is a far more effective modifier of thermal conductivity than uniaxial strain, since the changes in thermal conductivity in strained meshes outpace the changes in thermal conductivity for uniaxially strained systems. We note that we could expect the effect to be stronger in heterogeneously strained materials not containing a high defect concentration, as ours do due to the use of FIB milling, since the phonon scattering time in our unstrained system is already low. It would also be stronger in nanostructured Si or other materials, e.g. graphene, which can accommodate more strain, since our samples fractured at maximum strain $\sim 1\%$ in the

mesh, consistent with the fracture strain of the bulk-like Si thin films studied earlier.

Thorough simulations will need to be performed in order to fully understand these results, and to our knowledge strain fields which vary over such long distances or do not arise from some defect have not been studied. In general, it has been known since the 1950s that the decrease in thermal conductivity in defected systems (e.g. vacancies, dislocations, grain boundaries) arises in part from the introduction of structural disorder and subsequent breaking of lattice symmetry, as well as spatially-varying interatomic force constants. These increase vibrational anharmonicity and hence phonon scattering, reducing the phonon scattering time τ .^{60–62, 164–166} More recently, simulations by Meng *et al.* demonstrated that the magnitude and spatial extent of the interfacial strain field between two different crystals partly determines the scattering rate with a strong dependence on phonon wavelength—phonons with wavelength shorter than the thickness of the strained region are more likely to scatter.¹⁶⁷ This may help explain why we observe decreases in thermal conductivity without introducing smaller length scales. A similar study incorporating the full strain tensor and phonon dispersion could shed light on our findings as well as allow for an optimization of the mesh pattern for tuning thermal conductivity.

4.3. Conclusions

We have measured the effect of both globally homogeneous and locally nonuniform strain on thermal conductivity in single Si nano- and microstructures using Raman

piezothermography. Up to 1.7 GPa of uniaxial tensile stress was applied to a $\langle 111 \rangle$ Si nanowire, and spatially resolved maps of Raman spectra at several laser powers were used to decouple the effects of strain and temperature in order to calculate thermal conductivity. A weak strain effect on thermal conductivity was observed for these uniaxially strained nanowires, but when core defects and thus nonuniform states of strain were introduced via Ga^+ irradiation, near-order-of-magnitude decreases in thermal conductivity were realized. Our results also show that thermal conductivity decreases in nanowires previously attributed to surface roughness may in fact be due to core defects created during the fabrication of roughened nanowires.

A large portion of the phonon scattering from point defects is believed to be due to enhanced phonon scattering from the large strain gradients surrounding these defects, but decoupling this mechanism from others, such as mass-difference scattering, is experimentally quite challenging. To address this, we developed a means of isolating the effect of strain gradients from other effects by applying elastic, heterogeneous strain—namely, by straining a Si micromesh. After verifying that the method developed for nanowires could be adapted to thin film-type structures by measuring thermal conductivity of a bulk-like film under strain, we applied the method to a micromesh structure. We found we could reduce the thermal conductivity of the micromesh by up to 15% before fracture, far outpacing the reductions we achieved in bulk-like films due to increased phonon scattering by strain gradients. Although the sizes and periods of the strain gradients achieved in the micromeshes differ widely from the gradients

near vacancies, dislocations, interfaces, or grain boundaries, this is, to our knowledge, the first experiment to isolate the role of strain gradients in phonon scattering in crystals, with important implications for the understanding of phonon scattering mechanisms from defects. These experiments also suggest a variety of new, previously unexplored directions for controlling thermal conductivity by using heterogeneously strained structures to improve thermoelectric properties or design thermal transistors, rectifiers, or adaptive barriers. Some of these new directions will be discussed further in the next chapter.

Chapter 5

Conclusions and Prospectives

In this dissertation, we have described uniaxial tensile testing of nanowires, with particular attention paid to the compliance of the clamps typically used in nanomechanical testing. We then combined our tensile testing method with a novel method of measuring thermal conductivity of strained Si nanowires using Raman spectroscopy. We extended this method to irradiated Si nanowires, Si thin films, and Si micromeshes. We found uniform, uniaxial strain to have little effect on thermal transport within the ranges of strain we were able to apply (see Figure 5.1), but nonuniform strain applied via the introduction of vacancies, in the case of nanowires, or in strained micromeshes led to more significant decreases—up to 75% and 15%, respectively—in thermal conductivity. This implies that the uniform strain effects on thermal conductivity via changes in heat capacity and phonon velocity are much weaker than the effect of enhanced phonon scattering from strain gradients. The novel methods presented here will allow for a wide array of measurements on other systems, and our results suggest several interesting new directions in materials research, some of which we describe below.

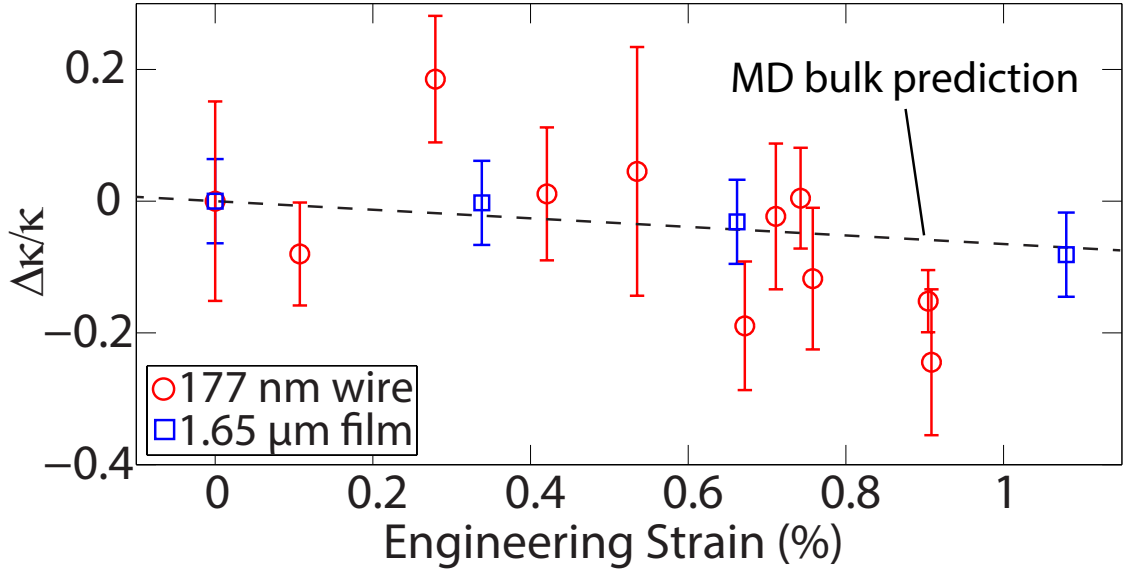


Figure 5.1: Thermal conductivity of strained Si nanowires and thin films. The MD prediction is for relative changes in thermal conductivity with strain in bulk Si from Refs. 42, 158.

5.1. Si Nanomeshes

We have demonstrated that thermal conductivity of a Si micromesh may be decreased by over 15% with the application of strain due to the presence of large strain gradients, but additional experiments as well as more robust simulations and theory will be needed to understand the effects of strain gradients on thermal transport. Our approach has several limitations which should be addressed. First, since we have used bulk-like Si with all critical dimensions $>1\mu\text{m}$, the system exhibits bulk-like fracture strength. Far-field strains only up to 0.32% (maximum $\sim 0.9\%$ in the mesh) were achievable before the system failed, and these low strains limit the range of attainable thermal conductivities. Second, our use of the FIB complicates any effort

to quantitatively describe the strain gradient effect, since the extent of the ion damage is unknown. Strain gradients may furthermore affect the more heavily FIB-damaged regions of the mesh differently than the pristine regions. Lastly, we would expect thermal conductivity to be fairly anisotropic in a mesh structure, but our experimental setup necessitates the assumption of isotropy.

Many of the limitations described above could be overcome by instead using a Si *nanomesh* structure fabricated not with the FIB but with deep reactive ion etching (DRIE) so that a pristine crystal structure would be maintained throughout the mesh thickness. Patterns could be created and transferred following recent methods of nanomesh fabrication using photolithography¹⁶³ or e-beam lithography.¹⁶⁸ Using silicon-on-insulator (SOI) wafers with thinner device layers or creating meshes with thinner ligaments between pores would allow for exploitation of the well-known increase in fracture strain observed in nanoscale Si. Since the spot size of a typical Raman laser is on the order of 100s of nm, it would be difficult to map gradients as we did in Figure 4.9a. However, if a large gradient exists over the laser spot size, the Raman peak will broaden as the laser simultaneously samples from regions of high and low strain. This may serve as a useful metric of strain gradient when mapping the spatially varying peak position becomes untenable. In order to explore the effect of anisotropy, it would be useful to rotate the pattern by 45° as in Figure 5.2. Other patterns (e.g. hexagonal packing) or pore shapes (e.g. squares or fins) could also be fabricated in order to vary the gradients and optimize the range of available thermal

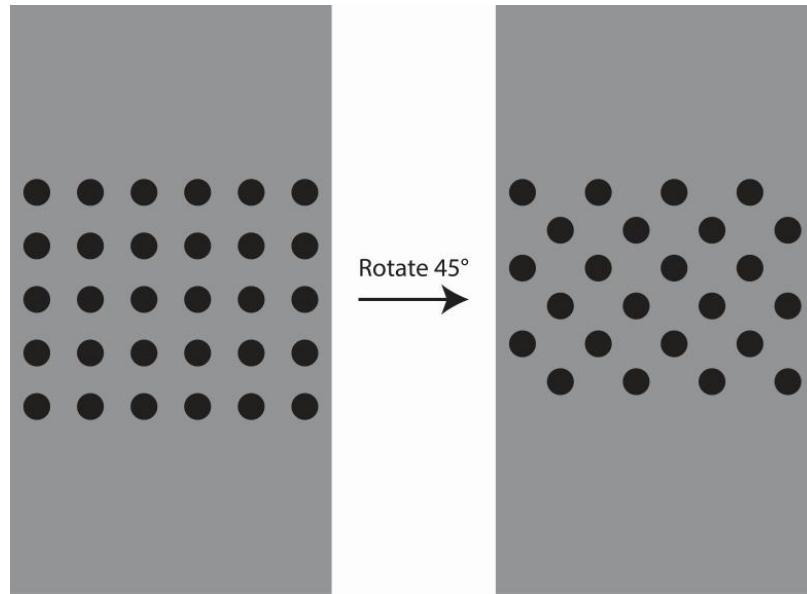


Figure 5.2: Pattern rotation for exploring anisotropy in Si nanomeshes. This rotation effectively moves the heat sinks so that thermal conductivity along different directions may be probed.

conductivities.

Although we expect our decreases in thermal conductivity with nonuniform strain to arise from increased rates of phonon-phonon (Umklapp) scattering, further steps should be taken to prove this is the case. If it is the primary mechanism, there should be a stronger temperature dependence of thermal conductivity in heterogeneously strained systems due to changes in phonon population with temperature and hence changes in phonon-phonon scattering rate (see, e.g., Equation 1.17, Ref. 39, or the review by Berman¹⁶⁹). The experimental setup could be adapted for a cryostat and the experiment repeated for both strained and unstrained meshes at various temperatures. A change in the thermal conductivity dependence on temperature (e.g. the slope of

$\kappa(T)$) between strained and unstrained meshes would indicate changes in rates of phonon-phonon scattering. We note that attempting to raise temperature by increasing laser power would only do so locally and would be insufficient for determining the overall thermal conductivity of the mesh. Care should also be taken to avoid changes in strain due to thermal expansion or contraction when performing these tests away from room temperature.

5.2. Other Materials for Tunable Thermal Conductivity

Aside from stress applied to meshes, other opportunities exist for applying controlled, reversible, nonuniform strains in order to more thoroughly understand the effect of gradients on thermal transport. The simplest nonuniform strain state is that of a constant gradient, which could be achieved by applying uniaxial strain to a structure of constantly varying cross-sectional area. Greil *et al.*¹⁷⁰ demonstrated this by straining a tapered Ge nanowire, using Raman to verify the constant gradient. Thermal conductivity measurements on a similar structure would best isolate the effect of strain gradients in controlling transport. Conversely, bending or buckling of straight nanowires will create strain gradients in the direction perpendicular to the nanowire axis. More complicated strain gradients may be achieved in more complicated structures. For instance, several groups have recently synthesized kinked Si,^{171, 172} Ge,^{171, 173} CdS,¹⁷¹ and ZnO^{174, 175} nanowires. Pulling a kinked nanowire in tension will result in stress concentrations—and hence large strain gradients—near the kinks,

which we expect would decrease their thermal conductivity. Two-dimensional systems present further opportunities, in part due to their ability to accommodate large elastic strains¹⁷⁶ and in part due to the availability of more complicated strain states. For instance, twisting should decrease thermal conductivity of graphene.¹⁷⁷

5.3. Further Applications of Raman Piezothermography

We expect the method presented here to be widely applicable for characterizing the thermal and phononic behavior of any Raman-active system which may be laser-heated. Determination of the room temperature peak position makes the method particularly useful when the positions of peaks in the Raman spectrum do not exactly correspond to the bulk due to not only strain but nanostructuring, doping, or defects. Attractive candidates for Raman piezothermography should have strong Raman signals in order to minimize collection time, since long collection times can often make mapping difficult due to sample or microscope drift. The dependence of the Raman peak on temperature would also need to be constant with strain; highly nonlinear elastic materials should be approached with care. Isolated, non-overlapping peaks will also allow for more accurate determination of relative shifts. Selected materials which meet these criteria and should also show a strain dependence of thermal conductivity are described below.

5.3.1. Graphene

Perhaps the most natural extension of Raman piezothermography is to graphene, the first nanomaterial studied with Raman thermography.^{122, 123} Like 1D systems, graphene may accommodate far more strain prior to fracture than its bulk counterpart, graphite. For instance, the uniaxial tensile strength of graphene has been demonstrated to be over 100 GPa or 10% strain,¹⁷⁸ meaning that there is a very large range of elastic strain over which to tune properties. The Raman spectra of graphene under strain have also been well-characterized.^{176, 179–183} Graphene should furthermore exhibit a large decrease in thermal conductivity with tensile strain, as evidenced by many recent simulations,^{42, 177, 184–189} due to rippling and changes in phonon dispersion and density of states. Graphene exhibits some measurable nonlinear elastic behavior,¹⁹⁰ which for Raman piezothermography purposes would have to be accounted for at high strains, but this should manifest as more drastic decreases in thermal conductivity with strain. The experimental setup shown in Figure 4.7 could be directly adapted by exchanging the PDMS support with graphene supported by some flexible substrate, as was recently achieved by Bisset *et al.*¹⁸² with both PMMA and PDMS in order to study the effect of grain boundaries on the Raman spectra of uniaxially strained graphene, or by Wang *et al.* with polyimide supports.¹⁹¹ For thermal studies, it would be necessary to fabricate a hole or indentation in the support, so that the region of the graphene under investigation would be suspended. Alternatively, a dry transfer method such as that used by Zhang *et al.*¹⁹² could be used to place a flake of graphene

across the grips of a MEMS-based or push-to-pull style tensile testing device. Such a study would be valuable for understanding and controlling the thermal behavior of graphene-based flexible devices^{193, 194} as well as for validating theoretical predictions.

5.3.2. Piezoresistive Systems

Our measurements represent equilibrium values and thus probe the total thermal conductivity (κ_{total}), which includes contributions from both charge carriers (κ_e) and the lattice (κ_l), as per Equation 1.6. Room temperature, undoped Si has κ_e on the order of $1 \text{ nW m}^{-1} \text{ K}^{-1}$, whereas $\kappa_{total}=150 \text{ W m}^{-1} \text{ K}^{-1}$,³⁹ but systems with very low thermal conductivity and highly strain-sensitive electrical conductivity may exhibit a more significant effect. SiGe nanowires are a good example of this: their thermal conductivity is nearly an order of magnitude lower than single-crystal Si nanowires of the same size¹⁹⁵, but they have piezoresistive gauge factors several times that of Si,¹⁹⁶ making them a potentially interesting avenue of research.

5.4. Size Dependence of the Heat Transfer Coefficient

Nanowires have been proposed as a useful system for rapidly transferring heat between solids and liquids or gases due to their high surface-to-volume ratio and enhanced heat transfer coefficients.¹⁹⁷ The degree of thermal transfer from a nanostructure to a surrounding medium is also of interest for device cooling,¹⁹⁸ thermoelectric,¹⁹⁹ and solar thermal¹⁴⁷ applications. Furthermore, the value of the heat transfer coefficient

is needed in order to measure thermal conductivity in air using *any* method, not just the one described here. These measurements are far easier in ambient conditions than at low pressure (where it may be assumed that $h \sim 0$) in that they require less experimental consideration for sample stability in vacuum or of the size of a vacuum chamber. At the macroscale, the diameter dependence of the heat transfer coefficient is well-understood using continuum models, but this relation breaks down when sample size approaches the mean free path of air molecules (67 nm, Ref. 146). Models for nanoscale spheres¹⁴⁷ and cylinders^{144, 145} have been developed, and some experimental studies have been performed for nano- and microwires,^{143, 145, 200} but a comprehensive, experimentally-verified model over a wide range of nanowire diameters has not been produced. Moreover, all of these reports relied on an assumed value of the wire's thermal conductivity. This is particularly troubling since, as we saw in Section 4.1.5, small numbers of defects can have a large effect, as can other aspects of the system such as grain boundaries or surface roughness, none of which were characterized. The method of simultaneously determining thermal conductivity and the heat transfer coefficient by performing the same measurement on the same nanowire with different clamp geometries as described in Section 3.2.6 is unique in that it allows measurement of the heat transfer coefficient without the need for prior knowledge of the nanowire's thermal conductivity. We therefore propose a systematic, diameter- and shape-dependent study of nanoscale heat transfer to air at atmospheric pressure using this method. The dependence of the heat transfer coefficient on the mean free

path and heat capacity of air could furthermore be explored by varying pressure or gas species. Such a study would be valuable for a wide variety of applications as well as enabling deeper understanding of thermal transport across interfaces.

5.5. Strain Effects on Seebeck Coefficient

As discussed in Chapter 1, nanostructured Si has thermoelectric efficiency orders of magnitude higher than bulk, largely due to changes in thermal conductivity. The thermoelectric figure of merit ZT (Equation 1.1) depends on electrical conductivity, thermal conductivity, and Seebeck coefficient ($S = -(\Delta V/\Delta T)|_{I=0}$). Electrical conductivity is known to be highly sensitive to strain (see, e.g., Refs. 11, 18–20, 104, 201, 202), whereas thermal conductivity is relatively insensitive to uniform strain and sensitive to nonuniform strain, as we have shown. However, no experiments have been performed examining the effect of strain on Seebeck coefficient, despite several simulations showing that, with proper choice of doping and orientation, strain can improve it in many materials.^{203–207} Such experiments could be tackled by integrating the microfabricated devices used for static Seebeck coefficient measurements^{21, 22} with a MEMS-based tensile testing device such as the one used here. Alternatively, the heaters, thermometers, and leads used for those measurements could be directly fabricated onto the tensile bars discussed in Chapter 4. If photocurrents can be decoupled or neglected, one could also potentially use a device for measuring piezoresistivity (MEMS-based¹¹ or otherwise¹⁰⁴) with a Raman laser as the heat source and thermometer.

5.6. Mechanical Behavior of GeTe Nanowires

Our finding that GeTe nanowires undergo Lüders-like transformations under strain presents more questions than answers, particularly since no theoretical studies of the mechanical properties of GeTe have previously been performed to which we could compare. As GeTe is also a candidate for phase change memory applications,²⁰⁸ it is particularly interesting that mechanical stress can be used to change the structure, and it is particularly important that its effects are understood in order to incorporate these materials in real devices. First, it will be necessary to perform force- or displacement-controlled measurements, as the compliance of the MEMS-based load cell used likely resulted in the stepped nature of the transformation observed in our experiments. High resolution *in situ* TEM, selected area electron diffraction (SAED), or electron backscatter diffraction (EBSD) measurements will also be needed to understand the phase transformation, as our measurements shed no light on whether the transform is between orientations or between different structures. Either of these prospects would present an opportunity to study the thermal or electrical conductivity dependence on either crystal orientation or structure, as well.

Appendix

Raman Thermography on the NT-MDT NTEGRA System at Penn

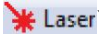
This Appendix describes the steps I take when performing Raman thermography or piezothermography on the NT-MDT system at Penn. Most of the settings given here were arrived at over years of trial and error; there is little that is arbitrary. I have attempted to provide brief reasons for everything so that if something with the system changes, future students will have an idea whether the procedure needs adjusting or not. I've written this Appendix for a user who has been fully trained on the Raman system, but doesn't have much experience with it. This document is in no way meant to replace the official tool training, as the training will naturally be more up-to-date than this document. The Miscellaneous Notes at the end of the document are important—read through everything before you start.

I assume that the green (532 nm) laser is being used, since that's what I've used and that's the wavelength we used for the absorption calculations. If use of the red (660 nm) laser becomes necessary, or if yet another laser is installed, laser-specific settings as well as absorption calculations will need to be changed. The spot size will also be slightly different, so you will want to remeasure that as well.

A.1. Startup and Laser Calibration

1. Turn on the system power strip, slave controller (even though you will not use the slave—it keeps the laser in fixed position), and upright controller. Turn on the CDA to float the air table.
2. If you're going to be doing a lot of measurements, restart the computer. It can start to run very, very slowly after a long session otherwise.
3. Run the full pre-start procedure for the Nova Upright.
4. Put the sample chamber on—this will greatly reduce thermal drift and protect your sample from the wind coming out of the vent directly over it. To do this, you will have to remove the objective head, unplug it, put the chamber on, then plug the head back in. Leave the head off for now.
5. On the very top toolbar, select Tools → Nova Power Script → Script Panel. On the next toolbar down, a button will appear for the 532 Edge script. Click it, and it will set up almost everything specific to the 532 nm laser with the edge

filter. It will ask what Raman shift you want, just click OK. When it asks if you want to open the shutter, this is for the laser, so select Cancel.

6. Turn on the power strip for the 532 nm laser *after* you've run the 532 Edge (or Notch, if you like) script and you're sure all the filters for the 532 are in place. This is so you don't accidentally burn the CCD.
7. Turn off the positioning laser (this button on the top toolbar should be unselected: ). You don't need this and it will mess up the power measurements if it's on.
8. Change "Bias Voltage" to "PMT", then set it to roughly 400-500 V, though this will largely depend on what you're looking at and your laser power. You don't want to saturate the PMT but you do want a high enough voltage that you get good contrast.
9. Select the Spectra button.
 - (a) On the Andor CCD tab, set the cooler to -60°C.
 - (b) Make sure the Laser box is set to 532 and not 660.
 - (c) Make sure you have shift speed V: 4.876, H: 0.05 (these generally shouldn't change).
 - (d) Select the Options button and make sure Flipping is unchecked. Otherwise your spectra will be reversed. Set Output Amplifier to EMCCD and Preamplifier Gain to 4. Set EMCCD gain to whatever works for you—I use 100-150. These settings will control your signal and noise intensities. Click Save All Parameters when you're done and close the window.
 - (e) Select Full Spectrum Recording since you want your maps to contain full spectra.
 - (f) Make sure Crop Mode (next to the Width box) is unchecked, otherwise you might not see anything.
10. On the Nano30 window:
 - (a) Select the Excitation tab. Set the half wave plate to 532 nm, then click the arrow pointing to the right and make sure Half Wave Plate (*not* Half Wave Plate Change) is set to 950. This will polarize your incident light in the y-direction of the maps (i.e., parallel to the short edge of the air table). I usually want the light polarized along the direction of strain—if you decide to strain along x, or if you want the light polarized perpendicular to the applied strain along y, set Half Wave Plate to 50.

- (b) Select the Spectrometer tab. Open the Shutter (allows for light to hit the CCD). Set Grating to 1800/500 (highest resolution/smallest band standard grating—for higher resolution switch to Echelle but your signal will be very weak). Set Wavelength to 547 nm. Click Set All and then wait about 5 minutes while it changes the grating (if it needs to change the grating). The wavelength will end up at like 547.0002nm, that's fine. If it doesn't, use the left and right arrows next to the wavelength to get there. This will center the Si Raman spectrum; if you're doing another material, change the wavelength.
11. Once the laser has been on for 20-30 minutes, you can start calibrating:
- (a) The power meter lives in the optics lab on the other side of the curtain, but the sensor is in a small pinkish baggie in the black tool chest. Unscrew the tube-like collar from the sensor and put a strip of double-sided carbon tape on the bottom.
 - (b) Remove the objective head if you haven't already, lower the sample stage as far as it will go, place the sensor on top of the ring which protects the piezo stage, and replace the objective head.
 - (c) Make sure the flywheel is set to 100%.
 - (d) You cannot get accurate power measurements if the laser is focused on the sensor, and moreover you run the risk of burning the anti-reflective coating—it cannot take such high power density. The NA of the objective is 0.7 (we measured 570 nm FWHM spot size, right where it should be), so the sensor should be lowered ~ 1 mm from focused to get a 1-2 mm spot size. With the laser off, raise the stage to get the sensor closer to the objective, then use the manual x- and y-translation of the stage to center the sensor as best you can. Then, height-wise, you want it so you can just see a sliver of space between the bottom of the objective and the top of the sensor. You'll really need a flashlight to see this.
 - (e) Put a USB stick into the power meter. Select the button to the left of the “?” button and make sure the wavelength is set to 532 nm. On the Trend screen, select Create File and name your file. Select File Manager and make sure you're in your USB stick. Make sure the Duration is set to something longer than your calibration (I use 1.5 hours), and if not, select Trend Setup and increase it.
 - (f) With the laser off, push the Zero button on the meter.
 - (g) The powers you choose should depend on the sample. Get a feel for what ND filters will yield what powers (*this will change day to day, so do it every time!*) before you start.
 - (h) Set up a calibration table to record what ND filter you used, what time you changed it, and roughly the settled power. Always return to the first

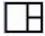
ND filter you used, to check that power is not slowly drifting. Six to ten different values should be enough to create a calibration curve. Don't vary ND value monotonically—you want to jump around.

- (i) Turn the laser shutter off, start recording, then turn the laser shutter on. Change ND filter when the power settles. This should take at least 2 minutes, sometimes more.
- (j) When done, hit stop, turn off the power meter, remove your USB stick.

A.2. MEMS-Based Nanowire Testing

For testing nanowires mounted on a MEMS-based tensile testing device on a ceramic dual inline package (cerDIP), follow this procedure. For thin films mounted on stretchers, skip to the next section.

1. Select Tools → Calibrations → Load Calibrations and choose Kate.par. I did some piezo-stage calibrations in August 2013 (Instruction manual—not Reference manual—chapter 7) and this should take care of the weird feedback in the stage. Then go to Tools → Calibrations → Change Calibrations and change the sample height to 10 mm. If it seems that your programmed scan size doesn't match reality, play around with this quantity. It affects how the piezo stage moves, so if its off you'll be measuring the wrong distances in the x-y plane.
2. Attach one magnetic chuck to the bottom of the cerDIP with a little bit of carbon tape.
3. To make leads, use ~1 foot regular copper-core electrical wires. With a wire stripper, take ~4 inches of coating off one end, isolate a single copper strand, and cut off the rest. Take that single wire and gently wrap it around the end of a sharp tweezer to make a loop. Strip ~1/2 inch off the other end. Repeat so you have at least 2 leads. The use of the thin leads is to minimize drift and the piezo-stage skipping.
4. Put the loops you made at the end of the single strands and place them on the appropriate legs of the cerDIP to make electrical connections to the actuator. Put a small piece of tape at the bottom of the legs to prevent the loops from slipping off or shorting.
5. Make sure the Keithley 2636A is connected to the laptop via the LAN. Turn it on *before* you attach any leads to the device—when it turns on, it will put out a test current which can fry your device.
6. Connect leads to the Keithley 2636A, either channel. If using the CINT tensile stage, the resistance across the actuator should be 600-800 Ω .

7. Put 2 magnetic chucks on the stage, and the cerDIP on top (so 3 total magnetic chucks), roughly aligned as you want it. I usually mount the cerDIP so that its long axis is along the y-direction, as is the wire. Now you need to minimize the strain on the thin leads so they don't cause any drift. To do this, I usually put a piece of masking tape down on the front part of the translational stage and tape the lead right where you cut the rest of the copper strands there. I put the other lead around the left side, taped near the base of the objective head.
8. On the additional operations page (this button: ) select Scheme, then click the Z button and set the z-height to near the center of the range. Later this will allow you to perform fine focusing. Then raise the stage so the wire is focused and roughly aligned along the y-direction (or x-direction, if that's what you want, but here I assume you're using y).
9. If the wire is aligned along y, you'll want to set the scan to go column-wise rather than row-wise. Between the Run and Scan Size buttons on the Scan (Master) tab, set it for Fast Y, Slow X.
10. Your life will be much easier if you get the wire as well-aligned with the y-direction of the stage as possible. Use the PMT to make maps of the wire region at relatively low powers ($\sim 100 \mu\text{W}$). I usually first make a large map (large step size), then try to only scan in the wire gauge section in order to minimize exposure of the EBID to the laser. Use the focus knob to maximize the PMT signal you get from the wire itself. Rotate the cerDIP until the wire is squarely aligned. Don't rely on the optical camera, since it's usually off by a few degrees, and when using the PMT only use the Master scanner—*do not use the slave!* Take slave scans of a flat Si wafer and fit the spectra if you want to see why.
11. Choose an appropriate collection time and power, center the laser on the wire, and use Live Mode and the Z-scanner on the Scheme tab to maximize Raman signal. Don't rely on the PMT for this, sometimes it gets pretty out of focus.
12. Make Raman maps along and across the nanowire using 5+ different laser intensities (via the ND filter), varied non-monotonically (this is so if there's systematic drift in your peak position, you'll catch it). Under "Select Signals" you want both CCD and Ext2 or PMT, so you have reflectivity as well as Raman. I usually choose my step size to balance the diameter of the nanowire (you want your step less than the diameter, so you know you're not just measuring on either side) with time to make a map. 100 nm works well for the Sigma Aldrich nanowires ($d=170\text{-}180 \text{ nm}$), but if you're down to 80 nm you might want to decrease the step size. Of course, this means you'll need more points along the nanowire, which may become prohibitively time consuming. It's a balance. You can stop the scan as soon as it's clear you've scanned the entire wire (signal has mostly disappeared)—after that you're just collecting spectra from empty space.

13. For straining, turn the flywheel to “None” and turn the light on, then focus where you want to do your strain or load measurements. Set up the image software to take a series by right-clicking on the screen, selecting settings, then snapshot. Choose your folder and your file name, set it to 100 images (this is the max, and you can always stop it if you want less), and some time increment. Make sure you’ll have enough time to capture images for the entire straining period.
14. Strain using the Keithley for CINT LabView program. Under “My Stuff” there’s a program called “CINT Actuation Click to Continue.” This will stop the actuator and hold it so you can make your measurements. The code is written as if you wanted to pull, hold, pull, hold, pull, hold, etc., but really you should do pull, hold, unload (so you can see if you have any relaxations, as well as get 2 measurements of stress from the load cell rather than just the one). So, set the increment to the same as the max.
15. Start collecting images, and when you have ~5 or so, start running the program and click OK until the voltage starts increasing. Use the Z-scanner to keep everything in focus if it’s drifting. When the actuator voltage stops increasing, let the image software collect a few more images, then stop them.
16. Repeat the Raman measurements for the strained wire, then repeat the image collection while you unload.



A.3. Thin Film Testing on a Stretcher

1. The best way to get to the unstrained state is to buckle the tensile bar, then unbuckle it under an optical microscope in backscatter configuration. When the bar is straight, it will look like it’s lighting up when it’s reflecting light straight back into the objective. When carrying the stretcher around I usually try to make sure the bar is buckled so that a slight jostle won’t break it, though, so it’s useful to get to unstrained, then buckle a set amount, then reverse that amount in the Raman room. Overall, it’s better to do your first measurements slightly buckled, then unbuckled, then strained, than it is to do your first measurements strained and not have an unstrained reference.
2. In the Nova software, select Tools → Calibrations → Load Calibrations and choose Kate-stretcher.par. I did some piezo-stage calibrations in August 2014 (Instruction manual—not Reference manual—chapter 7) and this should take care of the weird feedback in the stage. Then go to Tools → Calibrations → Change Calibrations and change the sample height to 13 mm. If it seems that your programmed scan size doesn’t match reality, play around with this quantity.

It affects how the piezo stage moves, so if its off you'll be measuring the wrong distances in the x-y plane.

3. Attach one magnetic chuck to the bottom of a glass slide with a little bit of carbon tape, and place another chuck on the stage. Put the glass+chuck on top of this chuck (this is so you can rotate the glass slide), and place the stretcher on top of that, with the bar aligned along y.
4. Get the tensile bar as well-aligned with the y-direction of the stage as possible. Use the PMT to make maps near some feature which you can align (e.g., a mesh or the edge of the tensile bar), and rotate the sample using the glass slide until your PMT maps are square. Don't rely on the optical camera, since it's usually off by a few degrees, and when using the PMT only use the Master scanner—*do not use the slave!* Take slave scans of a flat Si wafer and fit the spectra if you want to see why.
5. Choose an appropriate collection time and power, then use Live Mode and the Z-scanner on the Scheme tab to maximize Raman signal. Don't rely on the PMT for this, sometimes it gets pretty out of focus.
6. Make Raman maps using several different laser intensities (via the ND filter), varied non-monotonically (this is so if there's systematic drift in your peak position, you'll catch it). Under "Select Signals" you want both CCD and Ext2 or PMT, so you have reflectivity as well as Raman. I've found Raman maps greater than about 30um in size suffer from changes in focus at the edges, which give changes in heating and peak intensity, so try not to make any really big maps. For thin films I try to use at least 6 or 7 different powers, since you don't get the "off-axis" spectra like you do with nanowires which effectively increases the number of powers. Vary laser power using the ND filter non-monotonically (this is so if there's systematic drift in your peak position, you'll catch it). Step size will depend on whether you need spatial information. For nanomeshes, this will depend on ligament/hole size. For our FIB milled nanomeshes with $\sim 2 \mu\text{m}$ holes and $\sim 3 \mu\text{m}$ ligaments, I found 0.5-1 μm step is fine, with minimum map size enough to cover at least one unit cell of the mesh, preferably more.
7. Strain manually. If you can line up a dirty part of the tensile bar or the mesh itself nearly the same way at each strain increment, take a single snapshot using the video software and then do DIC later. Do your best to make sure the images are as close to the same location as possible.

A.4. Saving Data and Shutting Down

1. When you have all the maps you want, on the Data tab I usually rename each good map after its ND filter, then delete everything else. Save the *.mdt file after each strain increment!
2. When making nanowire measurements, if you're not using the entire square map, on the Data tab select the map, then click the Select Region button: , put a box around your good data, then click "Cropping." This will create another, rectangular-shaped map, which you should export instead of the square map with all that dead space.
3. To export, on the Data tab select the map you want, then click the export button:  and select Matlab *.m file. You should name your files with the format PREFIX###.m so you can fit them in Matlab later. I usually name the files after the ND filter (e.g., for ND=1.2 I'd name the file ND120.m). Do this for every map, and keep the prefix the same for each. You can also do the exporting later from another machine, since the Nova software is free to install.
4. When done with everything, slide the CCD cooler to -10°C—this should gradually bring the temperature up to 0°C+, but if it gets stuck at -10 just turn the cooler off.
5. Transfer your files, turn off the slave controller, laser, and upright controller. Turn off the CDA. When the CCD is up to 0°C+, turn off the system power strip.

A.5. Miscellaneous Notes

- Monitor the X- and Y-sensors at the bottom of the additional options page. When you're not scanning with the Master, RMS for both should be around 0.000X (X=1-5). If you get some generation there (it will look like the stage is oscillating back and forth) click on the Closed Loop tab (also on the additional operations page) and play with X and Y Band. Between 30 and 180 will usually work. Often you need to adjust both. For the stretcher in particular I've found setting these both to 40-50 is best. Sometimes you'll get generation when the stage is at certain positions, particularly the corners, and sometimes it will start randomly after hours of no generation, so keep an eye on it.
- If your peaks are slightly off from where they should be:
 - Always bring a piece of bulk Si wafer or graphite with you so you can figure out if problems are due to the system or your sample.

- Check the “Central Pix” quantity on the Andor CCD tab. It should be near 800. Change this and click Save and it will adjust the calibration between Raman shift and CCD pixel position. You can also change to very high laser intensity (use a bulk material as the substrate) and look at where the slight bit of incident laser wavelength comes through the filter, which should be at 0 cm^{-1} (you’ll need to be looking at the part of the spectrum where you can see both positive and negative Raman shifts).
- Make sure Flipping is off (Andor CCD tab → Options).
- On the Nano30 window → Registration tab the pinhole should typically be set for $70\text{ }\mu\text{m}$, which will maximize spatial resolution. Increasing this up to $150\text{ }\mu\text{m}$ will give poorer spatial resolution but much more signal intensity.
- For nanowire testing, if you’re clamping using EBID (actually this will probably apply no matter what you bond with), you’ll want to keep the laser away from it as much as possible, since it will both degrade the clamp (mechanically) and cause the carbon to diffuse down the wire. I mill the edges of the grips so they make steps, as in Figure A.1 below. This way, as I’m moving the laser along the nanowire, it hits the bottom step before the EBID and I know not to go any further. It is not sufficient to simply clamp the wire further back from the grip, since this will cause some complicated strains in the nanowire due to friction with the grip.

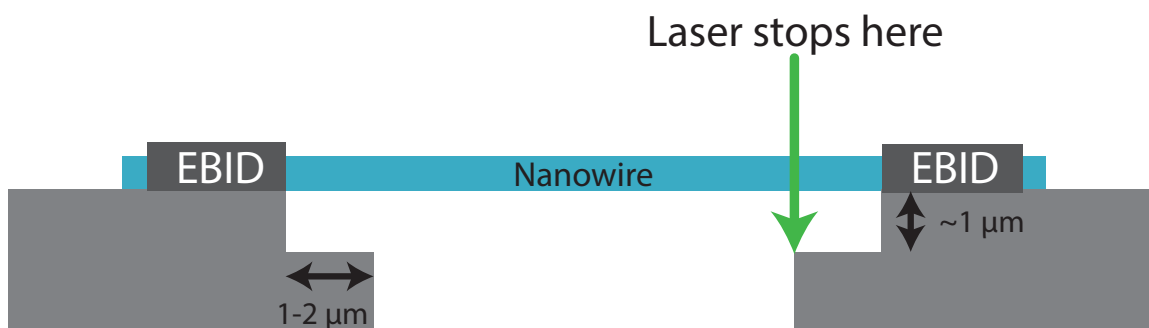


Figure A.1: Schematic of steps in the grips. These steps are milled using the FIB prior to nanowire manipulation. As the laser scans the nanowire, it can be seen hitting the step before it reaches the EBID clamp, so that clamp exposure to the laser may be minimized.

Bibliography

- [1] S S Brenner. Tensile strength of whiskers. *J. Appl. Phys.*, 27:1484–1491, 1956.
- [2] T Namazu, Y Isono, and T Tanaka. Evaluation of size effect on mechanical properties of single crystal silicon by nanoscale bending test using AFM. *J. Microelectromechanical Syst.*, 9:450–459, 2000.
- [3] Massood Tabib-Azar, Maissarath Nassirou, Run Wang, S Sharma, T I Kamins, M Saif Islam, and R Stanley Williams. Mechanical properties of self-welded silicon nanobridges. *Appl. Phys. Lett.*, 87:113102, 2005.
- [4] Samuel Hoffmann, Ivo Utke, Benedikt Moser, Johann Michler, Silke H Christiansen, Volker Schmidt, Stephan Senz, Peter Werner, Ulrich Gösele, and Christophe Ballif. Measurement of the bending strength of vapor-liquid-solid grown silicon nanowires. *Nano Lett.*, 6:622–5, 2006.
- [5] Michael J Gordon, Thierry Baron, Florian Dhalluin, Pascal Gentile, and Pierre Ferret. Size effects in mechanical deformation and fracture of cantilevered silicon nanowires. *Nano Lett.*, 9:525–529, 2009.
- [6] G Stan, S Krylyuk, A V Davydov, I Levin, and R F Cook. Ultimate bending strength of Si nanowires. *Nano Lett.*, 12:2599–2604, 2012.
- [7] Ferran Urena, Sarah H. Olsen, Lidija Siller, Umesh Bhaskar, Thomas Pardoen, and Jean-Pierre Raskin. Strain in silicon nanowire beams. *J. Appl. Phys.*, 112:114506, 2012.
- [8] Wonmo Kang and M Taher A Saif. *In situ* study of size and temperature dependent brittle-to-ductile transition in single crystal silicon. *Adv. Funct. Mater.*, 23:713–719, 2013.
- [9] Xinxin Li, Takahito Ono, Yuelin Wang, and Masayoshi Esashi. Ultrathin single-crystalline-silicon cantilever resonators: Fabrication technology and significant specimen size effect on Youngs modulus. *Appl. Phys. Lett.*, 83:3081, 2003.
- [10] Yong Zhu, Feng Xu, Qingquan Qin, Wayne Y Fung, and Wei Lu. Mechanical properties of vapor-liquid-solid synthesized silicon nanowires. *Nano Lett.*, 9:3934–3939, 2009.

- [11] Yan Liang Yong Zhang, Xinyu Liu, Changhai Ru, Lixin Dong, and Yu Sun. Piezoresistivity characterization of synthetic silicon nanowires using a MEMS device. *J. Microelectromechanical Syst.*, 20:959–967, 2011.
- [12] M S Steighner, L P Snedeker, B L Boyce, K Gall, D C Miller, and C L Muhlstein. Dependence on diameter and growth direction of apparent strain to failure of Si nanowires. *J. Appl. Phys.*, 109:033503, 2011.
- [13] Dongfeng Zhang, Jean-Marc Breguet, Reymond Clavel, Vladimir Sivakov, Silke Christiansen, and Johann Michler. *In situ* electron microscopy mechanical testing of silicon nanowires using electrostatically actuated tensile stages. *J. Microelectromechanical Syst.*, 19:663–674, 2010.
- [14] Q H Jin, T Li, Y L Wang, X L Gao, and F F Xu. Confirmation on the size-dependence of Young’s modulus of single crystal silicon from the TEM tensile tests. In *IEEE Sensors*, pages 2530–2533, 2010.
- [15] Hamed Sadeghian, Chung-Kai Yang, Johannes F L Goosen, Andre Bossche, Urs Stauer, Paddy J French, and Fred van Keulen. Effects of size and defects on the elasticity of silicon nanocantilevers. *J. Micromechanics Microengineering*, 20:064012, 2010.
- [16] David Roundy and Marvin Cohen. Ideal strength of diamond, Si, and Ge. *Phys. Rev. B*, 64:212103, 2001.
- [17] Y M Huang, J C H Spence, and Otto F Sankey. The effect of impurities on the ideal tensile strength of silicon. *Philos. Mag. A*, 70:53–62, 1994.
- [18] Scott E Thompson, Mark Armstrong, Chis Auth, Mohsen Alavi, Mark Buehler, Robert Chau, Steve Cea, Tahir Ghani, Glenn Glass, Thomas Hoffman, Chia-Hong Jan, Chis Kenyon, Jason Klaus, Kelly Kuhn, Zhiyong Ma, Brian McIntyre, Kaizad Mistry, Anand Murthy, Borna Obradovic, Ramune Nagisetty, Phi Nguyen, Sam Sivakumar, Reaz Shaheed, Lucian Shifren, Bruce Tufts, Sunit Tyagi, Mark Bohr, and Youssef El-Mansy. A 90-nm logic technology featuring strained-silicon. *IEEE Trans. Electron Devices*, 51:1790–1797, 2004.
- [19] Min Chu, Yongke Sun, Umamaheswari Aghoram, and Scott E Thompson. Strain: A solution for higher carrier mobility in nanoscale MOSFETs. *Annu. Rev. Mater. Res.*, 39:203–229, 2009.
- [20] J L Hoyt, H M Nayfeh, S Eguchi, I Aberg, G Xia, T Drake, E A Fitzgerald, and D A Antoniadis. Strained silicon MOSFET technology. In *IEDM*, pages 23–26, 2002.
- [21] Akram I Boukai, Yuri Bunimovich, Jamil Tahir-Kheli, Jen-Kan Yu, William A Goddard III, and James R Heath. Silicon nanowires as efficient thermoelectric materials. *Nature*, 451:168–171, 2008.

- [22] Allon I Hochbaum, Renkun Chen, Raul Diaz Delgado, Wenjie Liang, Erik C Garnett, Mark Najarian, Arun Majumdar, and Peidong Yang. Enhanced thermoelectric performance of rough silicon nanowires. *Nature*, 451:163–168, 2008.
- [23] Sabah K Bux, Richard G Blair, Pawan K Gogna, Hohyun Lee, Gang Chen, Mildred S Dresselhaus, Richard B Kaner, and Jean-Pierre Fleurial. Nanostructured bulk silicon as an effective thermoelectric material. *Adv. Funct. Mater.*, 19:2445–2452, 2009.
- [24] Jinyao Tang, Hung-Ta Wang, Dong Hyun Lee, Melissa Fardy, Ziyang Huo, Thomas P Russell, and Peidong Yang. Holey silicon as an efficient thermoelectric material. *Nano Lett.*, 10:4279–4283, 2010.
- [25] George E Dieter. *Mechanical Metallurgy*. McGraw-Hill, Inc., 1986.
- [26] Charles Kittel. *Introduction to Solid State Physics*. John Wiley & Sons, Inc., 1996.
- [27] Jihui Yang. Theory of thermal conductivity. In Terry M Tritt, editor, *Thermal Conductivity: Theory, Properties, and Applications*, pages 1–20. Kluwer Academic/Plenum Publishers, 2004.
- [28] P G Klemens. Thermal conductivity and lattice vibrational modes. In F Seitz and D Turnbull, editors, *Solid State Physics*, volume 7, pages 1–98. Academic Press Inc., 1958.
- [29] Neil W Ashcroft and N David Mermin. *Solid State Physics*. Saunders College Publishing, 1976.
- [30] Renkun Chen, Allon I Hochbaum, Pdraig Murphy, Joel Moore, Peidong Yang, and Arun Majumdar. Thermal conductance of thin silicon nanowires. *Phys. Rev. Lett.*, 101:105501, 2008.
- [31] Gregory S Doerk, Carlo Carraro, and Roya Maboudian. Single nanowire thermal conductivity measurements by Raman thermography. *ACS Nano*, 4:4908–4914, 2010.
- [32] Deyu Li, Yiyang Wu, Philip Kim, Li Shi, Peidong Yang, and Arun Majumdar. Thermal conductivity of individual silicon nanowires. *Appl. Phys. Lett.*, 83:2934–2936, 2003.
- [33] Joseph P Feser, Jyothi S Sadhu, Bruno P Azeredo, Keng H Hsu, Jun Ma, Junhwan Kim, Myunghoon Seong, Nicholas X Fang, Xiuling Li, Placid M Ferreira, Sanjiv Sinha, and David G Cahill. Thermal conductivity of silicon nanowire arrays with controlled roughness. *J. Appl. Phys.*, 112:114306, 2012.

- [34] Jongwoo Lim, Kedar Hippalgaonkar, Sean C Andrews, Arun Majumdar, and Peidong Yang. Quantifying surface roughness effects on phonon transport in silicon nanowires. *Nano Lett.*, 12:2475–2482, 2012.
- [35] M G Ghossoub, K V Valavala, M Seong, B Azeredo, K Hsu, J S Sadhu, P K Singh, and S Sinha. Spectral phonon scattering from sub-10 nm surface roughness wavelengths in metal-assisted chemically etched Si nanowires. *Nano Lett.*, 13:1564–1571, 2013.
- [36] Dae Ho Lee, Yongkwan Kim, Gregory S Doerk, Ian Laboriante, and Roya Maboudian. Strategies for controlling Si nanowire formation during Au-assisted electroless etching. *J. Mater. Chem.*, 21:10359–10363, 2011.
- [37] Zhipeng Huang, Nadine Geyer, Peter Werner, Johannes de Boor, and Ulrich Gösele. Metal-assisted chemical etching of silicon: a review. *Adv. Mater.*, 23:285–308, 2011.
- [38] Yuping He and Giulia Galli. Microscopic origin of the reduced thermal conductivity of silicon nanowires. *Phys. Rev. Lett.*, 108:215901, 2012.
- [39] C J Glassbrenner and Glen A Slack. Thermal conductivity of silicon and germanium from 3K to the melting point. *Phys. Rev.*, 134:A1058–A1069, 1964.
- [40] Zhifeng Sui and Irving P Herman. Effect of strain on phonons in Si, Ge, and Si/Ge heterostructures. *Phys. Rev. B*, 48:17938–17953, 1993.
- [41] Jian Zi, Kaiming Zhang, and Xide Xie. Phonon spectra of strained Si and Ge. *Phys. Rev. B*, 45:9447–9450, 1992.
- [42] Xiaobo Li, Kurt Maute, Martin Dunn, and Ronggui Yang. Strain effects on the thermal conductivity of nanostructures. *Phys. Rev. B*, 81:245318, 2010.
- [43] Wei-Wei Zhang, Shuang-Ying Lei, Hong Yu, and Qing-An Huang. Theoretical modeling of thermal expansion of crystalline silicon by using the strain phonon spectra. *2011 IEEE SENSORS Proc.*, pages 1669–1672, 2011.
- [44] Somnath Bhowmick and Vijay B Shenoy. Effect of strain on the thermal conductivity of solids. *J. Chem. Phys.*, 125:164513, 2006.
- [45] Zhenyu Yang, Rui Feng, Fei Su, Dayong Hu, and Xiaobing Ma. Isotope and strain effects on thermal conductivity of silicon thin film. *Phys. E*, 64:204–210, 2014.
- [46] P G Klemens, G K White, and R J Tainsh. Scattering of lattice waves by point defects. *Philos. Mag.*, 7:1323–1335, 1962.

- [47] Jyothi Sadhu and Sanjiv Sinha. Room-temperature phonon boundary scattering below the Casimir limit. *Phys. Rev. B*, 84:115450, 2011.
- [48] R G Ross, P Andersson, B Sundqvist, and G Backstrom. Thermal conductivity of solids and liquids under pressure. *Reports Prog. Phys.*, 47:1347–1402, 1984.
- [49] Staffan Andersson and Gunnar Backstrom. The thermal conductivity and heat capacity of single-crystal Si under hydrostatic pressure. *J. Phys. C Solid State Phys.*, 21:3727–3735, 1988.
- [50] Ming Gan and Vikas Tomar. Correlating microscale thermal conductivity of heavily-doped silicon with simultaneous measurements of stress. *J. Eng. Mater. Technol.*, 133:041013, 2011.
- [51] Wen-Pin Hsieh, Bin Chen, Jie Li, Pawel Keblinski, and David G Cahill. Pressure tuning of the thermal conductivity of the layered muscovite crystal. *Phys. Rev. B*, 80:180302, 2009.
- [52] Douglas Allen Dalton, Wen-Pin Hsieh, Gregory T Hohensee, David G Cahill, and Alexander F Goncharov. Effect of mass disorder on the lattice thermal conductivity of MgO periclase under pressure. *Sci. Rep.*, 3:2400, 2013.
- [53] H F Lee, S Kumar, and M A Haque. Role of mechanical strain on thermal conductivity of nanoscale aluminum films. *Acta Mater.*, 58:6619–6627, 2010.
- [54] M T Alam, M P Manoharan, M A Haque, C Muratore, and A Voevodin. Influence of strain on thermal conductivity of silicon nitride thin films. *J. Micromechanics Microengineering*, 22:045001, 2012.
- [55] M T Alam and M A Haque. Probing mechanical, electrical and thermal properties of nanoscale materials using MEMS devices. In *Transducers 2013*, pages 780–783, 2013.
- [56] Denis J Evans and Gary P Morriss. *Statistical Mechanics of Nonequilibrium Liquids*. Academic Press, 1990.
- [57] R C Picu, T Borca-Tasciuc, and M C Pavel. Strain and size effects on heat transport in nanostructures. *J. Appl. Phys.*, 93:3535–3539, 2003.
- [58] S-M Lee, David G Cahill, and Rama Venkatasubramanian. Thermal conductivity of SiGe superlattices. *Appl. Phys. Lett.*, 70:2957–2959, 1997.
- [59] Alexis R Abramson, Chang-Lin Tien, and Arun Majumdar. Interface and strain effects on the thermal conductivity of heterostructures: A molecular dynamics study. *J. Heat Transfer*, 124:963–970, 2002.

- [60] P G Klemens. The scattering of low-frequency lattice waves by static imperfections. *Proc. Phys. Soc. A*, 68:1113–1128, 1955.
- [61] Conyers Herring. Role of low-energy phonons in thermal conduction. *Phys. Rev.*, 95:954–965, 1954.
- [62] Peter Carruthers. Theory of thermal conductivity of solids at low temperatures. *Rev. Mod. Phys.*, 33:92–138, 1961.
- [63] Sangheon Lee and Gyeong Hwang. Theoretical determination of stable fourfold coordinated vacancy clusters in silicon. *Phys. Rev. B*, 78:125310, 2008.
- [64] Yongjin Lee, Sangheon Lee, and Gyeong Hwang. Effects of vacancy defects on thermal conductivity in crystalline silicon: A nonequilibrium molecular dynamics study. *Phys. Rev. B*, 83:125202, 2011.
- [65] T Wang, G K H Madsen, and A Hartmaier. Atomistic study of the influence of lattice defects on the thermal conductivity of silicon. *Model. Simul. Mater. Sci. Eng.*, 22:035011, 2014.
- [66] E G Song, E Kim, and Y H Lee. Fully relaxed point defects in crystalline silicon. *Phys. Rev. B*, 48:1486–1489, 1993.
- [67] M Asheghi, K Kurabayashi, R Kasnavi, and K E Goodson. Thermal conduction in doped single-crystal silicon films. *J. Appl. Phys.*, 91:5079–5087, 2002.
- [68] Paul G Klemens. Phonon scattering by oxygen vacancies in ceramics. *Phys. B Condens. Matter*, 263-264:102–104, 1999.
- [69] Patricia B Weisensee, Joseph P Feser, and David G Cahill. Effect of ion irradiation on the thermal conductivity of UO_2 and U_3O_8 epitaxial layers. *J. Nucl. Mater.*, 443:212–217, 2013.
- [70] D P White and P G Klemens. Thermal conductivity of thermoelectric $\text{Si}_{0.8}\text{-Ge}_{0.2}$ alloys. *J. Appl. Phys.*, 71:4258–4263, 1992.
- [71] Giordano Bruno. Classical theory of Rayleigh and Raman scattering. In Derek A Long, editor, *The Raman Effect: A Unified Treatment of Raman Scattering by Molecules*, volume 8, pages 31–48. John Wiley & Sons, 2002.
- [72] S Ganesan, A A Maradudin, and J Oitmaa. A lattice theory of morphic effects in crystals of the diamond structure. *Ann. Phys.*, 56:556–594, 1970.
- [73] E Anastassakis, A Pinczuk, E Burstein, F H Pollak, and M Cardona. Effect of static uniaxial stress on the Raman spectrum of silicon. *Solid State Commun.*, 8:133–138, 1970.

- [74] Meera Chandrasekhar, J B Renucci, and M Cardona. Effects of interband excitations on Raman phonons in heavily doped n-Si. *Phys. Rev. B*, 17:1623–1633, 1978.
- [75] E Anastassakis, A Cantarero, and M Cardona. Piezo-Raman measurements and anharmonic parameters in silicon and diamond. *Phys. Rev. B*, 41:7529–7535, 1990.
- [76] C-Y Peng, C-F Huang, Y-C Fu, Y-H Yang, C-Y Lai, S-T Chang, and C-W Liu. Comprehensive study of the Raman shifts of strained silicon and germanium. *J. Appl. Phys.*, 105:083537, 2009.
- [77] F Cerdeira, C J Buchenauer, Fred H Pollak, and Manuel Cardona. Stress-induced shifts of first-order Raman frequencies of diamond- and zinc-blende-type semiconductors. *Phys. Rev. B*, 5:580–593, 1972.
- [78] John J Hall. Electronic effects in the elastic constants of n-type silicon. *Phys. Rev.*, 161:756–761, 1967.
- [79] R A Cowley. Raman scattering from crystals of the diamond structure. *Le J. Phys.*, 26:659–667, 1965.
- [80] T R Hart, R L Aggarwal, and Benjamin Lax. Temperature dependence of Raman scattering in silicon. *Phys. Rev. B*, 1:638–642, 1970.
- [81] Gregory S Doerk, Carlo Carraro, and Roya Maboudian. Temperature dependence of Raman spectra for individual silicon nanowires. *Phys. Rev. B*, 80:073306, 2009.
- [82] W K Choi, T H Liew, M K Dawood, Henry I Smith, C V Thompson, and M H Hong. Synthesis of silicon nanowires and nanofin arrays using interference lithography and catalytic etching. *Nano Lett.*, 8:3799–3802, 2008.
- [83] Yeonwoong Jung, Se-Ho Lee, Dong-Kyun Ko, and Ritesh Agarwal. Synthesis and characterization of $\text{Ge}_2\text{Sb}_2\text{Te}_5$ nanowires with memory switching effect. *J. Am. Chem. Soc.*, 128:14026–14027, 2006.
- [84] Se-Ho Lee, Yeonwoong Jung, and Ritesh Agarwal. Highly scalable non-volatile and ultra-low-power phase-change nanowire memory. *Nat. Nanotechnol.*, 2:626–630, 2007.
- [85] Andrew T Jennings, Yeonwoong Jung, Johanna Engel, and Ritesh Agarwal. Diameter-controlled synthesis of phase-change germanium telluride nanowires via the vapor - liquid - solid mechanism. *J. Phys. Chem. C Lett.*, 113:6898–6901, 2009.

- [86] Gunther Richter, Karla Hillerich, Daniel S Gianola, Reiner Mönig, Oliver Kraft, and Cynthia A Volkert. Ultrahigh strength single crystalline nanowhiskers grown by physical vapor deposition. *Nano Lett.*, 9:3048–3052, 2009.
- [87] A Botman, M Hesselberth, and J J L Mulders. Improving the conductivity of platinum-containing nano-structures created by electron-beam-induced deposition. *Microelectron. Eng.*, 85:1139–1142, 2008.
- [88] J J L Mulders, L M Belova, and A Riazanova. Electron beam induced deposition at elevated temperatures: compositional changes and purity improvement. *Nanotechnology*, 22:055302, 2011.
- [89] Lisa Y Chen, Gunther Richter, John P Sullivan, and Daniel S Gianola. Lattice anharmonicity in defect-free Pd nanowhiskers. *Phys. Rev. Lett.*, 109:125503, 2012.
- [90] W F van Dorp and C W Hagen. A critical literature review of focused electron beam induced deposition. *J. Appl. Phys.*, 104:081301, 2008.
- [91] H W P Koops, A Kaya, and M Weber. Fabrication and characterization of platinum nanocrystalline material grown by electronbeam induced deposition. *J. Vac. Sci. Technol. B Microelectron. Nanom. Struct.*, 13:2400–2403, 1995.
- [92] G E Pike and C H Seager. Percolation and conductivity: A computer study. I*. *Phys. Rev. B*, 10:1421–1434, 1974.
- [93] C Schossler, A Kaya, J Kretz, M Weber, and H W P Koops. Electrical and field emission properties of nanocrystalline materials fabricated by electron-beam induced deposition. *Microelectron. Eng.*, 30:471–474, 1996.
- [94] A Botman, J J L Mulders, R Weemaes, and S Mentink. Purification of platinum and gold structures after electron-beam-induced deposition. *Nanotechnology*, 17:3779–3785, 2006.
- [95] I Utke, V Friedli, S Fahlbusch, S Hoffmann, P Hoffmann, and J Michler. Tensile strengths of metal-containing joints fabricated by focused electron beam induced deposition. *Adv. Eng. Mater.*, 8:155–157, 2006.
- [96] Feng Xu, Qingqun Qin, Ashish Mishra, Yi Gu, and Yong Zhu. Mechanical properties of ZnO nanowires under different loading modes. *Nano Res.*, 3:271–280, 2010.
- [97] Ravi Agrawal, Bei Peng, Eleftherios E Gdoutos, and Horacio D Espinosa. Elasticity size effects in ZnO nanowires—a combined experimental-computational approach. *Nano Lett.*, 8:3668–3674, 2008.

- [98] Ingrid de Wolf. Micro-Raman spectroscopy to study local mechanical stress in silicon integrated circuits. *Semicond. Sci. Technol.*, 11:139–154, 1996.
- [99] Thomas Wermelinger and Ralph Spolenak. Correlating Raman peak shifts with phase transformation and defect densities: a comprehensive TEM and Raman study on silicon. *J. Raman Spectrosc.*, 40:679–686, 2009.
- [100] K Wasmer, T Wermelinger, A Bidiville, R Spolenak, and J Michler. *In situ* compression tests on micron-sized silicon pillars by Raman microscopy–stress measurements and deformation analysis. *J. Mater. Res.*, 23:3040–3047, 2011.
- [101] J Greil, A Lugstein, C Zeiner, G Strasser, and E Bertagnolli. Tuning the electro-optical properties of germanium nanowires by tensile strain. *Nano Lett.*, 12:6230–6234, 2012.
- [102] Kathryn F Murphy, Brian Piccione, Mehdi B Zanjani, Jennifer R Lukes, and Daniel S Gianola. Strain- and defect-mediated thermal conductivity in silicon nanowires. *Nano Lett.*, 14:3785–3792, 2014.
- [103] M J Süess, R A Minamisawa, R Geiger, K K Bourdelle, H Sigg, and R Spolenak. Power-dependent Raman analysis of highly strained Si nanobridges. *Nano Lett.*, 2014.
- [104] Rongrui He and Peidong Yang. Giant piezoresistance effect in silicon nanowires. *Nat. Nanotechnol.*, 1:42–46, 2006.
- [105] Hironori Tohmyoh, Takuya Imaizumi, Hiroyuki Hayashi, and Masumi Saka. Welding of Pt nanowires by Joule heating. *Scr. Mater.*, 57:953–956, 2007.
- [106] Yang Lu, Jian Yu Huang, Chao Wang, Shouheng Sun, and Jun Lou. Cold welding of ultrathin gold nanowires. *Nat. Nanotechnol.*, 5:218–24, 2010.
- [107] Julio A Martinez, Paula P Provencio, S T Picraux, John P Sullivan, and B S Swartzentruber. Enhanced thermoelectric figure of merit in SiGe alloy nanowires by boundary and hole-phonon scattering. *J. Appl. Phys.*, 110:074317, 2011.
- [108] Yoonjin Won, Jaeho Lee, Mehdi Asheghi, Thomas W. Kenny, and Kenneth E Goodson. Phase and thickness dependent modulus of $\text{Ge}_2\text{Sb}_2\text{Te}_5$ films down to 25 nm thickness. *Appl. Phys. Lett.*, 100:161905, 2012.
- [109] Il-Mok Park, Jung-Kyu Jung, Sang-Ouk Ryu, Kyu-Jeong Choi, Byoung-Gon Yu, Young-Bae Park, Seung Min Han, and Young-Chang Joo. Thermomechanical properties and mechanical stresses of $\text{Ge}_2\text{Sb}_2\text{Te}_5$ films in phase-change random access memory. *Thin Solid Films*, 517:848–852, 2008.

- [110] J. Kalb, F. Spaepen, T. P. Leervad Pedersen, and M. Wuttig. Viscosity and elastic constants of thin films of amorphous te alloys used for optical data storage. *J. Appl. Phys.*, 94:4908, 2003.
- [111] T P Leervad Pedersen, J Kalb, W K Njoroge, D Wamwangi, M Wuttig, and F Spaepen. Mechanical stresses upon crystallization in phase change materials. *Appl. Phys. Lett.*, 79:3597, 2001.
- [112] Walter K Njoroge, Han-Willem Woltgens, and Matthias Wuttig. Density changes upon crystallization of $\text{Ge}_2\text{Sb}_{2.04}\text{Te}_{4.74}$ films. *J. Vac. Sci. Technol. A*, 20:230–233, 2002.
- [113] Qiang Guo, Minghua Li, Yi Li, Luping Shi, Tow Chong Chong, Johannes A Kalb, and Carl V Thompson. Crystallization-induced stress in thin phase change films of different thicknesses. *Appl. Phys. Lett.*, 93:221907, 2008.
- [114] Stefania Braga, Alessandro Cabrini, and Guido Torelli. Dependence of resistance drift on the amorphous cap size in phase change memory arrays. *Appl. Phys. Lett.*, 94:092112, 2009.
- [115] H-S Philip Wong, Simone Raoux, SangBum Kim, Jiale Liang, John P Reifenberg, Bipin Rajendran, Mehdi Asheghi, and Kenneth E Goodson. Phase change memory. *Proc. IEEE*, 98:2201–2227, 2010.
- [116] Sung-Hoon Hong, Jun-Ho Jeong, Kang-In Kim, and Heon Lee. High density phase change data on flexible substrates by thermal curing type nanoimprint lithography. *Microelectron. Eng.*, 88:2013–2016, 2011.
- [117] T Chattopadhyay, J X Boucherle, and H G von Schnering. Neutron diffraction study on the structural phase transition in GeTe. *J. Phys. C Solid State Phys.*, 20:1431–1440, 1987.
- [118] J Stoemenos and R Vincent. Twinning faults in epitaxial films of germanium telluride and GeTe–SnTe alloys. *Phys. Status Solidi A*, 11:545–558, 1972.
- [119] M Snykers, P Delavignette, and S Amelinckx. The domain structure of GeTe as observed by electron microscopy. *Mater. Res. Bull.*, 7:831–840, 1972.
- [120] S Perichon, V Lysenko, B Remaki, D Barbier, and B Champagnon. Measurement of porous silicon thermal conductivity by micro-Raman scattering. *J. Appl. Phys.*, 86:4700–4702, 1999.
- [121] V Lysenko, S Perichon, B Remaki, D Barbier, and B Champagnon. Thermal conductivity of thick meso-porous silicon layers by micro-Raman scattering. *J. Appl. Phys.*, 86:6841–6846, 1999.

- [122] Alexander A Balandin, Suchismita Ghosh, Wenzhong Bao, Irene Calizo, Desalegne Teweldebrhan, Feng Miao, and Chun Ning Lau. Superior thermal conductivity of single-layer graphene. *Nano Lett.*, 8:902–907, 2008.
- [123] S Ghosh, I Calizo, D Teweldebrhan, E P Pokatilov, D L Nika, A A Balandin, W Bao, F Miao, and C N Lau. Extremely high thermal conductivity of graphene: Prospects for thermal management applications in nanoelectronic circuits. *Appl. Phys. Lett.*, 92:151911, 2008.
- [124] Weiwei Cai, Arden L Moore, Yanwu Zhu, Xuesong Li, Shanshan Chen, Li Shi, and Rodney S Ruoff. Thermal transport in suspended and supported monolayer graphene grown by chemical vapor deposition. *Nano Lett.*, 10:1645–1651, 2010.
- [125] Shanshan Chen, Qiongyu Li, Qimin Zhang, Yan Qu, Hengxing Ji, Rodney S Ruoff, and Weiwei Cai. Thermal conductivity measurements of suspended graphene with and without wrinkles by micro-Raman mapping. *Nanotechnology*, 23:365701, 2012.
- [126] Shanshan Chen, Qingzhi Wu, Columbia Mishra, Junyong Kang, Hengji Zhang, Kyeongjae Cho, Weiwei Cai, Alexander A Balandin, and Rodney S Ruoff. Thermal conductivity of isotopically modified graphene. *Nat. Mater.*, 11:203–207, 2012.
- [127] Shanshan Chen, Arden L Moore, Weiwei Cai, Ji Won Suk, Jinho An, Columbia Mishra, Charles Amos, Carl W Magnuson, Junyong Kang, Li Shi, and Rodney S Ruoff. Raman measurements of thermal transport in suspended monolayer graphene of variable sizes in vacuum and gaseous environments. *ACS Nano*, 5:321–328, 2011.
- [128] Jae-Ung Lee, Duhee Yoon, Hakseong Kim, Sang Wook Lee, and Hyeonsik Cheong. Thermal conductivity of suspended pristine graphene measured by Raman spectroscopy. *Phys. Rev. B*, 83:081419, 2011.
- [129] I-Kai Hsu, Michael T Pettes, Adam Bushmaker, Mehmet Aykol, Li Shi, and Stephen B Cronin. Optical absorption and thermal transport of individual suspended carbon nanotube bundles. *Nano Lett.*, 9:590–594, 2009.
- [130] Qingwei Li, Changhong Liu, Xueshen Wang, and Shoushan Fan. Measuring the thermal conductivity of individual carbon nanotubes by the Raman shift method. *Nanotechnology*, 20:145702, 2009.
- [131] Rusen Yan, Jeffrey R Simpson, Simone Bertolazzi, Jacopo Brivio, Michael Watson, Xufei Wu, Andras Kis, Tengfei Luo, Angela R Hight Walker, and Huili Grace Xing. Thermal conductivity of monolayer molybdenum disulfide obtained from temperature-dependent Raman spectroscopy. *ACS Nano*, 8:986–993, 2014.

- [132] Martin Soini, Ilaria Zardo, Emanuele Uccelli, Stefan Funk, Gregor Koblmuller, Anna Fontcuberta i Morral, and Gerhard Abstreiter. Thermal conductivity of GaAs nanowires studied by micro-Raman spectroscopy combined with laser heating. *Appl. Phys. Lett.*, 97:263107, 2010.
- [133] E Chávez-Ángel, J S Reparaz, J Gomis-Bresco, M R Wagner, J Cuffe, B Graczykowski, A Shchepetov, H Jiang, M Prunnila, J Ahopelto, F Alzina, and C M Sotomayor Torres. Reduction of the thermal conductivity in free-standing silicon nano-membranes investigated by non-invasive Raman thermometry. *APL Mater.*, 2:012113, 2014.
- [134] S Ghosh, D L Nika, E P Pokatilov, and A A Balandin. Heat conduction in graphene: experimental study and theoretical interpretation. *New J. Phys.*, 11:095012, 2009.
- [135] M Sulfridge, T Saif, N Miller, and K O’Hara. Optical actuation of a bistable MEMS. *J. Microelectromechanical Syst.*, 11:574–583, 2002.
- [136] A Sampathkumar, T W Murray, and K L Ekinci. Photothermal operation of high frequency nanoelectromechanical systems. *Appl. Phys. Lett.*, 88:223104, 2006.
- [137] Linyou Cao, Justin S White, Joon-Shik Park, Jon A Schuller, Bruce M Clemens, and Mark L Brongersma. Engineering light absorption in semiconductor nanowire devices. *Nat. Mater.*, 8:643–647, 2009.
- [138] R A Minamisawa, M J Süess, R Spolenak, J Faist, C David, J Gobrecht, K K Bourdelle, and H Sigg. Top-down fabricated silicon nanowires under tensile elastic strain up to 4.5%. *Nat. Commun.*, 3:1096, 2012.
- [139] Tzu-Hsuan Chang and Yong Zhu. A microelectromechanical system for thermo-mechanical testing of nanostructures. *Appl. Phys. Lett.*, 103:263114, 2013.
- [140] M Kerker. *The Scattering of Light and Other Electromagnetic Radiation*. Academic Press, 1969.
- [141] Edward D Palik. *Handbook of Optical Constants of Solids*. Academic Press, 1996.
- [142] Frank P Incropera and David P DeWitt. *Introduction to Heat Transfer*. John Wiley & Sons, Inc., 1996.
- [143] Chun Cheng, Wen Fan, Jinbo Cao, Sang-Gil Ryu, Jie Ji, Costas P Grigoropoulos, and Junqiao Wu. Heat transfer across the interface between nanoscale solids and gas. *ACS Nano*, 5:10102–10107, 2011.

- [144] Hai-Dong Wang, Jin-Hui Liu, Xing Zhang, Tian-Yi Li, Ru-Fan Zhang, and Fei Wei. Heat transfer between an individual carbon nanotube and gas environment in a wide Knudsen number regime. *J. Nanomater.*, 2013:1–7, 2013.
- [145] Hai-Dong Wang, Jin-Hui Liu, Zeng-Yuan Guo, Xing Zhang, Ru-Fan Zhang, Fei Wei, and Tian-Yi Li. Thermal transport across the interface between a suspended single-walled carbon nanotube and air. *Nanoscale Microscale Thermophys. Eng.*, 17:349–365, 2013.
- [146] S G Jennings. The mean free path in air. *J. Aerosol Sci.*, 19:159–166, 1988.
- [147] Hanna Helena Klein, Jacob Karni, Rami Ben-Zvi, and Rudi Bertocchi. Heat transfer in a directly irradiated solar receiver/reactor for solid-gas reactions. *Sol. Energy*, 81:1227–1239, 2007.
- [148] Kathryn F Murphy, Lisa Y Chen, and Daniel S Gianola. Effect of organometallic clamp properties on the apparent diversity of tensile response of nanowires. *Nanotechnology*, 24:235704, 2013.
- [149] Ingrid de Wolf, H E Maes, and Stephen K Jones. Stress measurements in silicon devices through Raman spectroscopy: Bridging the gap between theory and experiment. *J. Appl. Phys.*, 79:7148–7156, 1996.
- [150] S Rubanov and P R Munroe. FIB-induced damage in silicon. *J. Microsc.*, 214:213–221, 2004.
- [151] C Villeneuve, K K Bourdelle, V Paillard, X Hebras, and M Kennard. Raman spectroscopy study of damage and strain in (001) and (011) Si induced by hydrogen or helium implantation. *J. Appl. Phys.*, 102:094905, 2007.
- [152] L Tay, D J Lockwood, J-M Baribeau, X Wu, and G I Sproule. Raman and transmission electron microscopy study of disordered silicon grown by molecular beam epitaxy. *J. Vac. Sci. Technol. A Vacuum, Surfaces, Film.*, 22:943–947, 2004.
- [153] I H Campbell and P M Fauchet. The effects of microcrystal size and shape on the one phonon Raman spectra of crystalline semiconductors. *Solid State Commun.*, 58:739–741, 1986.
- [154] H Richter, Z P Wang, and L Ley. The one phonon Raman spectrum in microcrystalline silicon. *Solid State Commun.*, 39:625–629, 1981.
- [155] M Rohde. Reduction of the thermal conductivity of SiC by radiation damage. *J. Nucl. Mater.*, 182:87–92, 1991.
- [156] R J Price. Thermal conductivity of neutron-irradiated pyrolytic beta-silicon carbide. *J. Nucl. Mater.*, 46:268–272, 1973.

- [157] A X Levander, T Tong, K M Yu, J Suh, D Fu, R Zhang, H Lu, W J Schaff, O Dubon, W Walukiewicz, D G Cahill, and J Wu. Effects of point defects on thermal and thermoelectric properties of InN. *Appl. Phys. Lett.*, 98:012108, 2011.
- [158] Y Xu and G Li. Strain effect analysis on phonon thermal conductivity of two-dimensional nanocomposites. *J. Appl. Phys.*, 106:114302, 2009.
- [159] J R Lukes and C L Tien. Molecular dynamics simulation of thermal conduction in nanoporous thin films. *Microscale Thermophys. Eng.*, 8:341–359, 2004.
- [160] Yunfei Chen, Jennifer R Lukes, Deyu Li, Juekuan Yang, and Yonghua Wu. Thermal expansion and impurity effects on lattice thermal conductivity of solid argon. *J. Chem. Phys.*, 120:3841–3846, 2004.
- [161] Xingli Zhang and Zhaowei Sun. Effects of vacancy structural defects on the thermal conductivity of silicon thin films. *J. Semicond.*, 32:053002, 2011.
- [162] M Asheghi, Y K Leung, S S Wong, and K E Goodson. Phonon-boundary scattering in thin silicon layers. *Appl. Phys. Lett.*, 71:1798–1800, 1997.
- [163] David Song and Gang Chen. Thermal conductivity of periodic microporous silicon films. *Appl. Phys. Lett.*, 84:687–689, 2004.
- [164] B Abeles. Lattice thermal conductivity of disordered semiconductor alloys at high temperatures. *Phys. Rev.*, 131:1906–1911, 1963.
- [165] P G Klemens. Phonon scattering by Cottrell atmospheres surrounding dislocations. *J. Appl. Phys.*, 39:5304–5305, 1968.
- [166] M W Ackerman and P G Klemens. Phonon scattering by impurity atmospheres surrounding dislocations. III. Combined mass and distortion scattering. *J. Appl. Phys.*, 42:968–971, 1971.
- [167] Qingping Meng, Lijun Wu, and Yimei Zhu. Phonon scattering of interfacial strain field between dissimilar lattices. *Phys. Rev. B*, 87:064102, 2013.
- [168] Jen-Kan Yu, Slobodan Mitrovic, Douglas Tham, Joseph Varghese, and James R Heath. Reduction of thermal conductivity in phononic nanomesh structures. *Nat. Nanotechnol.*, 5:718–721, 2010.
- [169] R Berman. The thermal conductivity of dielectric solids at low temperatures. *Adv. Phys.*, 2:103–140, 1953.
- [170] J Greil, S Birner, E Bertagnolli, and A Lugstein. Nanowires enabling strained photovoltaics. *Appl. Phys. Lett.*, 104:163901, 2014.

- [171] Bozhi Tian, Ping Xie, Thomas J Kempa, David C Bell, and Charles M Lieber. Single-crystalline kinked semiconductor nanowire superstructures. *Nat. Nanotechnol.*, 4:824–829, 2009.
- [172] Prashanth Madras, Eric Dailey, and Jeff Drucker. Kinetically induced kinking of vapor-liquid-solid grown epitaxial Si nanowires. *Nano Lett.*, 9:3826–3830, 2009.
- [173] Ildar R Musin and Michael A Filler. Chemical control of semiconductor nanowire kinking and superstructure. *Nano Lett.*, 12:3363–3368, 2012.
- [174] Su Li, Xiaozhong Zhang, Lihuan Zhang, and Min Gao. Twinning-induced kinking of Sb-doped ZnO nanowires. *Nanotechnology*, 21:435602, 2010.
- [175] Peite Bao, Rongkun Zheng, Sichao Du, Li Li, Wai Kong Yeoh, Xiangyuan Cui, and Simon P. Ringer. Single crystal kinked ZnO [001] and [110] nanowires: Synthesis, characterization, and growth/kinking mechanism. *Cryst. Growth Des.*, 12:3153–3157, 2012.
- [176] H Hugo Pérez Garza, Eric W Kievit, Grégory F Schneider, and Urs Staufer. Controlled, reversible, and nondestructive generation of uniaxial extreme strains (>10%) in graphene. *Nano Lett.*, 14:4107–4113, 2014.
- [177] Ning Wei, Lanqing Xu, Hui-Qiong Wang, and Jin-Cheng Zheng. Strain engineering of thermal conductivity in graphene sheets and nanoribbons: a demonstration of magic flexibility. *Nanotechnology*, 22:105705, 2011.
- [178] Gwan-Hyoung Lee, Ryan C Cooper, Sung Joo An, Sunwoo Lee, Arend van der Zande, Nicholas Petrone, Alexandra G Hammerberg, Changgu Lee, Bryan Crawford, Warren Oliver, Jeffrey W Kysar, and James Hone. High-strength chemical-vapor-deposited graphene and grain boundaries. *Science.*, 340:1073–1076, 2013.
- [179] Zhen Hua Ni, Ting Yu, Yun Hao Lu, Ying Ying Wang, Yuan Ping Feng, and Ze Xiang Shen. Uniaxial strain on graphene: Raman spectroscopy study and band-gap opening. *ACS Nano*, 2:2301–2305, 2008.
- [180] Ting Yu, Zhenhua Ni, Chaoling Du, Yumeng You, Yingying Wang, and Zexiang Shen. Raman mapping investigation of graphene on transparent flexible substrate: The strain effect. *J. Phys. Chem. C Lett.*, 112:12602–12605, 2008.
- [181] T Mohiuddin, A Lombardo, R R Nair, A Bonetti, G Savini, R Jalil, N Bonini, D M Basko, C Galiotis, N Marzari, K S Novoselov, A K Geim, and A C Ferrari. Uniaxial strain in graphene by Raman spectroscopy: G peak splitting, Grüneisen parameters, and sample orientation. *Phys. Rev. B*, 79:205433, 2009.

- [182] Mark A Bissett, Wataru Izumida, Riichiro Saito, and Hiroki Ago. Effect of domain boundaries on the Raman spectra of mechanically strained graphene. *ACS Nano*, 6:10229–10238, 2012.
- [183] Otakar Frank, Milan Bouša, Ibsam Riaz, Rashid Jalil, Kostya S Novoselov, Georgia Tsoukleri, John Parthenios, Ladislav Kavan, Konstantinos Papagelis, and Costas Galiotis. Phonon and structural changes in deformed Bernal stacked bilayer graphene. *Nano Lett.*, 12:687–93, 2012.
- [184] Zhixin Guo, Dier Zhang, and Xin-Gao Gong. Thermal conductivity of graphene nanoribbons. *Appl. Phys. Lett.*, 95:163103, 2009.
- [185] K G S H Gunawardana, Kieran Mullen, Jiuning Hu, Yong P Chen, and Xiulin Ruan. Tunable thermal transport and thermal rectification in strained graphene nanoribbons. *Phys. Rev. B*, 85:245417, 2012.
- [186] F. Ma, H. B. Zheng, Y. J. Sun, D. Yang, K. W. Xu, and Paul K. Chu. Strain effect on lattice vibration, heat capacity, and thermal conductivity of graphene. *Appl. Phys. Lett.*, 101:111904, 2012.
- [187] Jianwei Zhang, Xiaodong He, Lin Yang, Guoqiang Wu, Jianjun Sha, Chengyu Hou, Cunlu Yin, Acheng Pan, Zhongzhou Li, and Yubai Liu. Effect of tensile strain on thermal conductivity in monolayer graphene nanoribbons: a molecular dynamics study. *Sensors*, 13:9388–9395, 2013.
- [188] Luiz Felipe C Pereira and Davide Donadio. Divergence of the thermal conductivity in uniaxially strained graphene. *Phys. Rev. B*, 87:125424, 2013.
- [189] L Lindsay, Wu Li, Jesús Carrete, Natalio Mingo, D A Broido, and T L Reinecke. Phonon thermal transport in strained and unstrained graphene from first principles. *Phys. Rev. B*, 89:155426, 2014.
- [190] Changgu Lee, Xiaoding Wei, Jeffrey W Kysar, and James Hone. Measurement of the elastic properties and intrinsic strength of monolayer graphene. *Science.*, 321:385–388, 2008.
- [191] Xiaohan Wang, Li Tao, Yufeng Hao, Zhihong Liu, Harry Chou, Iskandar Kholmanov, Shanshan Chen, Cheng Tan, Nishant Jayant, Qingkai Yu, Deji Akinwande, and Rodney S Ruoff. Direct delamination of graphene for high-performance plastic electronics. *Small*, 10:694–698, 2014.
- [192] Peng Zhang, Lulu Ma, Feifei Fan, Zhi Zeng, Cheng Peng, Phillip E Loya, Zheng Liu, Yongji Gong, Jiangnan Zhang, Xingxiang Zhang, Pulickel M Ajayan, Ting Zhu, and Jun Lou. Fracture toughness of graphene. *Nat. Commun.*, 5:3782, 2014.

- [193] Nathan O Weiss, Hailong Zhou, Lei Liao, Yuan Liu, Shan Jiang, Yu Huang, and Xiangfeng Duan. Graphene: an emerging electronic material. *Adv. Mater.*, 24:5782–5825, 2012.
- [194] Jinhong Du, Songfeng Pei, Laipeng Ma, and Hui-Ming Cheng. Carbon nanotube- and graphene-based transparent conductive films for optoelectronic devices. *Adv. Mater.*, 26:1958–1991, 2014.
- [195] Liang Yin, Eun Kyung Lee, Jong Woon Lee, Dongmok Whang, Byoung Lyong Choi, and Choongho Yu. The influence of phonon scatterings on the thermal conductivity of SiGe nanowires. *Appl. Phys. Lett.*, 101:043114, 2012.
- [196] F Murphy-Armando and S Fahy. Giant piezoresistance in silicon-germanium alloys. *Phys. Rev. B*, 86:035205, 2012.
- [197] Renkun Chen, Ming-Chang Lu, Vinod Srinivasan, Zhijie Wang, Hyung Hee Cho, and Arun Majumdar. Nanowires for enhanced boiling heat transfer. *Nano Lett.*, 9:548–553, 2009.
- [198] D Li, G S Wu, W Wang, Y D Wang, Dong Liu, D C Zhang, Y F Chen, G P Peterson, and Ronggui Yang. Enhancing flow boiling heat transfer in microchannels for thermal management with monolithically-integrated silicon nanowires. *Nano Lett.*, 12:3385–3390, 2012.
- [199] Yuchao Wang, Chuanshan Dai, and Shixue Wang. Theoretical analysis of a thermoelectric generator using exhaust gas of vehicles as heat source. *Appl. Energy*, 112:1171–1180, 2013.
- [200] M T Alam, A P Raghu, M A Haque, C Muratore, and A A Voevodin. Structural size and temperature dependence of solid to air heat transfer. *Int. J. Therm. Sci.*, 73:1–7, 2013.
- [201] Toshiyuki Toriyama, Daisuke Funai, and Susumu Sugiyama. Piezoresistance measurement on single crystal silicon nanowires. *J. Appl. Phys.*, 93:561, 2003.
- [202] J S Milne, A C S Rowe, S Arscott, and Ch Renner. Giant piezoresistance effects in silicon nanowires and microwires. *Phys. Rev. Lett.*, 105:226802, 2010.
- [203] N F Hinsche, I Mertig, and P Zahn. Effect of strain on the thermoelectric properties of silicon: an *ab initio* study. *J. Phys. Condens. Matter*, 12:295502, 2011.
- [204] Abhijeet Paul, Kai Miao, Ganesh Hegde, Saumitra Mehrotra, Mathieu Luisier, and Gerhard Klimeck. Enhancement of thermoelectric efficiency by uniaxial tensile stress in n-type GaAs nanowires. *IEEE Int. Conf. Nanotechnol.*, pages 1352–1357, 2011.

- [205] Y. Xu and G. Li. Strain effect analysis on the thermoelectric figure of merit in n-type Si/Ge nanocomposites. *J. Appl. Phys.*, 111:054318, 2012.
- [206] Victor Pardo, Antia S Botana, and Daniel Baldomir. Strain effects to optimize thermoelectric properties of hole-doped $\text{La}_2\text{NiO}_{4+\delta}$ via *ab initio* calculations. *Phys. Rev. B*, 87:125148, 2013.
- [207] Joo-Hyoung Lee. Significant enhancement in the thermoelectric performance of strained nanoporous Si. *Phys. Chem. Chem. Phys.*, 16:2425–2429, 2014.
- [208] M Chen, K A Rubin, and R W Barton. Compound materials for reversible, phase-change optical data storage. *Appl. Phys. Lett.*, 49:502–504, 1986.